Active gas features in three HSC-SSP CAMIRA clusters revealed by high angular resolution analysis of MUSTANG-2 SZE and XXL X-ray observations

Nobuhiro Okabe [1,2,3,4]★ Simon Dicker,[5] Dominique Eckert,[6] Tony Mroczkowski [7]
Fabio Gastaldello [8] Yen-Ting Lin,[9] Mark Devlin,[5] Charles E. Romero,[5] Mark Birkinshaw,[10]
Craig Sarazin,[11] Cathy Horellou,[12] Tetsu Kitayama,[13] Keiichi Umetsu [9] Mauro Sereno [14,15]
Brian S. Mason,[16] John A. ZuHone,[17] Ayaka Honda,[1] Hiroki Akamatsu,[18] I-Non Chiu [9]
Kotaro Kohno [19,20] Kai-Yang Lin,[9] Elinor Medezinski [21] Satoshi Miyazaki,[22] Ikuyuki Mitsuishi,[23]
Atsushi J. Nishizawa [24] Masamune Oguri,[19,25,26] Naomi Ota [27] Florian Pacaud,[28] Marguerite Pierre,[29]
Jonathan Sievers [30] Vernesa Smolčić,[31] Sara Stanchfield,[5] Keigo Tanaka,[32] Ryoichi Yamamoto,[1]
Chong Yang[1] and Atsushi Yoshida[23]

Affiliations are listed at the end of the paper

ABSTRACT
We present results from simultaneous modelling of high angular resolution GBT/MUSTANG-2 90 GHz Sunyaev–Zel'dovich effect (SZE) measurements and XMM-XXL X-ray images of three rich galaxy clusters selected from the HSC-SSP Survey. The combination of high angular resolution SZE and X-ray imaging enables a spatially resolved multicomponent analysis, which is crucial to understand complex distributions of cluster gas properties. The targeted clusters have similar optical richnesses and redshifts, but exhibit different dynamical states in their member galaxy distributions: a single-peaked cluster, a double-peaked cluster, and a cluster belonging to a supercluster. A large-scale residual pattern in both regular Compton-parameter y and X-ray surface brightness distributions is found in the single-peaked cluster, indicating a sloshing mode. The double-peaked cluster shows an X-ray remnant cool core between two SZE peaks associated with galaxy concentrations. The temperatures of the two peaks reach ∼20–30 keV in contrast to the cool core component of ∼2 keV, indicating a violent merger. The main SZE signal for the supercluster is elongated along a direction perpendicular to the major axis of the X-ray core, suggesting a minor merger before core passage. The S_X and y distributions are thus perturbed at some level, regardless of the optical properties. We find that the integrated Compton y parameter and the temperature for the major merger are boosted from those expected by the weak-lensing mass and those for the other two clusters show no significant deviations, which is consistent with predictions of numerical simulations.

Key words: gravitational lensing: weak – galaxies: clusters: general – galaxies: clusters: intracluster medium – radio continuum: galaxies – X-rays: galaxies: clusters.

1 INTRODUCTION

Galaxy clusters, whose compositions are dominated by dark matter, ionized gas and galaxies, are the largest gravitationally bound objects in the Universe and sometimes aggregate in superclusters. The abundance of galaxy clusters is sensitive to the growth of matter density perturbations, and thus serves as a cosmological probe. Thanks to recent technical progress, galaxy clusters can be discovered by various observational methods: optical (e.g. Oguri 2014; Rykoff et al. 2014; Rozo et al. 2016; Oguri et al. 2018), X-ray (e.g. Böhringer et al. 2004; Piffaretti et al. 2011; Adami et al. 2018), thermal Sunyaev–Zel'dovich effect (SZE; e.g. Planck Collaboration XXIX 2014; Bleem et al. 2015; Sifón et al. 2016), and weak-lensing

mass reconstruction (e.g. Miyazaki et al. 2007, 2018b). Optical techniques are unbiased against cluster mergers that non-linearly change properties of the intracluster medium (ICM), but suffer from projection effects along the line of sight (Okabe et al. 2019). As X-ray emission from the ICM is proportional to the square of the electron number density, projection effects are less important but this technique suffers from a cool core bias (Eckert, Molendi & Paltani 2011; Rossetti et al. 2017). The surface brightness of the thermal SZE is proportional to the line of sight integral of the ICM electron pressure, and is independent of redshift (see e.g. Birkinshaw 1999; Mroczkowski et al. 2019). When using weak-lensing shear to select clusters (Miyazaki et al. 2018b; Chen et al. 2020), the resulting sample does not rely on any baryonic physics, but may potentially suffer from projection bias in the lensing signals. While complementary, the redshift dependence and the tracer used (ICM, galaxies, or total mass) in different techniques can introduce different

★ E-mail: okabe@hiroshima-u.ac.jp

Table 1. Properties of the clusters.

CAMIRA Name	Optical morphology	RA (deg)	Dec. (deg)	z	N^a	XXL name	$k_B T_{300\mathrm{kpc}}^{b}$ (keV)	Dynamical state^c
HSC J022146-034619	Single-peake^d	35.441	-3.772	0.433	69	XLSSC 006	4.2 ± 0.5	Sloshing
HSC J023336-053022	Double-peaked^d	38.398	-5.506	0.436	47	XLSSC 105	6.0 ± 1.0	Post-major merger
HSC J021056-061154	Supercluster^e	32.735	-6.198	0.429	41	XLSSC 083	5.1 ± 0.9	Pre-minor merger

^{a}Cluster richness from the CAMIRA catalogue (Oguri et al. 2018). ^{b}X-ray temperature within 300 kpc (Adami et al. 2018). ^{c}gas properties revealed by this paper. ^{d}Okabe et al. (2019). ^{e}Pompei et al. (2016).

biases for each method. It is therefore important for the upcoming era of cluster cosmological studies to understand the selection function that arises in the construction of cluster catalogues from the true cluster population. In particular, it is essential to understand the baryonic physics as a function of dynamical state and the interplay between dark matter and baryons.

The Hyper Suprime-Cam Subaru Strategic Program (HSC-SSP; Aihara et al. 2018b, a; Bosch et al. 2018; Coupon et al. 2018; Furusawa et al. 2018; Huang et al. 2018; Kawanomoto et al. 2018; Komiyama et al. 2018; Miyazaki et al. 2018a; Aihara et al. 2019) is an on-going wide-field optical imaging survey composed of three layers of different depths (Wide, Deep and UltraDeep). The wide layer is designed to obtain five-band (*grizy*) imaging over 1400 deg^2. The HSC-SSP Survey achieves both excellent imaging quality (~ 0.7 arcsec seeing in *i*-band) and deep observations ($r \lesssim 26$ AB mag). Therefore, the HSC survey currently has the best performance to search simultaneously for galaxy clusters and to measure their weak-lensing masses (for review; Pratt et al. 2019). Oguri et al. (2018) constructed a cluster catalogue using the *Cluster finding Algorithm based on Multi-band Identification of Red-sequence gAlaxies* (CAMIRA; Oguri 2014), which is a red-sequence cluster finder that exploits stellar population synthesis model fitting. The catalogue contains ~ 1900 clusters at $0.1 < z < 1.1$ with richness larger than $N = 15$ in the ~ 240 deg^2 HSC-SSP S16A field. The accuracy of photometric redshifts of the clusters is $\sigma_z/(1 + z) \sim 0.01$ for the whole redshift range. Compared to shallower data from the Sloan Digital Sky Survey (SDSS; Rykoff et al. 2014; Oguri 2014) and the Dark Energy Survey (DES; Rykoff et al. 2016), many clusters beyond $z \sim 0.8$ were discovered for the first time (Oguri et al. 2018). Okabe et al. (2019) found ~ 190 major-merger candidates using a peak-finding method of galaxy maps of the CAMIRA clusters and confirmed that the mass ratio of the sub and main halo is higher than 0.1 based on stacked weak-lensing analysis. Our statistical approach uncovers merger boosts in stacked *ROSAT* L_X and *Planck* SZE scaling relations for the CAMIRA clusters and equatorial-shock-heated gas in cluster outskirts (Ricker & Sarazin 2001; ZuHone 2011; Ha, Ryu & Kang 2018) in both stacked X-ray and SZE images. However, using a stacked analysis makes it difficult to discriminate between the dynamical states of individual clusters, such as pre- and post-mergers. In principal, the optically selected CAMIRA clusters cover various dynamical states and stages (relaxed, minor merger, major merger, pre-merger, and post-merger), and thus systematic multiwavelength follow-up studies of individual clusters are critically important to understand the relationship between gas properties and dynamical states in more details.

In this paper, we carry out joint SZE and X-ray studies of three CAMIRA clusters exhibiting different dynamical states to derive gas distributions, and compare the gas properties with optical properties and weak-lensing masses. The SZE data were taken using MUSTANG-2 (Dicker et al. 2014; Romero et al. 2020) installed on the 100-m Green Bank Telescope (GBT). MUSTANG-2 has an

angular resolution of 9 arcsec full width at half-maximum (FWHM) at 90 GHz and an instantaneous field of view of 4.25 arcmin, well matched to our resolution requirement and the angular size of our clusters. We use X-ray images from the XXL Survey (Giles et al. 2016; Lieu et al. 2016; Pacaud et al. 2016; Pierre et al. 2016; Pompei et al. 2016; Adami et al. 2018; Guglielmo et al. 2018) that is the largest observing programme undertaken by *XMM–Newton*. The XXL Survey covers two distinct sky areas for a total of 50 deg^2 down to a sensitivity of 6×10^{-15} erg cm^{-2} s^{-1} for point-like sources ([0.5–2] keV band). The XXL survey provides us with the unique, complementary X-ray data set for the joint analysis. We use the HSC-SSP Survey data for optical and weak-lensing analyses.

This paper is organized as follows. Section 2 describes our target properties. Section 3 presents our observations, a method of joint SZE and X-ray analysis, and our weak-lensing analysis. Section 4 is devoted to the results and discussion, respectively. We summarize our results in Section 5. Throughout this paper, we use $\Omega_{\mathrm{m,0}} = 0.3$, $\Omega_{\Lambda, 0} = 0.7$, and $H_0 = 70 h_{70}$ km s^{-1} Mpc^{-1}.

2 TARGETS

We selected three clusters (Table 1) at redshifts of $z \sim 0.4$ from the sample of the HSC-SSP CAMIRA clusters (Oguri et al. 2018) to observe with MUSTANG-2. As described in Section 3.1, recovery of faint signals on angular scales larger than an instrument's instantaneous field of view (FOV) can be problematic. Clusters with angular sizes comparable to MUSTANG-2's ≈ 4.25 arcmin FOV are at medium ($z \sim 0.4$) to high ($z > 1.0$) redshifts, making them well suited for MUSTANG-2 follow-up. However, X-ray observations suffer from strong cosmological dimming and so for joint MUSTANG-2/X-ray analysis, the choice of $z \approx 0.4$ is close to optimal. At these redshifts, the 9 arcsec FWHM resolution of MUSTANG-2 enables us to resolve the pressure distribution with physical resolution of ~ 60 kpc. The point spread function (PSF) of *XMM–Newton* is comparable to the angular resolution of MUSTANG-2, and a joint analysis of MUSTANG-2 SZE and XXL X-ray observation enables measurements of the two-dimensional (2D) distributions of electron number density, temperature, pressure, and entropy parameter, all with reasonably high angular resolution.

As pointed out by Okabe et al. (2019), optically selected clusters are free from bias against the ICM merger boost because the number of luminous red galaxies is essentially conserved during cluster mergers, but X-ray and SZE observables are affected by cluster merger phenomena. This is simply caused by the collisionless nature of member galaxies and collisional particles of the ICM. Thus, the sample of optical clusters, composed of a wide range of various dynamical states, is a very well-suited sample to investigate dynamical dependence of gas properties.

As our first observation, we selected three representative clusters of different galaxy distributions (Table 1) from the CAMIRA catalogue (Oguri et al. 2018) based on galaxy distributions (Ok-
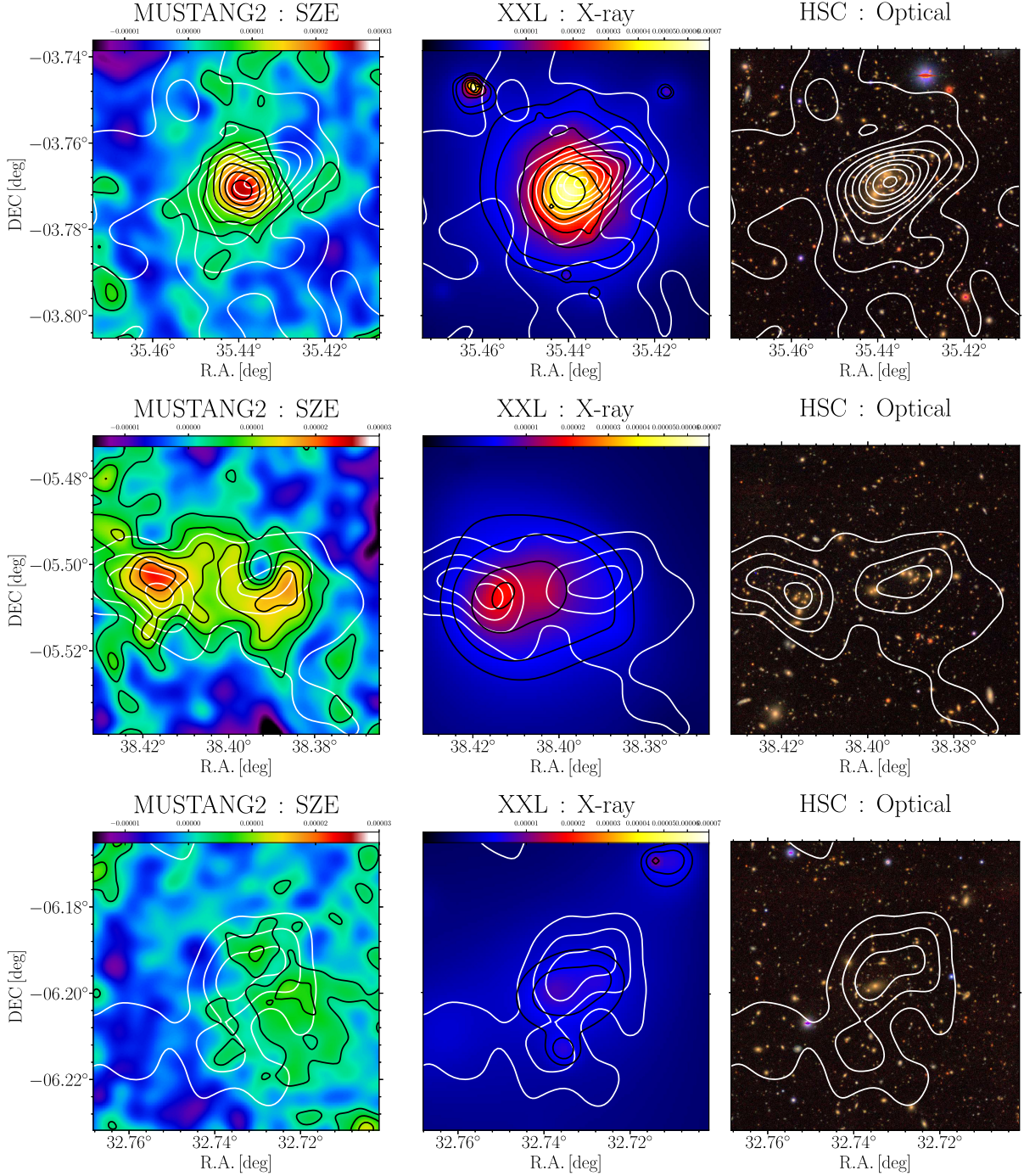
Figure 1. SZE (left), X-ray (middle), and optical (right) imaging (4 arcmin × 4 arcmin) for the three targeted clusters (from the top to the bottom; HSC J022146-034619, HSC J023336-053022, and HSC J021056-061154). *Left*: GBT/MUSTANG-2 Compton y-map with Gaussian smoothing ($\sigma = 8$ arcsec) of raw images, yielding an effective resolution of 12.5 arcsec. The black contours are at $y = [3, 7, 11, 15, 19, 23] \times 10^{-6}$. The RMS noises within 1 arcmin from the centre of FOV of the smoothed map are $y = 2, 6$, and 3×10^{-6} from the top to the bottom, respectively. The green and red colours show positive y-values and the blue and purple colours show negative values. Colour scales are the same for all the clusters. White contours are galaxy distributions, taken from the right-hand panel. *Middle*: Adaptively smoothed X-ray images in the soft band (0.5–2.0 keV) from the XXL survey. Black contours denote X-ray surface brightness ([4, 5.4, 9.8, 17, 27, 40] × 10^{-6} ct s^{-1}). The white contours are the same as those in the right-hand panel. Colour scales are the same for all the clusters. *Right*: HSC-SSP optical *riz*-colour image overlaid with galaxy contours (white) smoothed with a $\sigma = 200$ kpc Gaussian (Okabe et al. 2019). Each contour is stepped by two additional luminous member galaxies, starting at a level of two luminous galaxies.

abe et al. 2019). We first constructed Gaussian smoothed maps (FWHM = $200h_{70}^{-1}$ kpc) of number densities of red galaxies selected in the colour–magnitude plane. We then identified peaks above a redshift-dependent threshold considering the contamination of

extended galaxy distributions from nearby peaks caused by the smoothing procedure. The threshold was empirically determined to be an average peak stacked over the CAMIRA clusters at each redshift slice. The multi-peaked clusters are likely to be major-

Table 2. Properties of the data in our multiwavelength analysis.

CAMIRA name	SZE GBT MUSTANG-2[a]	X-ray XMM-Newton	Optical Subaru	WL Subaru	Synchrotron GMRT	VLA/GMRT
HSC J022146-034619	$6.1/36\sigma/8.8\sigma$	0604280101(XXL)[b]/100σ	HSC-SSP[c]	HSC-SSP[d]	–	–
HSC J023336-053022	$9.1/36\sigma/4.5\sigma$	XXL[e]/24σ	HSC-SSP	HSC-SSP	XXL[f]	FIRST[g]/TGSS[h]
HSC J021056-061154	$4.4/5\sigma/4.1\sigma$	XXL[e]/16σ	HSC-SSP	HSC-SSP[i]	–	–

[a]Observing hours on source by MUSTANG-2 (Dicker et al. 2014), the signal-to-noise ratio of the $\tilde{y}_d$ profiles (equation 8 and Figs 3, 9, and 14), and the peak signal-to-noise ratio of the 2D $\tilde{y}_d$ maps. [b]Obs Id for the pointing observation by the XXL Survey, and the signal-to-noise ratio of the $\tilde{S}_{X,d}$ profiles (equation 9 and Figs 3, 9, and 14). [c]Aihara et al. (2018b). Tanaka et al. (2018). [d]Mandelbaum et al. (2018a, b). [e]Pierre et al. (2016). [f]The GMRT data of the XXL Survey (610 MHz; Smolčić et al. 2018). [g]FIRST archival data (1.4GHz; Helfand, White & Becker 2015). [h]TGSS archival data (147.5 MHz; Intema et al. 2017). [i]Shape catalogue in the central region is not available.

merger candidates by stacked weak-lensing analysis. The method cannot resolve substructures within the smoothing scale, less massive subhaloes. We cannot discriminate between pre- and post-mergers due to the collisionless feature of galaxies.

The first cluster, HSC J022146-034619, is classified as single-peaked in galaxy distribution within the projected radius of 2 Mpc. As shown in the top right-hand panel of Fig. 1, the galaxy distribution is concentrated around the cluster centre. The second cluster, HSC J023336-053022, exhibits two galaxy peaks separated by about 520 kpc (the middle right-hand panel of Fig. 1). The third cluster, HSC J021056-061154, shows an irregular galaxy distribution (the bottom-right panel of Fig. 1). At a 200 kpc smoothing scale, the galaxy distribution has a single peak. This cluster is a part of the supercluster at $z = 0.43$ discovered by Pompei et al. (2016). As a mass proxy, we adopt cluster richness, $N \gtrsim 40$, as a selection function, which corresponds to $M_{500} \gtrsim 2 \times 10^{14} h_{70}^{-1} M_\odot$ (Okabe et al. 2019). The data used in our multiwavelength analysis are summarized in Table 2.

3 OBSERVATION AND DATA ANALYSIS

3.1 GBT/MUSTANG-2 SZE analysis

MUSTANG-2 (Dicker et al. 2014) is a 223-feedhorn bolometer camera installed on the 100-m GBT.[1] It has an angular resolution of 9 arcmin FWHM and a 75–105 GHz bandpass. The instantaneous field of view is 4.25 arcmin. We observed each cluster with a 3 arcmin radius daisy scan pattern similar to that used for other clusters by MUSTANG-2 (Romero et al. 2020), spending 6.5, 10, and 4.6 h on-source for HSC J022146-034619, HSC J023336-053022, and HSC J021056-061154, respectively. Every 20 min pointing and focus checks were carried out on 0217+0144 allowing us to calibrate out drifts in detector gains or the atmosphere. Several times a night this source was tied to observations of Uranus for absolute calibration. Stacked observations of the calibrators allowed recovery of the *effective* beam shape of the GBT. This beam includes any filtering in the mapmaker, near sidelobes from focus drifts, and any remaining pointing errors.

Data were reduced using the MIDAS data pipeline. Briefly, this pipeline first calibrates each detector with gains and beam volumes extrapolated between each observation of the point source 0217+0144. The astronomical signal is mostly between ∼0.1 Hz (i.e. ∼10 s, the time to scan across the map) and ∼10 Hz (i.e. ∼0.1 s, the time taken to scan across a point source). At lower frequencies, the
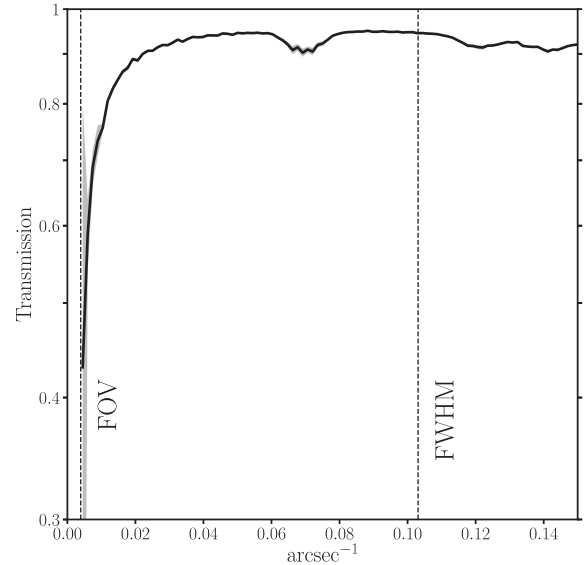
Figure 2. Effective average transfer function for our sample of clusters, $\hat{f}_{\rm TF}$, as a function of angular wavenumber k (arcsec^{-1}). The grey transparent region at low k shows that at low k a few points have large error bars. The transfer functions of individual clusters are calculated as the square root of the ratio of the 1D power spectra of the observed fake sky and input fake sky. Vertical dashed lines denote the relevant angular wavenumbers for the FOV and FWHM.

signal is dominated by 1/f noise from the atmosphere and at higher frequencies there is noise from electrical pickup. A Fourier filter (0.08–30 Hz bandpass) is applied to each detector time stream to greatly improve the data quality. After this, problematic detectors (e.g. ones with low gain or high noise) are flagged along with portions of data showing glitches. At this stage, the time streams are dominated by atmospheric emission. This can be removed using a principal component analysis to produce cleaned time streams that are made into the maps presented in this paper. More details of the MIDAS pipeline can be found in Romero et al. (2020).

Although the MIDAS pipeline reduces the rms in the raw time streams by several orders of magnitude, the maps it produces are not unbiased. Structures on angular scales significantly larger than the size of the FOV are diminished in brightness. This can be characterized by an angular transfer function ($f_{\rm TF}$; Fig. 2). When quantitatively comparing observational data to model fits, it is essential to correct for this transfer function (Section 3.3). The transfer function is calculated by passing randomized sky structure with equal power on all spatial scales through simulated observing software that produces time ordered data for a set of scans identical to those for each cluster. Those time-streams are then processed

[1]The Green Bank Observatory is a major facility supported by the National Science Foundation and operated under cooperative agreement by Associated Universities, Inc.

with the same filtering as is done on the real data and maps of the given instance of randomized sky are output. The transfer function is defined as the ratio in Fourier space of the power spectrum of the reconstructed image to the power spectrum of the input map (Fig. 2).

The rest of the analysis of the MUSTANG-2 data presented in this paper is carried out in map space. We follow Romero et al. (2015, 2017, 2020) for point source removal. To calculate cluster profiles, we use radial averaging in segments (either 90 or 45 deg) to bring down the noise/get higher accuracy in the profiles without compromising the ability to resolve the shape of the cluster.

As well as the transfer function, knowledge of the effective beam shape in the maps is critical. As described above, we made stacked beam maps for each cluster using 0217+0144. These beams were well described by the double Gaussian fit. A primary and secondary beam of an average of the three clusters have FWHM of 9.7 and 54 arcsec, respectively. The peak ratio of the secondary beam is $\sim 5 \times 10^{-3}$ of the primary one. The secondary beam agrees with the expected near-sidelobes on the GBT, given the MUSTANG-2 illumination pattern and medium-scale aperture phase errors not fully corrected by the out-of-focus (OOF) procedure.

3.2 XXL X-ray analysis

We here briefly describe X-ray analysis of the XXL Survey (Pierre et al. 2016). We processed the XXL data using the XMMSAS package and calibration files v10.0.2 and the data reduction pipeline (Pacaud et al. 2016) in order to obtain cleaned event files for each observation. We extracted photon images in the [0.5–2.0] keV band for each EPIC instrument and created co-added EPIC images by summing the images obtained for each detector. In this paper, we use the co-added images in model fittings described in Section 3.3.

We compare our results with X-ray complementary quantities from the literature, and briefly describe measurement methods. The measurement of the electron number density profile is described in detail by Eckert et al. (2017). The electron number density is measured by a deprojection method using surface brightness profiles that were extracted for each cluster using PROFFIT (Eckert et al. 2011). The X-ray temperature is measured and described in detail by Giles et al. (2016). The X-ray spectra are extracted within a circular aperture of 300 kpc centred on the X-ray positions. The background is measured from an annulus centred on the cluster with the inner radius set to the detection radius and the outer radius as 400 arcsec. The resulting temperatures are summarized in Table 1. Since there is deep X-ray pointing data (Obs Id:0604280101) for HSC J022146-034619 (XLSSC006), we also measure X-ray temperature profile following the *XMM–Newton* cluster outskirts project (XCOP; Eckert et al. 2017, 2019; Ghirardini et al. 2018; Ettori et al. 2019).

3.3 Gas modelling

We employ a Bayesian forward modelling method to measure gas properties of the ICM. In the modelling, we introduce a generalized Navarro, Frenk, and White profile (hereafter, gNFW; Navarro, Frenk & White 1997; Nagai, Kravtsov & Vikhlinin 2007b; Mroczkowski et al. 2009; Arnaud et al. 2010; Planck Collaboration XII 2011; Okabe et al. 2014a) of the electron number density and the temperature of the ICM,

$$n_e(r) = n_0 \left(\frac{r}{r_s}\right)^{-\gamma_n} \left(1 + \left(\frac{r}{r_{s,n}}\right)^{\alpha_n}\right)^{-\beta_n}, \tag{1}$$

$$T_e(r) = T_0 \left(\frac{r}{r_s}\right)^{-\gamma_T} \left(1 + \left(\frac{r}{r_{s,T}}\right)^{\alpha_T}\right)^{-\beta_T}. \tag{2}$$

Here, r is three-dimensional (3D) radius from cluster centre. We note that the notations of slope parameters are different from definitions of Nagai, Vikhlinin & Kravtsov (2007a) in order to clarify parameter degeneracy during the analysis. We assume a spherically symmetric model with $\alpha_n = \alpha_T = 2$. When the inner slope γ is additionally assumed to be $\gamma = 0$, the model corresponds to a β model (Cavaliere & Fusco-Femiano 1976) which is well used in X-ray analysis. The temperature scale radius, $r_{s,T}$, cannot be constrained well by a sharp y-distribution at $\theta > 1$ arcmin because of the transfer function. We therefore adopt $r_{s,n} = r_{s,T} = r_s$. The electron pressure is directly calculated by $P_e = n_e k_B T_e$.

The SZE Compton y-parameter and X-ray surface brightness are expressed as a geometrical projection of the spherical profiles along the line of sight,

$$y(R) = \frac{\sigma_T}{m_e c^2} \int P_e(R, l) dl, \tag{3}$$

$$S_X(R) = S_0 \int n_e(R, l)^2 dl + S_b, \tag{4}$$

where $r^2 = R^2 + l^2$, R is the projected radius from the cluster centre and l is the distance along the line of sight. Here, σ_T is the Thomson cross-section for electron scattering, m_e is the electron mass, and c is the light velocity. Since the X-ray soft-band emissivity (0.5–2.0 keV) is almost independent of gas temperature (Ettori et al. 2013), we ignore the temperature dependence. S_b and S_0 are the background components for X-ray data and the conversion factor from the electron number density to the X-ray surface brightness, respectively.

Given the model, we compute actual SZE and X-ray measurements on the sky taking into account the instrument spatial responses, namely, the PSF and the radial transfer function of the MUSTANG-2 (Section 3.1). We pixelize the models on to a regular grid of angular position θ ($\theta = R/D_A$) and then convolve them with the instrument response function using the 2D Fourier transform ($\mathcal{F}T$),

$$\tilde{y}_m(\theta) = \left(f_{\rm PSF}^{\rm SZ} f_{\rm TF}\right) \otimes y(\theta), \tag{5}$$

$$\tilde{S}_{X,m}(\theta) = f_{\rm PSF}^{\rm X} \otimes S_X(\theta), \tag{6}$$

where $f_{\rm TF}$ ($\hat{f}_{\rm TF} = \mathcal{F}T(f_{\rm TF})$) and $f_{\rm PSF}^{\rm SZ}$ are the transfer function and the PSF of the GBT/MUSTANG-2, respectively, and $f_{\rm PSF}^{\rm X}$ is the PSF of the *XMM–Newton*. We use the transfer functions and PSFs of individual clusters.

Since the X-ray surface brightness depends on only the electron number density and the y parameter is specified by both the electron number density and temperature, the constraints imposed by the SZE and X-ray data enables us to resolve a degeneracy between the number density and temperature in the y parameter and then model the 3D profiles under the assumption of spherically symmetric distributions. We therefore simultaneously fit the SZE and X-ray data with the models (equations 5–6), in a similar manner to X-COP (Eckert et al. 2017; Ghirardini et al. 2018, 2019; Ettori et al. 2019; Eckert et al. 2019) and other studies (e.g. Ruppin et al. 2020). The joint log-likelihood is written as

$$-2\ln\mathcal{L} = \sum_i \frac{(\tilde{y}_{d,i} - \tilde{y}_{m,i})^2}{\sigma_{y,i}^2} + \sum_j \frac{(\tilde{S}_{Xd,j} - \tilde{S}_{Xm,j})^2}{\sigma_{X,j}^2} + {\rm const}, \tag{7}$$

where $\tilde{y}_d$ and σ_y are the MUSTANG-2 measurements of y parameter and statistical errors and $\tilde{S}_{Xd}$ and σ_X are the X-ray surface brightness distribution and statistical errors, respectively. We do not include the X-ray temperature measurement in the joint likelihood, because the spatial resolution of the spectroscopic measurement is much worse than those of y and S_X distributions. Since n_0, T_0, and r_s are positive

parameters, we treat them as logarithmic quantities in our fitting procedures. All quantities are estimated using a central biweight in order to down-weight outliers in skewed posterior distributions.

In the Bayesian modelling, we use radial profiles computed with logarithmic binning and linearly pixelized maps as the data array of y and S_X of equation (7). The former and latter methods are called one-dimensional (1D) and 2D analyses, respectively. The former method is effective at reducing computational time and good at constraining the inner slopes of the electron number density and temperature profiles. We convert from the PSF-convolved maps to radial profiles in computing the likelihood. We choose XXL centres as central positions except for the major-merger case. The latter method is time-consuming but can consider multiple components of the ICM and treat cluster centres as free parameters. We use S_X and y maps binned with pixel size of 10 or 20 arcsec to reduce computational time, and thus the angular resolution of the central distributions is worse than that in the 1D analysis. Therefore, the two analyses are complementary to each other. We exclude regions around ~ 0.3 arcmin in radius centring radio point or X-ray point sources in computing the log-likelihood.

We also estimates the signal-to-noise ratios of the $\tilde{y}_d$ and $\tilde{S}_X$ radial profiles, defined by

$$(S/N)_y = \left(\sum_{\bar{y}_{d,i} > 0} \frac{\tilde{y}_{d,i}^2}{\sigma_{y,i}^2} \right)^{1/2}, \tag{8}$$

$$(S/N)_X = \left(\sum_i \frac{(\tilde{S}_{X,i} - \tilde{S}_b)^2}{\sigma_{X,i}^2} \right)^{1/2}, \tag{9}$$

where the subscript i denotes the ith radial bin.

3.4 Weak-lensing mass measurement

We describe weak-lensing (WL) analyses of individual clusters. Since the signal-to-noise ratio of the WL data is much lower than those of the X-ray and SZE imaging, we do not include a weak-lensing likelihood in the joint likelihood (equation 7) but independently measure individual cluster masses. The independent analysis has the advantage that it does not impose the assumption of hydrostatic equilibrium (HE) in the modelling (e.g. Okabe & Umetsu 2008).

For the shape measurement, we use the re-Gaussianization method (Hirata & Seljak 2003) which is implemented in the HSC pipeline (see details in Mandelbaum et al. 2018a). Only galaxies satisfying the full-colour and full-depth criteria from the HSC galaxy catalogue were used in both our precise shape measurements and photometric redshift estimations. We select background galaxies behind each cluster, using the colour–colour selection following Medezinski et al. (2018a).

The dimensional, reduced tangential shear $\Delta\Sigma_+$ in the kth radial bin can be computed by azimuthally averaging the measured tangential ellipticity, $e_+ = -(e_1 \cos 2\varphi + e_2 \sin 2\varphi)$:

$$\Delta\Sigma_+(R_k) = \frac{\sum_i e_{+,i} w_i \langle \Sigma_{\mathrm{cr}}(z_l, z_{s,i})^{-1} \rangle^{-1}}{2\mathcal{R}(R_k)(1 + K(R_k)) \sum_i w_i}, \tag{10}$$

(e.g. Medezinski et al. 2018b; Miyaoka et al. 2018; Okabe et al. 2019; Miyatake et al. 2019; Murata et al. 2019). The inverse of the mean critical surface mass density for the ith galaxy is computed by the probability function $P(z)$ from the machine learning method (MLZ; Carrasco Kind & Brunner 2014) calibrated with spectroscopic data

(Tanaka et al. 2018),

$$\langle \Sigma_{\mathrm{cr}}(z_l, z_s)^{-1} \rangle = \frac{\int_{z_l}^\infty \Sigma_{\mathrm{cr}}^{-1}(z_l, z_s) P(z_s) \mathrm{d}z_s}{\int_0^\infty P(z_s) \mathrm{d}z_s}, \tag{11}$$

where z_l and z_s are the cluster and source redshift, respectively. The critical surface mass density is expressed as $\Sigma_{\mathrm{cr}} = c^2 D_s / 4\pi G D_l D_{ls}$, where D_l, D_s, and D_{ls} are the angular diameter distances from the observer to the cluster, to the sources, and from the lens to the sources, respectively. The radius position, R_k, is defined by the weighted harmonic mean (Okabe & Smith 2016). We adopt the same central position as that of 1D SZE and X-ray analysis. The dimensional weighting function is given by

$$w = \frac{1}{e_{\mathrm{rms}}^2 + \sigma_e^2} \langle \Sigma_{\mathrm{cr}}^{-1} \rangle^2, \tag{12}$$

where e_{rms} and σ_e are the root mean square of intrinsic ellipticity and the measurement error per component ($e_\alpha; \alpha = 1$ or 2), respectively. The shear responsivity, $\mathcal{R}$, and the calibration factor, K, are obtained by $\mathcal{R} = 1 - \sum_{ij} w_{i,j} e_{\mathrm{rms},i}^2 / \sum_{ij} w_{i,j}$ and $K = \sum_{ij} m_i w_{i,j} / \sum_{ij} w_{i,j}$ with the multiplicative shear calibration factor m (Mandelbaum et al. 2018a, b), respectively. We also conservatively subtract an additional, negligible offset term for calibration.

We use the NFW profile (Navarro, Frenk & White 1996) for individual cluster mass measurements. The generalized version of the NFW model (gNFW; equations 1–2) is too complicated for low signal-to-noise ratio lensing profiles of individual clusters, and thus its slope parameters cannot be constrained. The gNFW model can be constrained by the stacked lensing profile measured with high signal-to-noise ratio (e.g. Okabe et al. 2013; Okabe & Smith 2016; Umetsu et al. 2016). The 3D mass density profile of the NFW profile is expressed as

$$\rho_{\mathrm{NFW}}(r) = \frac{\rho_s}{(r/r_s)(1 + r/r_s)^2}, \tag{13}$$

where r_s is the scale radius and ρ_s is the central density parameter. The NFW model is also specified by the spherical mass, $M_\Delta = 4\pi \Delta \rho_{\mathrm{cr}} r_\Delta^3 / 3$, and the halo concentration, $c_\Delta = r_\Delta / r_s$. Here, r_Δ is the overdensity radius. We treat M_Δ and c_Δ as free parameters. By integrating the mass density profile along the line of sight, we compute the model of the reduced tangential shear, f_{model}, defined by

$$f_{\mathrm{model}}(R) = \frac{\bar{\Sigma}(<R) - \Sigma(R)}{1 - \mathcal{L}_z \Sigma(R)}, \tag{14}$$

where $\Sigma(R)$ is the local surface mass density at the projected radius R, $\bar{\Sigma}(<R)$ is the average surface mass density within the projected radius R, and $\mathcal{L}_z = \sum_i \langle \Sigma_{\mathrm{cr},i}^{-1} \rangle w_i / \sum_i w_i$. Given the mass model, the log-likelihood of the weak-lensing analysis is described by

$$-2 \ln \mathcal{L}_{\mathrm{WL}} = \ln(\det(C_{km})) + \sum_{k,m} (\Delta\Sigma_{+,k} - f_{\mathrm{model}}(R_k))$$

$$\times C_{km}^{-1} (\Delta\Sigma_{+,m} - f_{\mathrm{model}}(R_m)), \tag{15}$$

where k and m denote the kth and mth radial bins. The covariance matrix, C, is composed of the uncorrelated large-scale structure (LSS), C_{LSS}, along the line of sight (Schneider et al. 1998), the shape noise C_g and the errors of the source redshifts, C_s (e.g. Pratt et al. 2019). The elements of LSS lensing covariance matrix are correlated with each other.

We also carry out the NFW model fitting with a free central position using 2D shear pattern (Oguri et al. 2010). The log-likelihood is

Table 3. Best-fitting gas model parameters. The upper and lower panels are the best-fits by the 1D analysis and the multi-component 2D analysis. The middle panel is the best-fits including the power-law model (pow) of the temperature for HSC J022146.

Name	n_0 $[h_{70}^{1/2} \mathrm{cm}^{-3}]$	$k_B T_0$ $[h_{70}^{1/2} \mathrm{keV}]$	r_s^{gas} $[h_{70}^{-1} \mathrm{kpc}]$	β_n	γ_n	β_T	γ_T
HSC J022146	$4.66^{+1.30}_{-0.70} \times 10^{-3}$	$7.47^{+0.72}_{-0.48}$	$137.48^{+22.46}_{-28.84}$	$0.684^{+0.058}_{-0.033}$	$0.328^{+0.076}_{-0.162}$	$0.315^{+0.115}_{-0.043}$	$-0.106^{+0.101}_{-0.151}$
HSC J023336	$1.34^{+0.43}_{-0.24} \times 10^{-3}$	$7.00^{+1.31}_{-0.86}$	$523.64^{+100.39}_{-187.37}$	$1.308^{+0.272}_{-0.274}$	$0.428^{+0.067}_{-0.134}$	$0.622^{+0.389}_{-0.232}$	$-0.186^{+0.109}_{-0.170}$
HSC J021056	$5.39^{+6.35}_{-1.98} \times 10^{-4}$	$15.41^{+9.22}_{-5.59}$	$525.30^{+629.61}_{-276.15}$	$0.511^{+0.581}_{-0.158}$	$0.579^{+0.052}_{-0.148}$	$0.727^{+0.296}_{-0.246}$	$-0.692^{+0.243}_{-0.685}$
HSC J022146 (gNFW)	$6.96^{+4.33}_{-1.74} \times 10^{-3}$	$6.96^{+1.01}_{-1.04}$	$99.03^{+30.00}_{-26.67}$	$0.795^{+0.304}_{-0.092}$	$0.263^{+0.228}_{-0.675}$	$1.382^{+0.648}_{-0.733}$	$-2.359^{+1.386}_{-1.090}$
HSC J022146 (pow)	–	$0.86^{+1.20}_{-0.50}$	–	–	–	–	$0.973^{+0.521}_{-0.287}$
HSC J023336 (centre)	$9.66^{+5.01}_{-2.82} \times 10^{-4}$	$11.64^{+2.14}_{-2.44}$	$522.28^{+182.34}_{-130.00}$	$1.229^{+0.285}_{-0.316}$	$0.622^{+0.114}_{-0.190}$	$0.914^{+0.345}_{-0.344}$	$-1.370^{+0.720}_{-0.888}$
HSC J023336 (east)	$5.49^{+1.12}_{-0.95} \times 10^{-4}$	$33.91^{+3.82}_{-6.54}$	$322.40^{+28.87}_{-47.54}$	1 (fixed)	0 (fixed)	1 (fixed)	0 (fixed)
HSC J023336 (west)	$3.77^{+1.72}_{-0.82} \times 10^{-4}$	$54.91^{+14.75}_{-14.57}$	322.40 (linked)	1 (fixed)	0 (fixed)	1 (fixed)	0 (fixed)
HSC J021056 (east)	$5.87^{+3.38}_{-2.20} \times 10^{-4}$	$16.37^{+10.03}_{-12.03}$	$485.27^{+203.28}_{-169.00}$	$0.920^{+0.514}_{-0.413}$	$0.566^{+0.334}_{-0.288}$	$1.458^{+0.353}_{-0.419}$	$-1.128^{+0.556}_{-0.739}$
HSC J021056 (west)	$5.10^{+0.58}_{-1.16} \times 10^{-4}$	$14.62^{+0.50}_{-1.43}$	$551.15^{+46.30}_{-70.26}$	1 (fixed)	0 (fixed)	1 (fixed)	0 (fixed)

defined as

$$-2 \ln \mathcal{L}_{\mathrm{WL}} = \sum_{\alpha, \beta=1}^{2} \sum_{k, m} \left[\Delta\Sigma_{\alpha, k} - f_{\mathrm{model}, \alpha}\left(\boldsymbol{R}_k\right) \right] \boldsymbol{C}_{\alpha\beta, km}^{-1}$$

$$\times \left[\Delta\Sigma_{\beta, m} - f_{\mathrm{model}, \beta}\left(\boldsymbol{R}_m\right) \right] + \ln(\det(C_{\alpha\beta, km})). \quad (16)$$

Here, the subscripts α and β denote each shear component. The central positions are restricted to full-width boxes 2 arcmin × 2 arcmin centred on the brightest cluster galaxies (BCGs). The 2D analysis is good at determining the central positions (Oguri et al. 2010) and measuring masses of multicomponents of merging clusters (Okabe et al. 2011, 2015; Medezinski et al. 2016).

In actual analyses, the maximum radial range to compute $\Delta\Sigma_\alpha$ is determined by excluding neighbouring, massive CAMIRA clusters to avoid their contamination in lensing signals. We adopt an adaptive radial-bin choice (Okabe et al. 2016) for cluster mass estimation. The shape catalogue in the central region of HSC J021056-061154 is not provided because the region does not satisfy the full-colour and full-depth condition of the shape measurement. We thus measure WL masses without the central region of HSC J021056-061154.

4 RESULTS AND DISCUSSION

4.1 HSC J022146-034619

4.1.1 Joint analysis

As shown in the top panel of Fig. 1, the 2D distributions of the member galaxies, y-parameter and X-ray surface brightness have a single peak around the BCG, coinciding within the PSF or smoothing scale of the observation. The y and S_X distributions exhibit regular morphology, while the red member galaxy distribution is elongated to the north-west direction.

We measure the y and S_X radial profiles, and fit them with the gNFW model (equations 1–2) using uniform priors. In order to discriminate between the actual observations and the non-convolved models, we represent the observations by $\tilde{y}_d$ and $\tilde{S}_{Xd}$ (equation 7). The best-fitting parameters are summarized in Table 3. The best-fitting y and S_X profiles are shown by the blue solid line in the top-left and top-middle panels of Fig. 3. Due to the transfer function (see Fig. 2) of the MUSTANG2 observation, the observed and best-fitting y profiles sharply decrease at $\theta > 1$ arcmin. In a very central

region of $\theta \lesssim 0.07$ arcmin ~ 4 arcsec ($R \lesssim 20$ kpc) comparable to BCG scale, we find a 3σ discrepancy between the observed $\tilde{y}_d$ profile and the best-fitting $\tilde{y}$ profile. Although we dropped the assumptions of α and r_T in the gNFW profiles, the excess of the y-parameter cannot be explained by the gNFW model alone. In order to solve the discrepancy, we add the power-law model for the temperature profile (equation 17) to the gNFW temperature model (equation 2); $T_e = T_{\mathrm{gNFW}} + T_{\mathrm{pow}}$. The power-law model is specified by

$$T_e = T_{p0} \left(\frac{r}{r_0} \right)^{-p}, \quad (17)$$

where T_{p0} is the normalization, $r_0 = 1$ kpc is a pivot radius, and p is a slope. We refer to it as a gNFW+T_{pow} model. The best-fitting parameters are summarized in the middle panel of Table 3 and shown by the green dashed lines in Fig. 2. The best-fitting profiles for the gNFW and gNFW+T_{pow} models are in good agreements at $\theta > 0.07$ arcmin.

The bottom panels of Fig. 3 are, from left to right, the 3D profiles of the pressure, the electron number density, and the electron temperature. The errors shown by blue and green transparent regions are calculated by the error covariance matrix. The electron pressure profiles for the gNFW model and the gNFW+T_{pow} model have a flat core and a cuspy structure, respectively. The electron number density profiles for the two models are similar to each other. We compare with the deprojected electron number density and find a good agreement. The electron temperature profile for the gNFW model has a flat core, while the gNFW+T_{pow} model has a steep profile. The two profiles at $r > 200$ kpc agree well with each other. We note that the temperature uncertainty of the gNFW+T_{pow} model is larger than the number density or pressure uncertainties, because the number density and pressure are directly linked to the y and S_X profiles in the likelihood. The uncertainty introduced by the additional power-law temperature distribution is anticorrelated with that of the number density in order to reproduce the y and S_X profiles. The temperature uncertainty of the gNFW model is smaller than that of the gNFW+T_{pow} model, because the gNFW temperature profile is sensitive to the y and S_X profiles with small measurement errors at large radii.

We also measured X-ray temperature using deep X-ray data based on the X-COP method (Eckert et al. 2017). In X-ray temperature measurements of the first and second inner bins, we consider a mixture of incoming photons at each annulus using CROSS-ARF in XSPEC. The X-ray temperature profile agrees well with the SZE
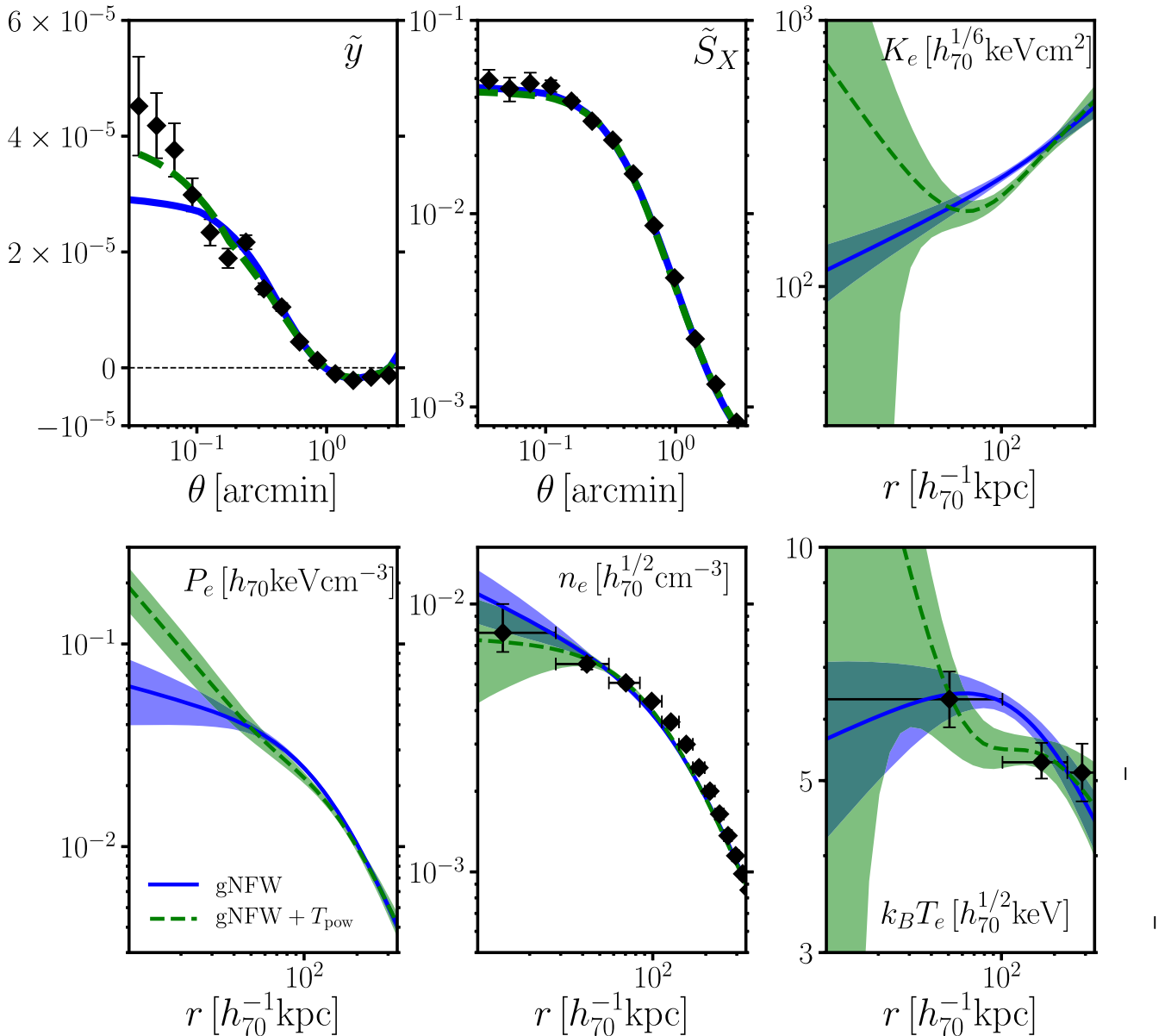
Figure 3. *Top*: $\tilde{y}$ (left) and $\tilde{S}_X$ (middle) profiles of HSC J022146-034619. The signal-to-noise ratios computed by the observed $\tilde{y}_d$ and $\tilde{S}_{Xd}$ profiles are $\sim 36\sigma$ and $\sim 100\sigma$, respectively. They are computed from equations (8) and (9). The blue solid and green dashed lines are the best-fitting gNFW and gNFW+$T_{\rm pow}$ models derived from the joint SZE and X-ray analysis, respectively. The right-hand panel shows the entropy index profile (K_e) computed from the bottom panels. The blue and green transparent regions are their 1σ errors. *Bottom*: 3D profiles of the best-fitting pressure (P_e, left), density (n_e, middle), and temperature (k_BT_e, right). The black diamonds in the middle panel denote the model-independent, deprojected profile of the electron number density. The black diamonds in the right-hand panel are X-ray temperature measured by deep X-ray data.

temperature profiles. However, the emission-weighted temperature using the XXL temperature ($4.2^{+0.5}_{-0.7}$ keV; Table 1) within 300 kpc is slightly lower than the X-COP measurement using deep X-ray data, but the discrepancy is only 2.3σ level.

We measure weak-lensing masses using a tangential shear profile (the left-hand panel of Fig. 4 and Table 4). A comparison of weak-lensing and HE masses is discussed in Section 4.8.

4.1.2 Sloshing feature

Both the S_X and y distributions for HSC J022146-034619 exhibit regular morphology in the sky plane in contrast to the other two clusters. However, in the gNFW profile alone it is difficult to explain

the excess in the observed $\tilde{y}_d$ profile at very central region of $\theta \lesssim 4''$, corresponding to $R \lesssim 20$ kpc, as shown in Fig. 3. The radial size is comparable to the beam radius. The excess requires the additional hot component. Since the 3D profiles computed with and without the hot component agree well with each other on large scale, the global gas structure does not change and only local modification occurs. We also assume an elliptical gNFW temperature model elongated along the line of sight for fitting, but found it difficult to explain the excess by the reasonable parameter choices. Therefore, the feature implies that the gas is locally interacting, heated, or perturbed.

A clearer display of this feature is shown in Fig. 5, where we compute fractional residual S_X and y maps between the observed images and average images. The residual images ($\delta \tilde{S}_X$ and $\delta \tilde{y}$) are
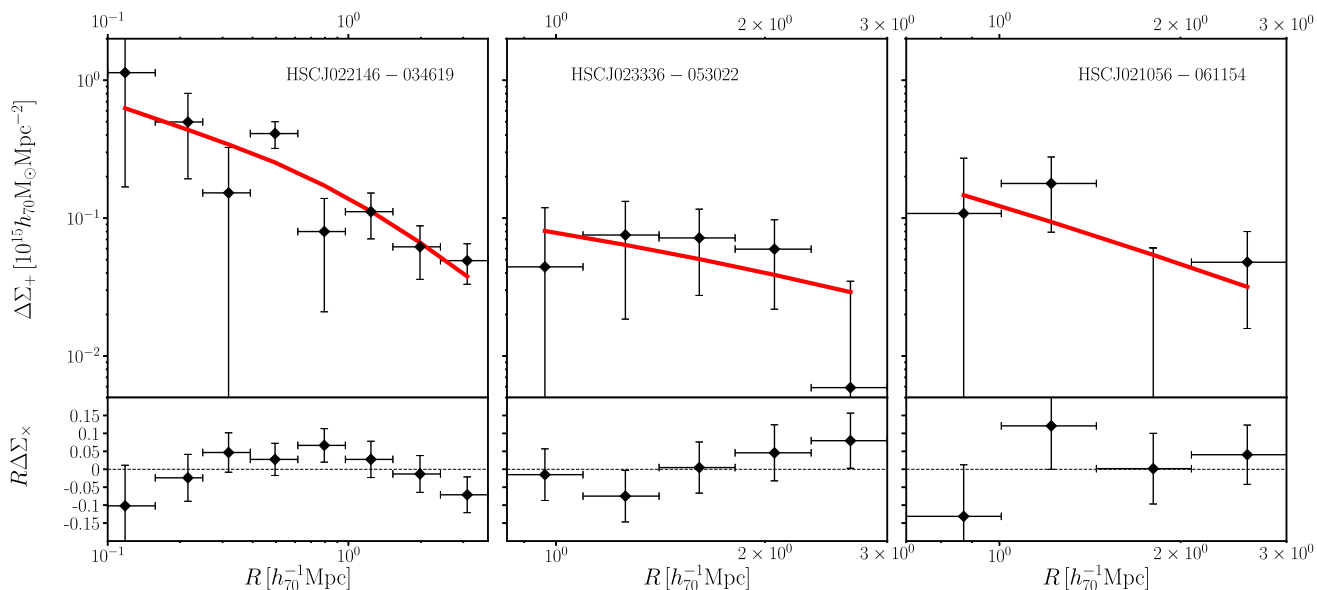
Figure 4. *Top*: Tangential shear profiles for the three subsamples of HSC J022146-034619, HSC J023336-053022, and HSC J021056-061154 (from left to right). *Bottom*: The product ($10^{15} h_{70} \mathrm{M_\odot Mpc^{-1}}$) of the 45 degree rotated component, $\Delta \Sigma_\times$, with the projected distance, R, as a function of R.

Table 4. WL masses.

Name	M_{200} $[10^{14}\,h_{70}^{-1}\mathrm{M_\odot}]$	M_{500} $[10^{14}\,h_{70}^{-1}\mathrm{M_\odot}]$
HSC J022146-034619	$8.34^{+3.22}_{-2.49}$	$5.69^{+1.65}_{-1.43}$
HSC J023336-053022[a]	$2.46^{+1.27}_{-1.08}$	$1.51^{+0.86}_{-0.71}$
HSC J021056-061154[b]	$5.42^{+3.84}_{-3.84}$	$4.30^{+3.01}_{-3.25}$

[a]Mass computed from 2D WL analysis. [b]Shape catalogue in the central region is not available.

derived by subtracting the averaged images. The average images are computed by azimuthally averaged profiles through interpolation and thus free from any assumptions of analytical models. We then normalize them by the averaged images and obtain $\delta \tilde{S}_X / \langle \tilde{S}_X \rangle$ and $\delta \tilde{y} / \langle \tilde{y} \rangle$ to consider the radial dependence of $\langle \tilde{S}_X \rangle$ and $\langle \tilde{y} \rangle$. For *XMM-Newton*, there is a large CCD gap in the PN detector around the central region, and the residual map is computed from the MOS1 and MOS2 detectors. Since there are small CCD gaps even in MOS1 and MOS2, we independently compute $\delta \tilde{S}_X / \langle \tilde{S}_X \rangle$ excluding CCD gaps and then combined the two residual maps. For MUSTANG-2, the $\tilde{y}$ profile is negative at $\theta \gtrsim 1$ arcmin, and we thus mask the region to $\theta > 0.8$ arcmin. Since the XMM pixel size (2.5 arcsec) is different from the MUSTANG-2 pixel size (1 arcsec), we computed the residual y map using the XMM pixel size. Since the two residual maps are still noisy, we adopt Gaussian smoothing with $\sigma = 8$ arcsec which is the same as Fig. 1. To avoid the masked region in the residual y map, we conservatively limit the region at $\theta < 0.5$ arcmin at which $\tilde{y}$ is almost constant (Fig. 3). The resulting residual maps are shown in Fig. 5. Positive and negative excesses appear in the northern and southern areas in the two maps. The sums of the signal-to-noise ratios of the deviations ($\delta \tilde{y}$ and $\delta \tilde{S}_X$) in every pixel within 0.5 arcmin from the centre are 3.5σ in $\delta \tilde{y}$, 5.0σ in $\delta \tilde{S}_X$, and 6.1σ in total. The residual patterns are coherently distributed, which indicates a presence of gas sloshing. The gas disturbances could also trigger local heating (e.g. Ascasibar & Markevitch 2006; ZuHone, Markevitch & Johnson 2010; Vazza, Roediger & Brüggen 2012). Even when we use the BCG position as the central position (Fig. 6), these coherent residual pattern does not

disappear. We quantify the pixel-to-pixel cross-correlation between the residual patterns with different centres and find the correlation coefficients of 0.86 in $\delta \tilde{y} / \langle \tilde{y} \rangle$ and of 0.97 in $\delta \tilde{S}_X / \langle \tilde{S}_X \rangle$.

It is difficult to search by photometric information for a subhalo that triggered the sloshing mode. A large number of spectroscopic redshifts will be crucial to identity the subhalo, but only nine redshifts are available to date. Since the red galaxy distribution (Okabe et al. 2019) could not offer clues on the subhaloes location within R_{200}, two subhalo candidates can be expected. The first candidate is a subhalo within the smoothing scale of 200 kpc from the BCG and the second candidate is a less massive subhalo.

There is a second luminous galaxy at $(\alpha, \delta) = (35.4382, -3.7673)$ which is 106 kpc north-west from the BCG. Its stellar mass is about one-fourth that of the BCG. The presence of the second brightest galaxy (the second BCG) is not rare in optical clusters. We perform the 2D WL analysis using a single NFW model and its free central location. The resulting centre is close to the second BCG rather than the BCG (Table 5 and Fig. 6). Although the two galaxies are too close to resolve their mass structures by WL analysis, the position would be explained by the superposition of the mass associated with the second bright galaxy and the main halo. If the difference in their redshifts gives their relative peculiar velocity along the line of sight, $v = c\delta z/(1 + z) \sim 450\,\mathrm{km\,s^{-1}}$ is likely to be subsonic motion. Therefore, the scenario that the moving second BCG triggers the hot component and sloshing pattern does not qualitatively contradict the observational results.

To search for a second halo candidate, we next made a galaxy number map of red and blue galaxies selected by full probability function of the photometric redshift (Tanaka et al. 2018). Following Ichikawa et al. (2013) to map the surrounding galaxy distribution on the large scale, we compute a probability of each galaxy located at a slice of $\pm \Delta z$, defined by

$$p_{\mathrm{gal}} = \int_{z_l - \Delta z}^{z_l + \Delta z} P(z)\mathrm{d}z \bigg/ \int_0^\infty P(z)\mathrm{d}z, \qquad (18)$$

where $P(z)$ is the full probability function, z_l is a cluster redshift, and Δz is the redshift slice. Taking into account photometric redshift
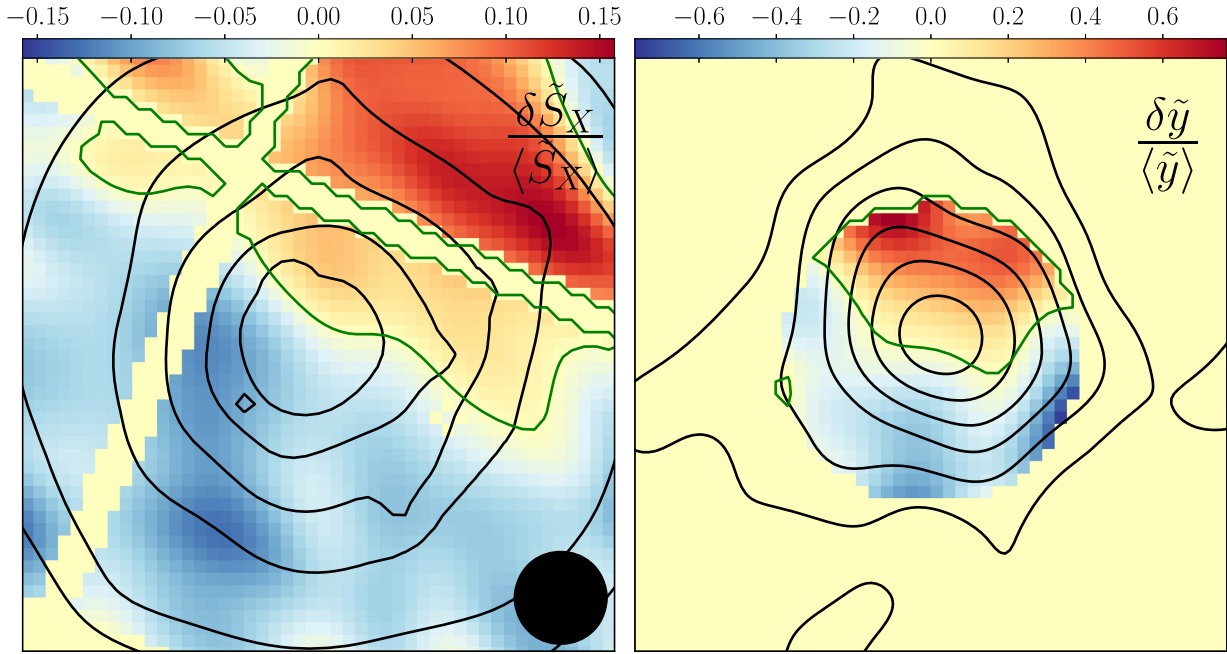
Figure 5. Fractional residual maps of the X-ray surface brightness (left) and the *y* parameter (right) of the box of 2 arcmin × 2 arcmin of HSC J022146-034619, centring with the XXL centre. The mean X-ray surface brightness and *y* are interpolated from the azimuthally averaged profiles. *Left*: the residual S_X map as computed from MOS1 and MOS2. The CCD gaps are evident as a cross-pattern. Green contours are $\delta \tilde{S}_X = 0$. The black circle at the lower right corner shows the FWHM circle of the smoothing scale ($\sigma = 8$ arcsec) in order to reduce noisy feature. Black contours is $\tilde{S}_X$ distribution which is the same as in the top-middle panel of Fig. 1. *Right*: the residual *y* map on the XMM grid of 2.5-arcsec pixels. The map is masked outside $\theta = 0.5$ arcmin, where $\tilde{y}$ is of low signal/noise. The smoothing is applied as in the left-hand panel. Green contours are $\delta \tilde{y} = 0$. Black contours are the $\tilde{y}$ distribution which is as in the top left-hand panel of Fig. 1.
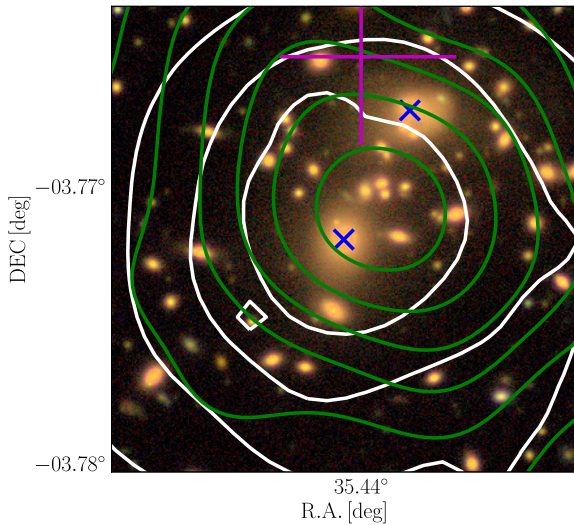
Figure 6. Optical *riz*-colour image around the BCG of HSC J022146-034619 (1 arcmin × 1 arcmin). The white and green contours denote *y* and S_x distributions (Fig. 1). The blue crosses represent the central BCG and the second brightest galaxy at the north-west. The large magenta symbol marks the WL-determined centre and its error.

errors, we adopt $\Delta z = 0.1$ in a similar way to Eckert et al. (2017). The galaxy number distribution is shown in the right-hand panel of Fig. 7. The galaxy distribution is elongated along the north–south direction. The spectroscopically identified galaxies (Guglielmo et al. 2018) are shown by red pluses. A galaxy group is found around (α, δ) = (35.4087, −3.8252) which is at ∼1.3 Mpc south of the BCG. The group is mainly composed of red luminous galaxies. Diffuse

Table 5. Centres determined by 2D fitting analyses.

Component	α (deg)	δ (deg)
HSC J022146-034619		
Gas	$35.4389^{+0.0001}_{-0.0001}$	$-3.7705^{+0.0001}_{-0.0001}$
Mass	$35.4400^{+0.0029}_{-0.0034}$	$-3.7653^{+0.0041}_{-0.0032}$
HSC J023336-053022		
Gas C	$38.4081^{+0.0009}_{-0.0010}$	$-5.5052^{+0.0014}_{-0.0010}$
Gas W	$38.3889^{+0.0007}_{-0.0010}$	$-5.5053^{+0.0004}_{-0.0004}$
Gas E	$38.4153^{+0.0020}_{-0.0007}$	$-5.5016^{+0.0006}_{-0.0005}$
Mass W	$38.3895^{+0.0058}_{-0.0072}$	$-5.5030^{+0.0051}_{-0.0068}$
Mass E	$38.4178^{+0.0067}_{-0.0103}$	$-5.5069^{+0.0062}_{-0.0070}$
HSC J021056-061154		
Gas E	$32.7338^{+0.0010}_{-0.0035}$	$-6.1975^{+0.0010}_{-0.0009}$
Gas W	$32.7208^{+0.0021}_{-0.0035}$	$-6.1998^{+0.0018}_{-0.0027}$
Ell Gas E	$32.7358^{+0.0022}_{-0.0015}$	$-6.1978^{+0.0007}_{-0.0008}$
Ell Gas W	$32.7228^{+0.0009}_{-0.0011}$	$-6.2003^{+0.0013}_{-0.0015}$

X-ray emission is also found around (α, δ) = (35.4269, −3.8115) which is ∼0.8 Mpc south of the BCG and at ∼0.4 Mpc north of the southern galaxy group. The X-ray contours along the line connected between the X-ray main peak and the southern X-ray emission is slightly curved outwards. One of possible interpretations is that the subhalo passed through the cluster centre and gas was stripped away by ram-pressure. Since the southern galaxy group is compact and less massive, we measure its projected mass following a subhalo mass measurement (Okabe et al. 2014b). The projected mass, $M_{\zeta_c} = 3.5 \pm 0.8 \times 10^{13} M_\odot$, is only about 1/25 of the main halo.
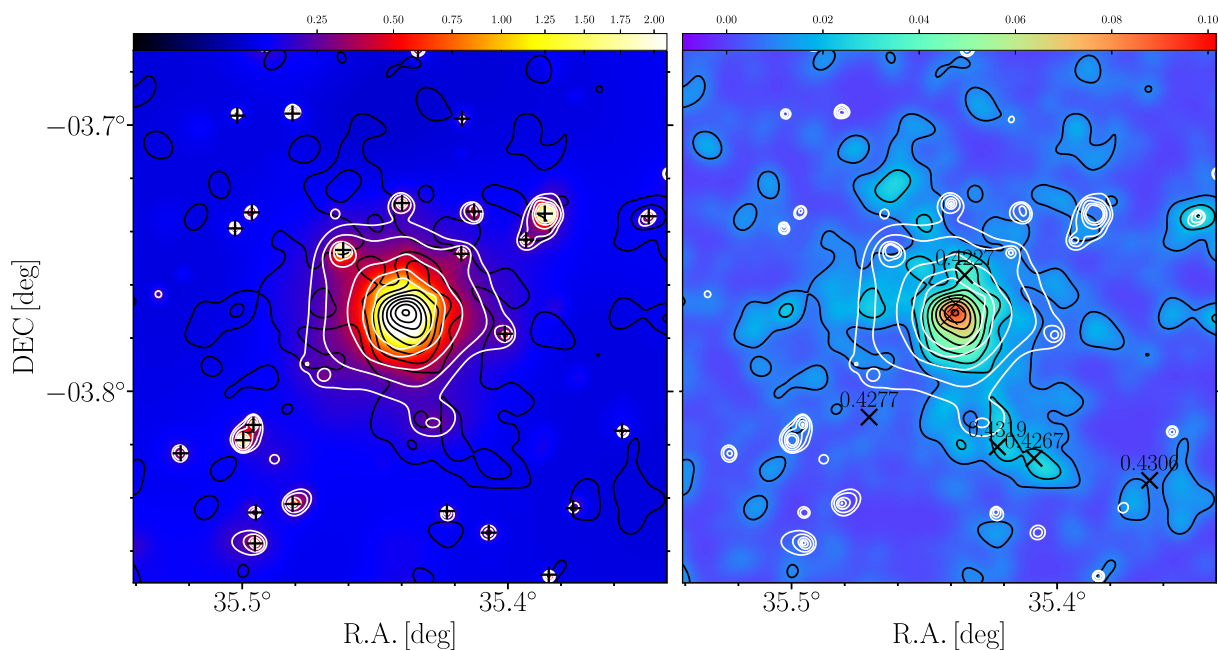
Figure 7. Adaptively smoothed X-ray map (left) and galaxy distribution (right) sliced by photometric redshift probability function $P(z)$ for HSC J022146-034619. The full-width size is 12 arcmin. *Left*: The X-ray tailed feature from the cluster centre to the southern region is marginally found. Black pluses denote X-ray point sources or foregrounds identified by cross-matching optical and X-ray images. White and black contours are X-ray and galaxy distributions, respectively. *Right*: The galaxy number density distribution smoothed with FWHM = 200 kpc. Black X points are spectroscopically identified galaxies of which redshifts are shown in black texts, excluding the BCG and second bright galaxy. The galaxy distribution is elongated along the north and south direction on large scale. X-ray faint galaxy substructure is found around (35.4087, −3.82514). If the galaxy substructure were passing from the cluster centre to the south, it could trigger the sloshing mode in the central region.
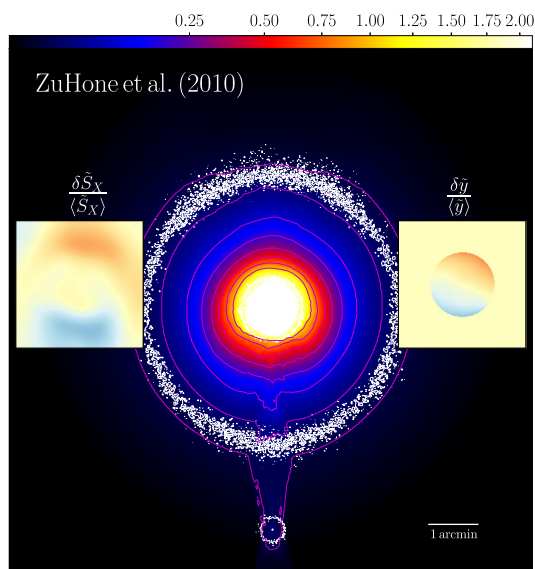
Figure 8. One of examples of simulated sloshing images retrieved from ZuHone et al. (2010, 2018). White and magenta contours are projected mass and X-ray surface brightness distributions, respectively. Inset panels are fractional residual $\tilde{S}_X / \langle \tilde{S}_X \rangle$ (left) and $\tilde{y} / \langle \tilde{y} \rangle$ maps (right) taking account of the PSFs and the transfer function of the box of 2 arcmin × 2 arcmin. The appearance of the residual images resembles our residual images (Fig. 5). The configurations of the X-ray and mass clumps are similar to those in Fig. 7.

Since having a less massive halo fall into a cluster occurs fairly often we cannot make a conclusive statement about which subhalo triggered the sloshing mode. Systematic future spectroscopic observations will reveal the details.

4.1.3 Comparison with numerical simulations

ZuHone et al. (2010) studied sloshing features in the gas core using *N*-body/hydrodynamic numerical simulations for which data is publicly available (ZuHone et al. 2018). In order to visually understand the observed feature, we compute mock residual maps of simulated clusters at the cluster redshift considering the PSFs and the transfer function. We use the data set of $M_{200} = 10^{15} M_\odot$ for the main cluster and a subhalo with mass ratio 1 : 20 and impact parameter of 200 kpc. The sloshing modes appeared in all phases after the first impact. The direction of residual emission and pattern depend on the viewing angle. We pick a phase at 2.5 Gyr after the closest encounter as a typical example. At this phase, the subhalo is on its way to the second impact after turnaround. Fig. 8 is an edge-on view from the merger plane for the simulated S_X and mass distributions. The subhalo is located at the south and a tailed gas feature is found. Inset figures are the fractional residual maps convolved with the PSFs and the transfer function excluding any observational noise. The coherent residual patterns and the location of the subhalo are similar to our observation (Figs 5 and 7).

4.2 HSC J023336-053022

4.2.1 Joint analysis

The *y* map shows a clear double-peaked structure associated with galaxy concentrations (the middle horizontal panel of Fig. 1). An X-ray core with a round shape is found at the intermediate position between the two high *y*-components. The X-ray core can be visually decomposed into two substructures. The X-ray peak coincides with the positions of the eastern *y* and galaxy structures. The secondary X-ray peak is located close to a surface-brightness weighted centroid. The *y* parameter around the X-ray morphological centre is lower than
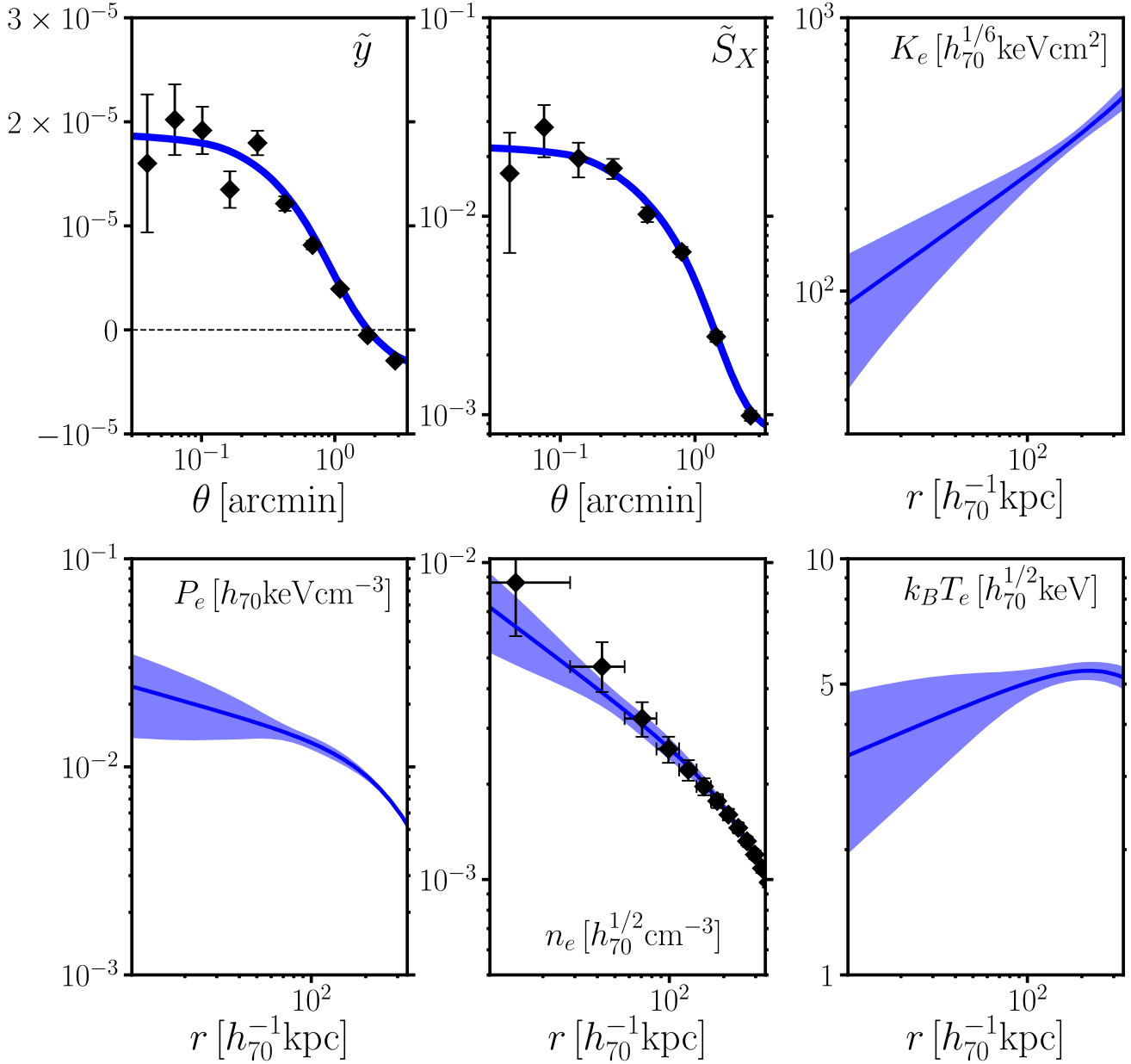
Figure 9. The same figure as Fig. 3, but for HSC J023336-053022. The signal-to-noise ratios of the $\tilde{y}_d$ and $\tilde{S}_{Xd}$ profiles are $\sim 36\sigma$ and $\sim 24\sigma$, respectively.

those of the double-peaked y-components. The high density and low pressure suggests that the X-ray core is likely to be a cool core. A possible scenario explaining the observed feature is that two clusters with cool cores are colliding with each other and two shock-heated regions are triggered ahead of the gas cores. The cluster is likely to be at a phase just after core passage.

As a first attempt at modelling, we assume a spherically symmetric gas distribution in a similar way as the other clusters (Sections 4.1 and 4.3), though the y and S_X distributions are composed of the three gas components. The azimuthally averaged y profile (the top-left panel of Fig. 9) is almost constant at small radii and steeping at $\theta \sim 1$ arcmin because of the angular transfer function. For this cluster, we choose an X-ray count-rate weighted centre within 100 kpc of the X-ray peak, because we find the S_X and y profile centres are misaligned with the XXL centre. As expected from the observed y profile, the modelled pressure profile has a shallow slope. The electron number density shows a steeply decreasing function and agrees with the

model-independent, deprojected electron number density. The temperature profile slightly increases as the radius increases to compensate for the steep function of the electron number density. The X-ray-like emission-weighted, projected temperature ($k_B T_{\mathrm{SZ+X}}$) within 300 kpc is $5.2^{+0.3}_{-0.3}$ keV.

We next perform a multicomponent analysis to model the double-peaked y structure and single S_X structure. The peak signal-to-noise ratios of the western and eastern y structures are 3.4 and 4.5σ, respectively. The signal-to-noise ratios (equation 8) of the $\tilde{y}_d$ profiles within an 0.5 arcmin circle centred on the two peaks are 21.7σ and 27.9σ, respectively. The signal-to-noise ratio of the $\tilde{S}_X$ profile within 0.5 arcmin centring the X-ray peak is 15.9σ. We therefore introduce three gas components as a function of 3D space, $\boldsymbol{x}$,

$$g(\boldsymbol{x}) = g_{\mathrm{gNFW}}^{\mathrm{C}}\left(\boldsymbol{x}_c^{\mathrm{C}}; \boldsymbol{x}\right) + g_\beta^{\mathrm{W}}\left(\boldsymbol{x}_c^{\mathrm{W}}; \boldsymbol{x}\right) + g_\beta^{\mathrm{E}}\left(\boldsymbol{x}_c^{\mathrm{E}}; \boldsymbol{x}\right), \qquad (19)$$

where $g = n_e$ or $g = T_e$ and $\boldsymbol{x}_c$ is the central position. The subscript and superscript denote the type of models and central positions, respectively. We adopt the gNFW model for the central gas component in order to express the presence of the cool core. In order to describe the western and eastern hot-thin regions, we adopt the β model for simplicity. Since the outer slopes of the number density and temperature profiles of the two hot regions cannot be constrained well, we fixed the slope $\beta_n = \beta_T = 1$. The slope is much steeper than the typical value of clusters derived by X-ray surface brightness profile (e.g. Pacaud et al. 2016, $\beta \sim 0.67$) in order to describe the gas locally heated by cluster merger shocks. We also assume that the scale radii of the western and eastern components are the same. In other words, the differences between the western and eastern gas properties are described by the central temperature and density values.

When we compute the projected y and S_X distributions, we assume that the two gas components do not interact with each other. We treat central positions as free parameters, restricted to boxes of 1 arcmin × 1 arcmin centred on the brightest cluster galaxies of the western and eastern components and the cool core for the W, E and C components, respectively. We use 2D images binned by ten pixels for the y map and four pixels for the S_X map, respectively. The pixel sizes of the two binned images correspond to 10 arcsec.

The resulting model maps and parameters are shown in Fig. 10 and Table 3, respectively. The best-fitting centres are shown in Table 5. The model maps do not take into account the transfer function and the PSFs to understand distributions of physical properties. The models succeed in reproducing the double-peaked distribution of the y distribution (top-left panel) and the single cool core (middle and bottom panels). The X-ray distribution is completely different from the WL mass distribution, as usual in on-going mergers (Okabe & Umetsu 2008). The X-ray-like emission-weighted, projected temperature ($k_B T_{SZ+X}$) of the central cluster component changes from ∼2 keV at the cool core to ∼7 keV at an intermediate radius of 2.5 arcmin. The temperature within 300 kpc from the best-fitting centre agrees with the expectation from the WL mass (Section 4.6). Although the temperature of the intermediate radius is slightly higher than expected from the WL mass, $\tilde{y}$ at the radius is negative due to the transfer function. The X-ray-like emission-weighted projected temperatures within the projected radius 300 kpc from the same centre of the 1D analysis is $k_B T_{SZ+X} = 6.6^{+1.4}_{-1.3}$ keV which agrees with that of the 1D analysis within the ∼1.1σ of the 2D analysis. We here take into account the full error covariance matrix of the gas parameters. The X-ray-like emission-weighted projected temperatures within the projected radius 300 kpc from the best-fitting centres in the western and eastern hot components (see details in Sections 4.5 and 4.6; $k_B T_{SZ+X}$) are $28.4^{+5.9}_{-6.0}$ keV and $20.2^{+3.5}_{-3.4}$ keV, respectively. We note that the projected temperatures depend not only on the normalization T_0 but also on the overall temperature and density distributions. The uncertainties in the projected temperatures fully take into account the error covariance matrix of the gas parameters.

When we include the cool component, the projected temperature in the western and eastern regions are $11.3^{+1.6}_{-1.6}$ keV and $6.8^{+1.4}_{-1.3}$ keV, respectively. We note that a relativistic correction is small in the observing frequency (e.g. Hughes & Birkinshaw 1998; Mroczkowski et al. 2019). Their temperatures are three or four times higher than that of the cool component in the same regions. However, the electron number density of the two hot regions is lower than that of the cool component. We compute the integral of the electron density over a cylindrical volume within a projected radius of 300 kpc from the best-fitting central position of the western/eastern component. The ratios of the electron number of the western/eastern component to

the total component are 0.45/0.38, respectively. It thus indicates that a small fraction of the ICM is locally heated by the cluster merger.

If we assume that the outer slope for the hot component is $\beta = 2$, the normalized temperatures, T_0, in the western and eastern hot components become lower by ∼20 per cent and by ∼6 per cent, respectively. Since the other parameters are also accordingly changed, the cylindrical temperatures of all the components, the western hot component and the eastern hot component within 300 kpc, change by only −2, −10 and −2 per cent, respectively, less than the 1σ uncertainty.

We compare the Akaike information criterion (AIC) and Bayesian information criterion (BIC) of the multi-component analysis with those of the single gNFW model (g^C_{gNFW}) analysis using the two dimensional y and S_X images. The differences are $\Delta \text{AIC} = \text{AIC}_{\text{multi}} - \text{AIC}_{\text{gFNW}} = -709 < 0$ and $\Delta \text{BIC} = \text{BIC}_{\text{multi}} - \text{BIC}_{\text{gFNW}} = -656 < 0$, respectively. Therefore, the additional two components based on visual inspections improve the modelling.

A future joint analysis of the high angular resolution, MUSTANG-2 data with the small FOV, and the mid-angular resolution SZE data (e.g. AdvACT; ∼1 arcmin) covering larger area would be helpful to constrain well the outer slopes of the gas temperature and density distributions and improve the parameter degeneracy caused by the transfer function. Although this study assumes the gNFW model (or β model), the shape of cluster merger shock surface could be a paraboloid-like feature and the asymmetric gas distribution model would be powerful in a future analysis. The geometrical assumption is also important for the deprojection and the volume-filling factor of each component in the three dimensional space.

To measure cluster richnesses of the western and eastern components, we split into two galaxy components by right ascension of a bright galaxy ($\alpha = 38.3991$) around the cool core. Based on the S16A catalogue (Aihara et al. 2018b; Oguri et al. 2018), the richness of the western and eastern galaxies are 25 and 14, respectively. The total stellar masses are $M^W_* = 3 \times 10^{12} M_\odot$ and $M^E_* = 10^{12} M_\odot$. When we use the S18A catalogue (Aihara et al. 2019), the result does not significantly change: $M^W_* = 3 \times 10^{12} M_\odot$ and $M^E_* = 2 \times 10^{12} M_\odot$. Since cluster richness and halo mass are positively correlated (Okabe et al. 2019), the western galaxy component is likely to be the main cluster.

We measure weak-lensing mass using a tangential shear profile (Fig. 4) and multicomponent masses by a 2D weak-lensing analysis using a 2D shear pattern (Okabe et al. 2011, 2015; Medezinski et al. 2016). Since the concentration parameters of the two haloes and the mass of the subcluster are ill-constrained (because of a small number of background galaxies), we assume the mass–concentration relation in Diemer & Kravtsov (2015). The central positions of the two haloes are treated as free parameters in a similar way as the 2D SZE and X-ray analysis.

We first fit with uniform priors and obtain $M^W_{200} = 1.28^{+1.17}_{-0.65} \times 10^{14} h^{-1}_{70} M_\odot$ and $M^E_{200} < 0.75 \times 10^{14} h^{-1}_{70} M_\odot$. This indicates that the western component is the main cluster, consistent with its higher richness. The central positions determined by WL analysis, shown in Table 5, coincide with BCG positions of the two galaxy components. Since we give an upper limit of the mass of the eastern component, we repeat fitting with fixed centres at best-fitting positions. The individual halo masses are $M^W_{200} = 1.54^{+1.29}_{-0.66} \times 10^{14} h^{-1}_{70} M_\odot$ and $M^E_{200} = 0.90^{+0.99}_{-0.40} \times 10^{14} h^{-1}_{70} M_\odot$. The best-fitting mass ratio between the subcluster and the total cluster is roughly 2:3. Considering the error matrix, the mass ratio is $0.54^{+0.93}_{-0.28}$. The resulting matter distribution is shown by the red lines in Fig. 10. Even when we fit the entire shear pattern with a single NFW model, the best-fitting centre is consistent with the western BCG position rather than the eastern BCG position, indicating that the western component is the main cluster.
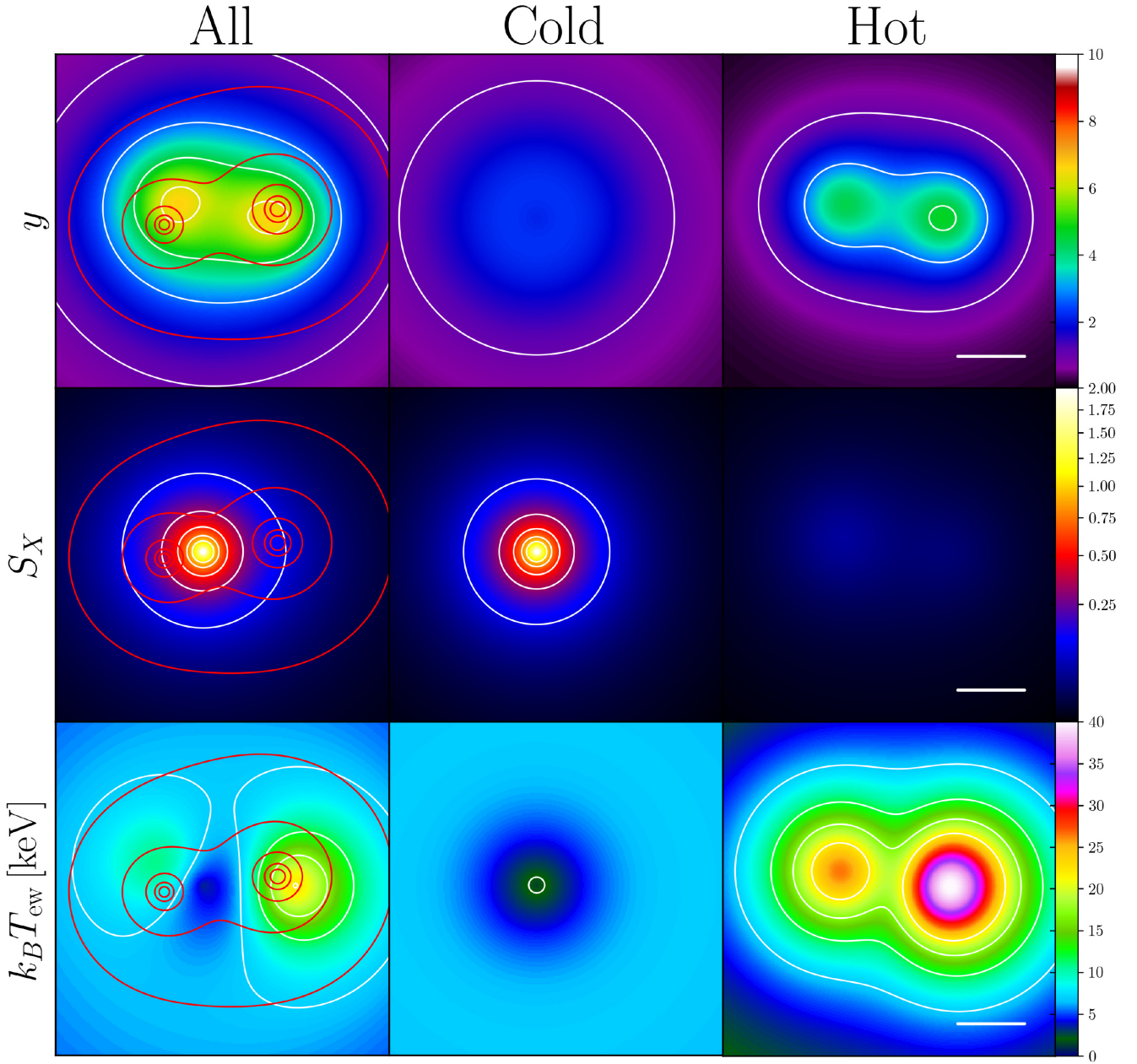
Figure 10. Model maps for HSC J023336-053022: y map $[10^{-5}]$ (top), S_X map in arbitrary units (middle), and X-ray-like emission-weighted temperature, $k_B T$ [keV] (bottom). The full-width size is 5 arcmin. Neither the transfer function nor the PSF has been applied. From left to right, the panels show the total gas components, the cold gas component, and the hot gas component, respectively. The red contours denote the projected mass contours derived by 2D WL analysis ($[0.1, 0.3, 1.1, 2.3, 4] \times 10^{14} M_\odot \, \text{Mpc}^{-2}$, stepped by square root). The white lines shown in the right-hand panels denote 1 arcmin.

4.2.2 Merger dynamics

The offsets in the y and S_X distributions (Figs 1 and 10) show violent merger phenomena, indicating that the merger is at the phase just after core-passage. Even so, we first discuss whether the possibility of a pre-merger phase can be ruled out or not. The expected masses given the measured temperatures of >20 keV associated with the eastern and western mass structures are $M_{500}^E = 4.5^{+1.4}_{-1.2} \times 10^{15} h_{70}^{-1} M_\odot$ and $M_{500}^W = 7.9^{+2.9}_{-2.5} \times 10^{15} h_{70}^{-1} M_\odot$, respectively. We assume that the clusters follow the mass–temperature scaling relation (Lieu et al. 2016; see also Section 4.6). The numbers of clusters with masses higher than the estimated masses are expected to be $N_{clu}^E < \mathcal{O}(10^{-5})$ and $N_{clu}^W < \mathcal{O}(10^{-7})$ in the overlapped footprint of the HSC-SSP and XXL surveys of 24.1 deg^2 and the redshift slice of $|\Delta z| <$

0.1 around the cluster redshift. The upper limits are constrained by the lower uncertainty bounds of the temperatures. We here assume the mass function of Tinker et al. (2008) with *Planck* cosmology (Planck Collaboration VI 2020). Therefore, the hypothesis that the cluster is at the pre-merger is unlikely from the point of view of the concordance cosmology. When we include the cool component, $N_{clu}^W \lesssim 0.04$ and $N_{clu}^E \lesssim 0.7$ and thus the result does not change.

We estimate the merger time-scale after core passage. Since dark matter is likely composed of collisionless particles, the WL-determined central position can constrain the merger time-scale (Okabe et al. 2011, 2015). From the 2D WL analysis (Section 4.2), assuming a point mass approximation, the projected distances between the two clusters and between the subhalo and the centre of

mass are estimated to be ~580 kpc and ~370 kpc, respectively. They are lower than the 3D overdensity radii, $r_{200} = 1212.3^{+219.2}_{-227.1}$ kpc and $r_{500} = 782.3^{+149.9}_{-191.0}$ kpc, which are derived by 2D WL analysis (Table 4 and Section 3.4). Okabe et al. (2019) found a segregation in a probability density function (PDF) of collision velocities of the optically defined merging clusters and well-known merging clusters with diffuse synchrotron radio emissions. The peak velocities of the optically defined merging clusters and merging clusters with diffuse radio emissions are $\sim 1000 \, \mathrm{km \, s^{-1}}$ and $\sim 2500 \, \mathrm{km \, s^{-1}}$, respectively. The former and latter cases give the merger time-scales after core passage of ~0.36 Gyr and ~0.14 Gyr, respectively.

We also estimate the merger velocity from the deviation from a mass–temperature scaling relation (Lieu et al. 2016). Assuming that the gas temperature before the merger follows the mass–temperature scaling relation (see details in Section 4.6), we infer a pre-merger temperature from the eastern WL mass, and derive a Mach number, $\mathcal{M}^E = 6.2^{+1.9}_{-1.8}$, from the ratio between the eastern hot and pre-merger temperatures. The resulting collision velocity is $v^E = 3940^{+386}_{-457} \, \mathrm{km \, s^{-1}}$ with the sound velocity of $c_s = 636^{+155}_{-99} \, \mathrm{km \, s^{-1}}$ expected by the WL mass. Thus, the merger time-scale is $0.16^{+0.07}_{-0.05}$ Gyr, assuming a 1D velocity of $v^E/\sqrt{3}$. The difference between spectroscopic redshifts (Guglielmo et al. 2018) of two luminous galaxy associated with the western and eastern structure gives a relative velocity of $\delta v_{\mathrm{l.o.s}} \sim 1700 \, \mathrm{km \, s^{-1}}$. If the subhalo is not moving along the Dec. direction, the time-scale is ~0.1 Gyr with $((v^E)^2 - \delta v_{\mathrm{l.o.s}}^2)^{1/2} \sim 3500 \, \mathrm{km \, s^{-1}}$. Even when we use another mass–temperature scaling relation (Umetsu et al. 2020), the estimated time-scale does not significantly change. The estimated collision velocity is acceptable in cosmological simulations (Bouillot et al. 2015) and observations (Okabe et al. 2019), but is at high end of the PDF of collision velocities for the optically defined merging clusters and similar to those of merging clusters with diffuse radio emission.

4.2.3 Comparison with numerical simulations

In order to visually interpret merger phenomena, we made simulated MUSTANG-2 and *XMM–Newton* images using the numerical simulations of ZuHone (2011) that are made publicly available through ZuHone et al. (2018). ZuHone (2011) computed *N*-body/hydrodynamic simulations of binary mergers with mass ratios of 1:1, 1:3, and 1:10 with impact parameters of 0, 500, and 1000 kpc, respectively. The main cluster mass is $6 \times 10^{14} \mathrm{M_\odot}$, which is slightly higher than those of our samples. We set simulated clusters at the observed redshifts of the merging cluster and then pick out a simulated cluster so that their peak separations between y and S_X maps measured from 90 deg from the merger plane are similar to our observations. The dynamical time and mass ratio are close to our cases. The simulated images, convolved with the PSFs and the transfer function, are shown in Fig. 11. The X-ray merger positions are rotated to be along the *x*-axis. Fig. 11 shows the $\tilde{y}$ and $\tilde{S}_X$ maps of an equal-mass merger with zero impact parameter. The simulated images of the *y* parameter clearly show a double-peaked structure. Bow-shock fronts (red lines) are located at outer-edges of the two hot components. These bow shocks appear as weak changes in the *y* map. We find that it is difficult to constrain the Mach number from the *y* distribution. The *y* peak regions are heated by input cluster merger shocks ($\mathcal{M} \sim 4.7$). The X-ray peak of the simulated image is in-between the double peak *y* structure and its morphology is highly elongated and perpendicular to the merger axis. This feature is slightly different from the best-fitting results and the observed features in that the X-ray peak is closer to the eastern component

and the X-ray morphology is not elongated perpendicular to the axis between the two hot components. The difference could be caused by differences in mass ratio, viewing angle or both. The weak-lensing analysis indicates that the western component is the main cluster, and thus the X-ray peak could be shifted to the east because the X-ray core is moving from the west to the east. For the visual purpose, we plot the simulated images of the merger with the mass ratio of 3:1 in the bottom panel of Fig. 11, in the similar way as the top panels. The *y* peak is associated with the main cluster and the stripping X-ray core is elongated along the merger axis, which is similar to the observed feature. Since the current data cannot constrain the line-of-sight structure of the merger, there remains the uncertainty in the viewing angle. Although it is difficult to find a perfectly matched simulation, the visual comparison helps us understand the plausible configuration that created the observed double-peak *y*, the single X-ray peak, and the mass distribution. Future theoretical studies using the observational parameters would be better for understanding the details.

In the simulation of the equal-mass merger, the temperature in these regions reaches ~25 keV from the initial value ~5 keV, supporting the presence of the hot component in the major merger. As for the mass ratio of 3:1 case, the temperature of the main cluster becomes ~18 keV from ~5 keV and the temperature around the observed *y* peak of the subcluster increases from ~2.5 to ~15 keV. We note that a prominent shock with ~20 keV appears around the negative *y* value at the east region from the subcluster. The asymmetric temperature distribution is similar to the joint analysis results. A quantitative discussion of the 2D comparison is very difficult because the observation cannot constrain the line-of-sight information and the public library of the stimulated images does not cover all the orientation angle. Therefore, the quantitative discussion of the merger boost in Section 4.6 uses the integrated quantities through mass observable scaling relations.

We stress that the joint SZE and X-ray analysis using high-angular resolution data provides a powerful means to extract the multiple gas structures and uncover hot components with $k_B T \sim 20-30$ keV. Such spatially resolved high temperature measurements are difficult with current X-ray satellites. Future *Chandra* observations will test our interpretation by detecting the X-ray surface brightness jumps as shown in red curves in the upper panel of Fig. 11, and will independently estimate the Mach number.

4.2.4 Absence of diffuse radio emission

The major-merger candidates defined by Okabe et al. (2019) evenly cover a new parameter region of mass, mass ratio, and dynamical stages. One main difference from the well-known mergers with diffuse synchrotron radio emissions, the so-called radio haloes and relics, is that the PDF of the merger velocity of the optically defined mergers is shifted to lower speeds. Okabe et al. (2019) found no diffuse radio emission in ~190 merging clusters by both visual inspection and spectral index maps using the NVSS (1.4 GHz; Condon et al. 1998) and TGSS (147.5 MHz; Intema et al. 2017) archival data because it is very difficult to discriminate between radio lobes and haloes/relics. Combined with a presence of hot regions revealed by the joint SZE and X-ray analysis, it is a good opportunity to search again for radio haloes/relics in the major-merging cluster.

We here use the FIRST (1.4GHz; Helfand et al. 2015) data and the GMRT data of the XXL Survey (610MHz; Smolčić et al. 2018). The beam sizes for the FIRST and GMRT data are 5 arcsec and 6.5 arcsec, respectively. In the FIRST image, we find a point source (FIRST J023334.1-053008) associated with the BCG at
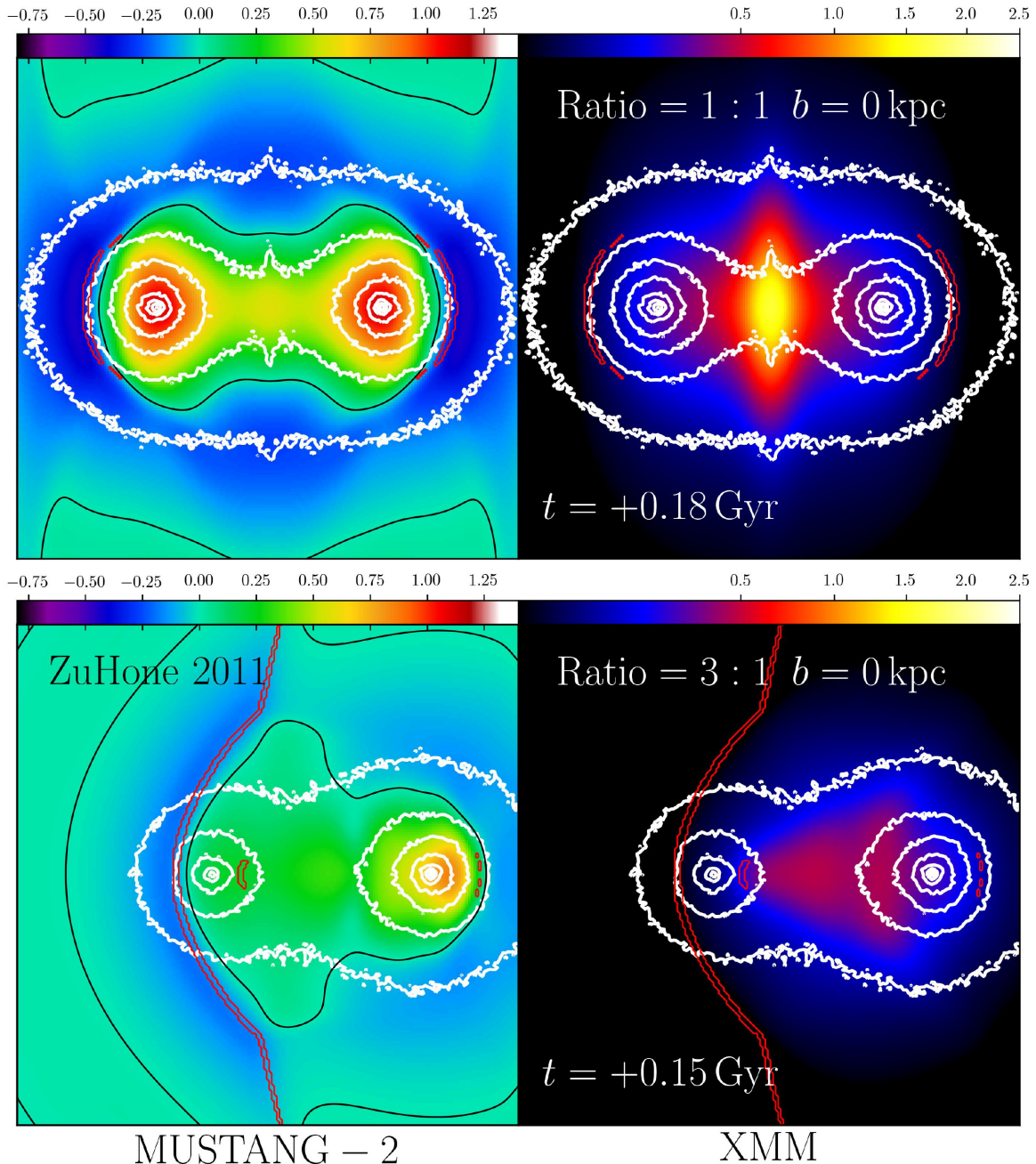
Figure 11. Simulated MUSTANG-2 (left) and *XMM–Newton* (right) images (4 arcmin × 4 arcmin) using numerical simulations of ZuHone (2011) publicly available through ZuHone et al. (2018), taking into account the PSFs and the transfer function. The top panels are the edge-on view of a binary merger with equal-mass ratio and impact parameter $b = 0$ kpc at 0.18 Gyr after first core-passage, which is similar to the case of the major merger, HSC J023336-053022. The white contours denote projected mass density. The black contours in the left panels denote the lines for $\bar{y} = 0$. The red lines are shock features appearing in the projected sky. The bottom panels show the edge-on view with a mass ratio of 3:1 for visual comparison to the X-ray morphology.

spectroscopic redshift $z = 0.4319$ in the western component of the cluster (Fig. 12). The SZE flux around the radio source is suppressed by compact radio source contamination. The radio contamination depends on the spectral index at high frequency (e.g. Lin et al. 2009; Gralla et al. 2014). We note that the radio source region is excluded in the modelling fitting. At 610 MHz (Smolčić et al. 2018) there are three sources (XXL-GMRT J023339.6-053028, XXL-GMRT J023334.1-053008, and XXL-GMRT J023332.1-053008). One of them coincides with the source listed in the FIRST catalogue; the three radio sources are associated with cluster members (the right-

hand panel of Fig. 12). The radio AGN activity might be recently triggered by the cluster merger (∼0.15 Gyr) because the typical timescale of AGN activities is short 0.01–0.1 Gyr (Soker 2016).

We do not find evidence of diffuse radio sources, though the SZE and X-ray data exhibit the presence of hot gas components triggered by the violent merger. This conflicts with the other cases of CIZA J2242.8+5301 (van Weeren et al. 2010) hosting a prominent filamentary radio relic, Abell 2146 (Hlavacek-Larrondo et al. 2018) with double relics, and the Bullet cluster (Markevitch et al. 2002) with a radio halo. The estimated merger time-scale is comparable
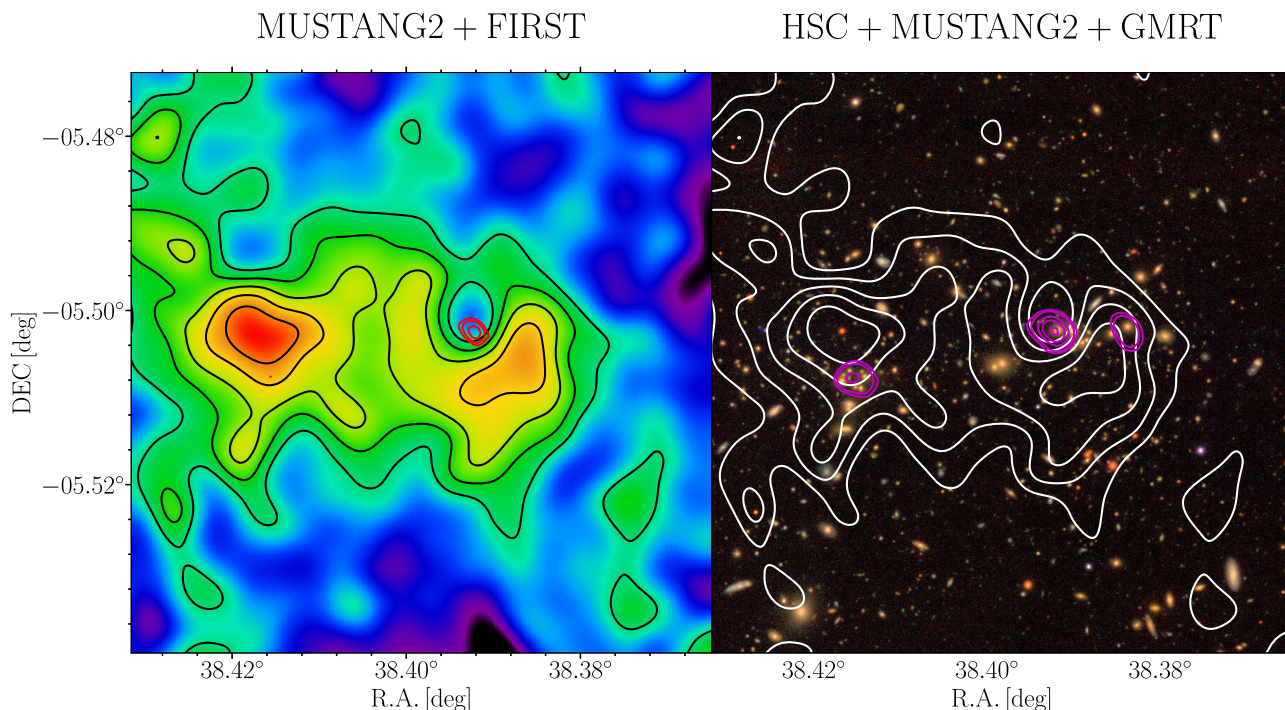
MUSTANG2 + FIRST HSC + MUSTANG2 + GMRT

Figure 12. *Left:* the *y* map for HSC J023336−053022 overlaid with the FIRST (red) contours (1.4 GHz). The contour levels are 4, 8, 16, and $32 \times \sigma_{\mathrm{rms}}$, where $\sigma_{\mathrm{rms}}^{\mathrm{FIRST}} = 1.5 \times 10^{-4}$ Jy beam^{-1}. *Right:* HSC-SSP optical *riz*-colour image overlaid with the *y* map contours (Fig. 1) and the GMRT contours (magenta). The contour levels are 4, 8, 32, 64, 128, and $512 \times \sigma_{\mathrm{rms}}$, where $\sigma_{\mathrm{rms}}^{\mathrm{GMRT}} = 6 \times 10^{-5}$ Jy beam^{-1}. The three low-frequency radio sources are associated with member galaxies. The black contours in the left-hand panel and the white contours in the right-hand panel show the distribution of the Compton *y* parameter (same levels as in Fig. 1, left-hand panel, second row).

to ∼0.1–0.2 Gyr for the Bullet cluster (Markevitch et al. 2002), and 0.2–0.3 Gyr for CIZA J2242.8+5301 and Abell 2146. One of differences is cluster mass. CIZA J2242.8+5301 (Okabe et al. 2015), Abell 2146 (King et al. 2016), and the Bullet cluster (Bradač et al. 2006) are all very massive ($M_{200} \sim 10^{15} h_{70}^{-1} \mathrm{M}_\odot$), while the mass of this cluster is only one-tenth of that ($M_{200} \sim 10^{14} h_{70}^{-1} \mathrm{M}_\odot$). Thus, the release of gravitational energy differs by more than one order of magnitude. Cassano et al. (2013) have shown that the *k*-corrected radio power at 1.4 GHz for diffuse radio emissions have a strong mass dependence; $P_{1.4\mathrm{GHz}} \propto M_{500}^p$ with $p = 3.77 \pm 0.57$. The upper limit of $P_{\mathrm{FIRST}} \sim 3 \times 10^{23}$ W Hz^{-1} with 3σ level is higher than 0.5×10^{23} W Hz^{-1} expected by the relation of Cassano et al. (2013) using the WL mass, and thus we do not rule out a possibility to detect diffuse radio emission by future observations with 1.4 GHz. Assuming the spectral index $\alpha = 1.3$ (Cassano et al. 2013), the expected radio powers at the GMRT and TGSS frequencies are $\sim 2 \times 10^{23}$ and $\sim 10^{24}$ W Hz^{-1}, respectively. The *k*-corrected powers of the 3σ rms noise levels of the GMRT and TGSS observations are $\sim 10^{23}$ and $\sim 4 \times 10^{24}$ W Hz^{-1}, respectively. Therefore, expected diffuse radio sources (Cassano et al. 2013) are not detected by the GMRT observation (Smolčić et al. 2018).

Thanks to the multicomponent gas analysis and high-angular resolution synchrotron radio data, we can constrain the upper limit of the particle acceleration efficiency η_e via the first-order *Fermi* acceleration. We assume that a merger shock created the hot gas component and simultaneously injected cosmic ray electrons. An injection spectra at downstream of the shock is defined by $Q_e = Q_{e,0}\gamma^{-p}$, where *p* is the particle index, γ is the Lorentz factor, and $Q_{e,0}$ is the injection normalization. Assuming a diffusive shock acceleration (DSA; Drury 1983), the particle index is given by $p = 2(\mathcal{M}^2 + 1)/(\mathcal{M}^2 - 1)$. Cluster merger shocks convert kinetic

energy to thermal energy. The total thermal energy of electrons heated by the merger shock can be computed from the pressure of the hot gas component measured by the multicomponent analysis, $E_{\mathrm{th},e} = \int (3/2)P_e \mathrm{d}V$. When we constrain the upper limit of the acceleration efficiency, we assume that all the kinetic energy is converted to the thermal energy. The injection energy is described by $\int_{\gamma_{\min}} Q_{e,0}\gamma^{-p}E\mathrm{d}\gamma = \eta_e E_{\mathrm{th},e}/\Delta t$ using a constant efficiency factor η_e, where Δt is the merger time-scale and *E* is the energy per cosmic ray electron. We assume $\gamma_{\min} = 2$. Given the injection spectra and the inverse-Compton and synchrotron energy losses, the steady state spectra has a form of $N(\gamma) \propto \gamma^{-(p+1)}$ (Sarazin 1999). Then, the synchrotron emissivity is $\mathrm{d}L_{\mathrm{syn}}/\mathrm{d}\nu \propto B^{(p+2)/2}\nu^{-p/2}$, where *B* is the magnetic field strength and ν is a frequency. A cooling time scale for cosmic ray electrons emitting at the GMRT frequency is 0.04 Gyr assuming a typical magnetic field $B = 1\,\mu G$ and shorter than the merger time scale ~ 0.15 Gyr. We assume Mach number $\mathcal{M} = 6.2$ and $\Delta t = 0.16$ Gyr (Section 4.2.2). Even when we change by $\mathcal{M} = \pm 2$ or $\Delta t = \pm 0.05$, the results do not significantly change. We consider the cylindrical volume of the eastern hot component within the central 1 arcmin. The left panel of Fig. 13 shows a comparison of the 1σ upper limits of the radio observations and the synchrotron flux density expected by 0.3,1 and 3 per cent acceleration efficiency at $B = 1\,\mu G$. The upper limits of the radio observations are estimated by the 3σ level. The acceleration efficiency should be less than $\mathcal{O}(10^{-2})$, which is lower than typical values used in theoretical models of galaxy clusters (e.g. Kang & Ryu 2013; Vazza et al. 2016) and strong shocks in supernova remnants (e.g. Miniati et al. 2001). The right panel of Fig. 13 shows the upper limit on η_e as a function of *B*. Since magnetic strengths of order of $\mathcal{O}(1)\,\mu G$ (e.g. Vogt & Enßlin 2003) or higher in radio relics (Nakazawa et al. 2009; van Weeren et al. 2011), the acceleration efficiency is less
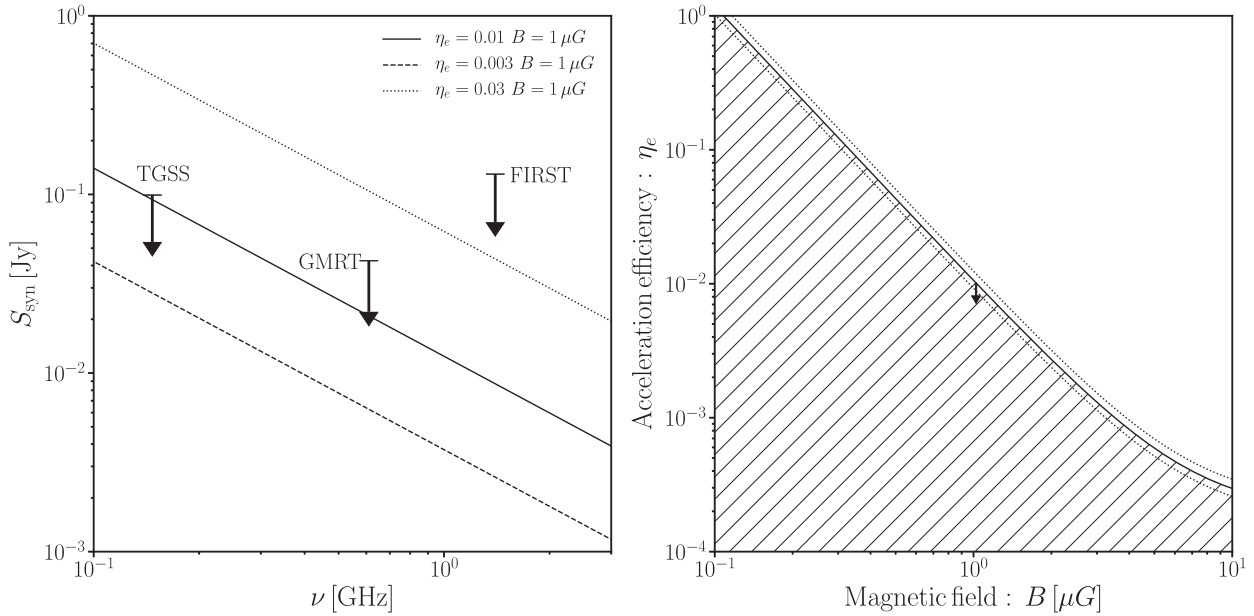
Figure 13. *Left*: synchrotron radio flux density. Radio upper limits are given by $3\sigma_{\rm rms}$ levels. The solid, dashed, and dotted lines are the radio flux density expected by the multi-component joint SZE and X-ray analysis with different acceleration efficiency, η_e. *Right*: the upper limits of the acceleration efficiency as a function of magnetic strength. The dotted lines denote the errors computed from the uncertainty of P_e. Non-detection of diffuse radio emission in the hot gas component gives the low acceleration efficiency of $<10^{-2}$ at $B > 1\,\mu G$.

than sub per cent and thus is very inefficient. Similar results are recently reported in well-known radio-relic clusters (Botteon et al. 2020).

Another possibility for particle acceleration is re-acceleration of supra-thermal electrons which are possibly ejected from radio AGN sources. If the AGNs were not triggered before merger shocks was sweeping, the scenario would not conflict with non-detection of diffuse radio sources, given their short time cycles of 0.01–0.1 Gyr (Soker 2016).

4.3 HSC J021056-061154

4.3.1 Joint analysis

HSC J021056-061154 exhibits a complex distribution of member galaxies, comprising a central component elongated along the west-east direction and southern substructures (the bottom-right panel of Fig. 1). The central X-ray surface distribution is elongated along the east-west direction, similar to the central galaxy distribution. The X-ray peak position coincides with the BCG. The X-ray flux is much lower than that of the other clusters. The bottom-left panel of Fig. 1 shows an anisotropic distribution of the Compton y parameter. The eastern and western regions show negative and positive y values, respectively. The high y region is elongated along the direction perpendicular to the major axis of the X-ray core. Taking into account the angular transfer function, this feature indicates that the peak position of the y parameter, that is, the hot region, is offset 45 arcsec to the west of the BCG.

Fig. 14 shows the y and S_X radial profiles. The signal-to-noise ratio of the y profile is much lower than those of the other clusters. Since it is difficult to constrain the outer-slope, we adopt a Gaussian prior $\beta_T = 0.67 \pm 0.30$ for the modelling. The temperature is an increasing function out to $\sim$500 kpc. When we refit with a model with constant temperature, the model is disfavoured to describe

the $\tilde{y}$ profile. The measurement uncertainty of the temperature is larger than that of the electron number density because of the low signal-to-noise ratio of the y profile.

We next perform the 2D analysis in a similar way to Section 4.2. Since the signal-to-noise ratio is low, we use the binned images with pixel size of 20 arcsec. In the modelling, we consider the eastern and western components to describe the main cluster and the offset hot component, respectively. We adopt the spherically symmetric gNFW model for the eastern main component and the spherically symmetric β model for the western hot component. We fixed $\beta_n^W = \beta_T^W = 1$ to describe the localized hot component in a similar way to Section 4.2. As shown in the lower-middle panel of Fig. 15, the main cluster has a cool core in which the X-ray-like emission-weighted temperature changes from $\sim$3 keV to $\sim$6 keV as the radius increases. The X-ray-like emission-weighted temperature for the main component within 300 kpc from the XXL centre is $\sim$5 keV. The features of the main component are not significantly different from the results of the 1D analysis. The western temperature reaches $\sim$11 keV. The best-fitting centres are shown in Table 5. The superposed temperature map (the lower-left panel of Fig. 15) exhibits an anisotropic distribution. A small gas fraction of the western region has a high temperature, while the eastern region is not affected by the high temperature component. The feature indicates that the cluster is likely to be a binary cluster prior to merger. The superposed X-ray surface brightness distribution is elongated along the east-west direction.

Since the cluster is located at the edge of the HSC-SSP survey field, the shape catalogue does not fully cover the entire region of the cluster because of the full-colour and full-depth requirement (Section 3.4). Therefore, the measurement uncertainty of the WL mass is very large (the right panel of Fig. 4 and Table 4). We cannot carry out a multi-component WL analysis because of this limitation. A comparison of weak-lensing and HE-derived masses is discussed in Section 4.8.
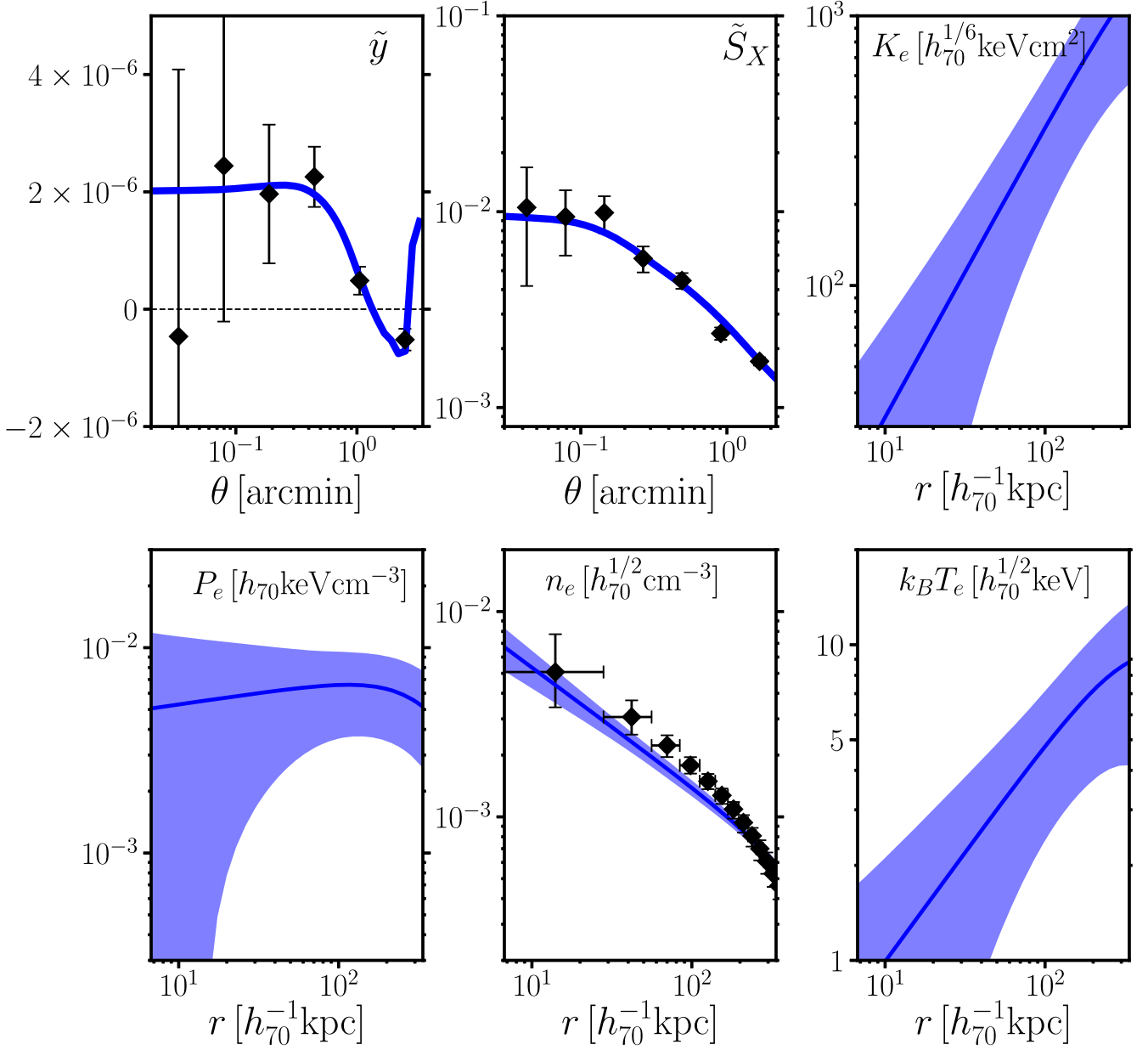
Figure 14. The same figure as Fig. 3, but for HSC J021056-061154. The signal-to-noise ratios of the y and S_X profiles are $\sim 5\sigma$ and $\sim 16\sigma$, respectively. The increase in the $\tilde{y}_m$ profile at large radii is caused by the transfer function.

4.3.2 Pre-minor merger physics

The y map of this cluster (Fig. 1) is chaotic in structure, with a peak offset to the west of X-ray peak. In particular, the major axis of the y map is elongated perpendicular to that of the X-ray core. We adopt an elliptical model to describe the gas structure.

The ellipticity of the projected distribution of the electron number density and temperature is defined by $e = 1 - b/a$, where a and b are the major and minor axes of gas properties following Oguri et al. (2010). We introduce an orientation angle of the major axis, ϕ_e, measured from the north to the east. The distance of an iso-contour from the centre is given by

$$r = (x'^2/(1 - e) + (1 - e)y'^2)^{1/2},$$
$$x' = x\cos\phi_e + y\sin\phi_e,$$
$$y' = -x\sin\phi_e + y\cos\phi_e,$$
(20)

where x' and y' are the rotated coordinates. The best-fitting orientation angles of the eastern and western components are $\phi_e^E = 112^{+7}_{-8}$ deg and $\phi_e^W = 17^{+9}_{-10}$ deg, respectively. The elongation of the hot gas in the projected sky is almost perpendicular to that of the cold gas. This suggests that the hot region has been heated by a merger shock triggered by the infalling dense gas. The ellipticities are $e^E = 0.53^{+0.10}_{-0.13}$ and $e^W = 0.29^{+0.16}_{-0.18}$. The best-fitting model map is shown in Fig. 16. Since the eastern region is not yet heated, the cluster is interpreted to be in a pre-merger phase.

We did not consider the elongation along the line of sight. Another possibility is that an ellipticity of the temperature distribution differs from that of the density distribution. If the temperature distribution were more elongated on the sky plane than the gas distribution, the y parameter would be lower than expectations from the spherical model. A full 3D reconstruction of gas properties is left for future studies to address the geometrical assumption.
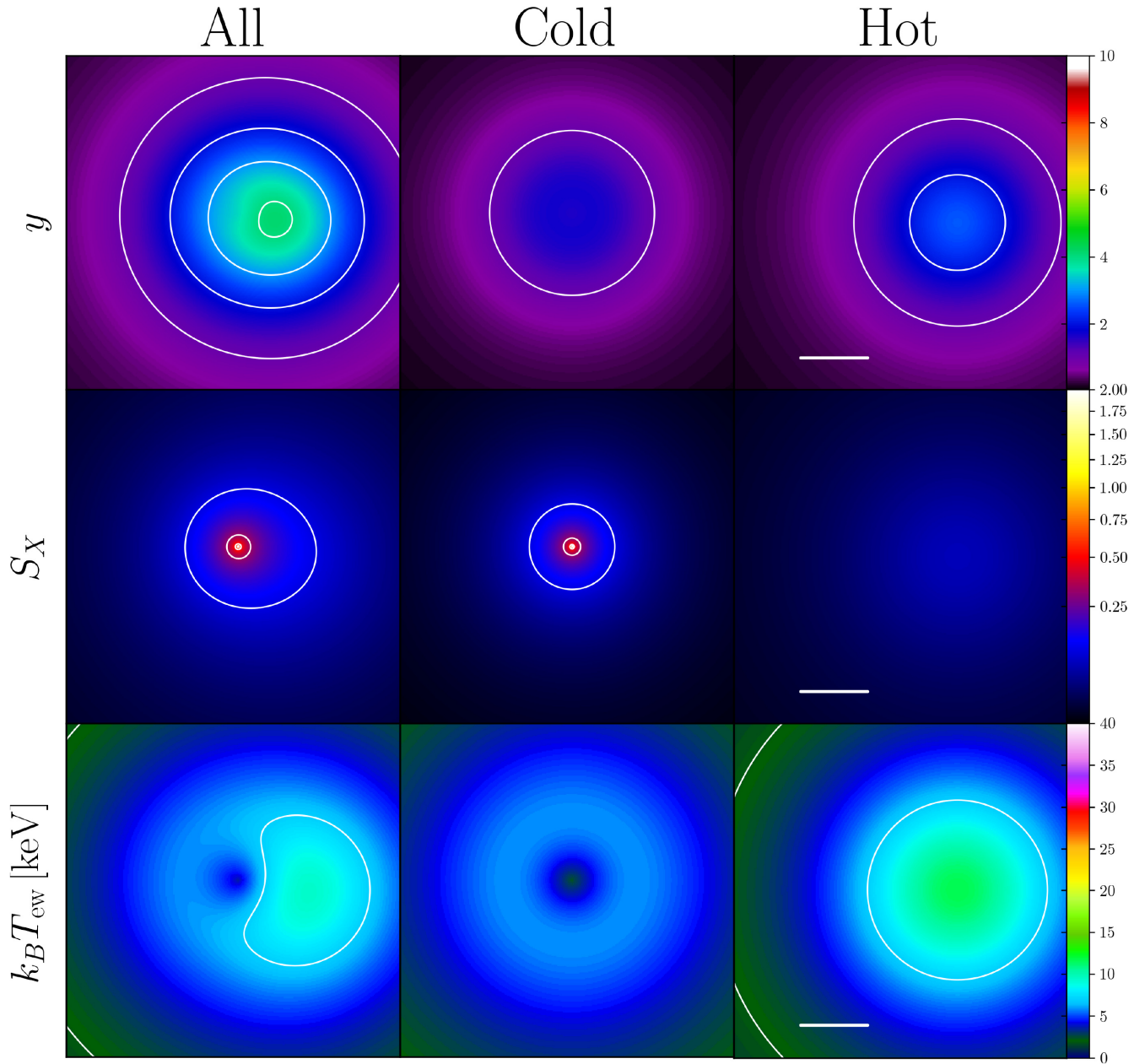
Figure 15. Model maps for HSC J021056-061154. Colours, contours and lines are the same as those in Fig. 10.

A group of several member galaxies in the west end of the central overdensity region is associated with the western hot region. The stellar mass of this group, $M_*^{\rm W} = 3 \times 10^{11} M_\odot$, is lower than the total stellar mass of $M_* = 4 \times 10^{12} M_\odot$ found using the S16A catalogue. When we use the S18A catalogue, our estimates become $M_*^{\rm W} = 7 \times 10^{11} M_\odot$ and $M_* = 4 \times 10^{12} M_\odot$. Therefore, the substructure mass triggering the hot region is one-tenth or less of the mass of the main cluster. The configuration and mass suggest that this system is likely to be a minor merger before core passage. Assuming a collision velocity of $1000\,{\rm km\,s^{-1}}$ (Okabe et al. 2019), the spatial separation of the two galaxy concentrations implies that the cluster is $\sim 0.3\,{\rm Gyr}(\sec\theta/1)$ before core passage. Here, θ is an inclination angle between the merger axis and the sky plane. The ratio between the projected temperatures of the hot and cold components gives the Mach number $\mathcal{M} \sim 4$ and the 1D collision velocity

$v/\sqrt{3} \sim 1500\,{\rm km\,s^{-1}}$ and the estimated time-scale, $\sim 0.2\,{\rm Gyr}$, is not significantly changed.

4.3.3 Comparison with numerical simulations

For visual purposes, we compute mock images using numerical simulations of ZuHone (2011) in a similar way of Section 4.2.3. Fig. 17 shows an edge-on view of a simulated merger with a 1: 10 mass ratio and $b = 500\,{\rm kpc}$ at $t = 0.14\,{\rm Gyr}$ before first core-passage. The features such as the double-peaked X-ray surface brightness distribution and the elongated y map associated with the western subcluster are found. The simulated y map after processing with the transfer function, has negative values at $\theta \gtrsim 1$ arcmin. This morphology resembles the observation. The western component is heated by a merger shock (red lines). The simulated y image shows a high value around the
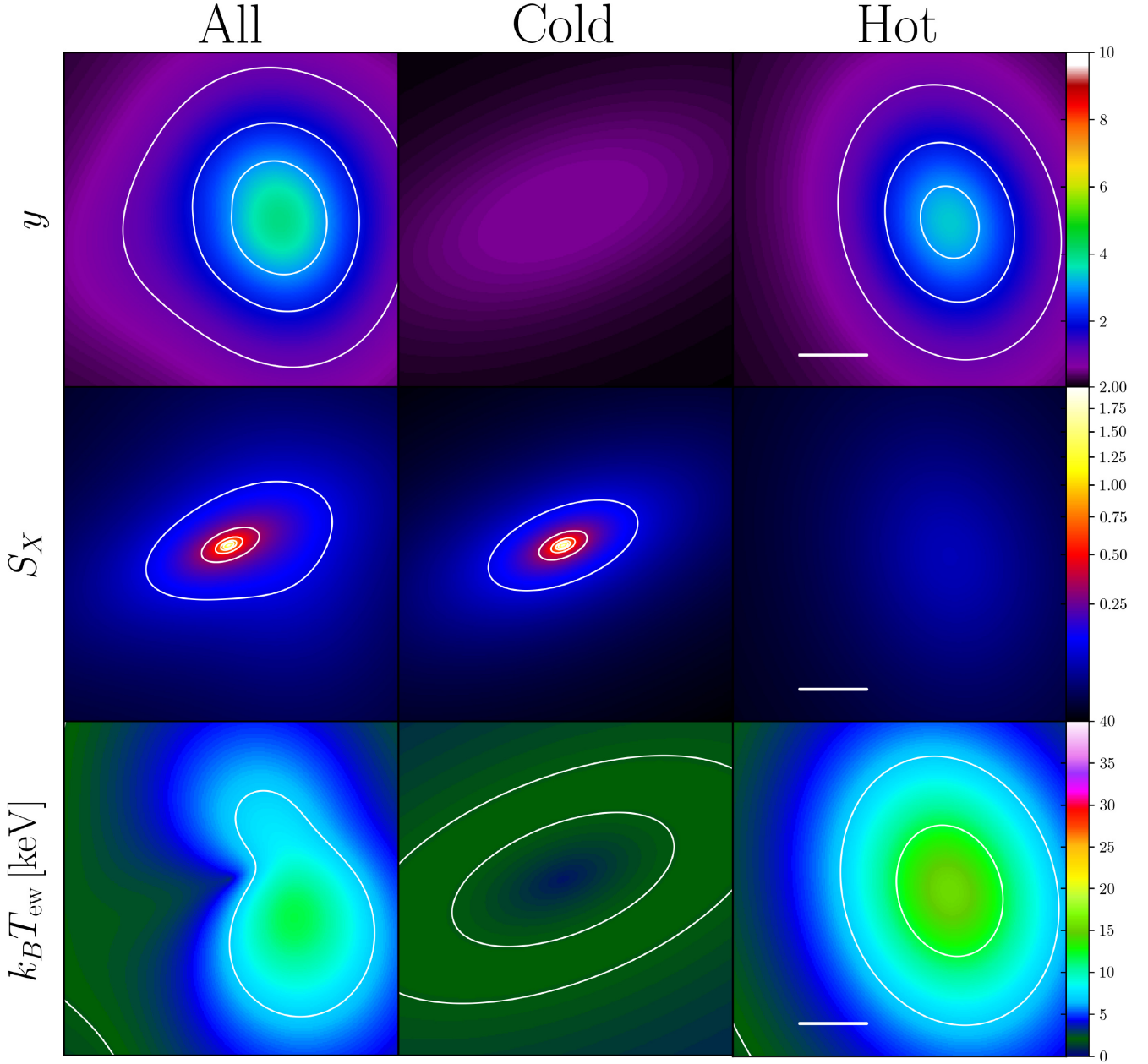
Figure 16. Elliptical model maps for HSC J021056-061154. Colours and contours are the same as those in Fig. 10.

main cluster, while our observation does not detect such a feature, perhaps caused by differences in the assumptions of the cool core between simulations and observations, and/or a different main cluster mass. Although the details of the simulated image are not identical to our image, the characteristic properties of the precursor phase of a minor merger well represents the observation.

4.4 Comparison with SZE and X-ray images in previous observations

We compare the SZE and X-ray imaging for the three clusters with those reported from previous observations. As aforementioned, the high resolution mapping and their multi-wavelength analysis reveal that the gas properties are more or less disturbed regardless of the number of galaxy density peaks. Thus, even minor mergers along

with galaxies or small subhalos which are not significantly detected by the peak-finding method of the major-merger finder (Okabe et al. 2019) trigger perturbations in distributions of gas temperature and density. The observed properties are summarized as follows. The single-peaked cluster shows the sloshing pattern in both the y and S_X distributions (Section 4.1.2). The double-peaked cluster with the mass ratio of $\sim$2: 3 has the single X-ray core between the two y peaks (Section 4.2). The part of the supercluster exhibits the elongated hot region perpendicular to the major axis of the cool gas core (Section 4.3.2). Our multi-wavelength results of SZE, X-ray, WL and optical measurements agree with predictions of the imaging patterns in numerical simulations (ZuHone et al. 2010; ZuHone 2011; ZuHone et al. 2018); the single-peaked cluster, the double-peaked cluster, and the part of the supercluster are likely to be at sloshing, post-major, and pre-minor merging phases, respectively.
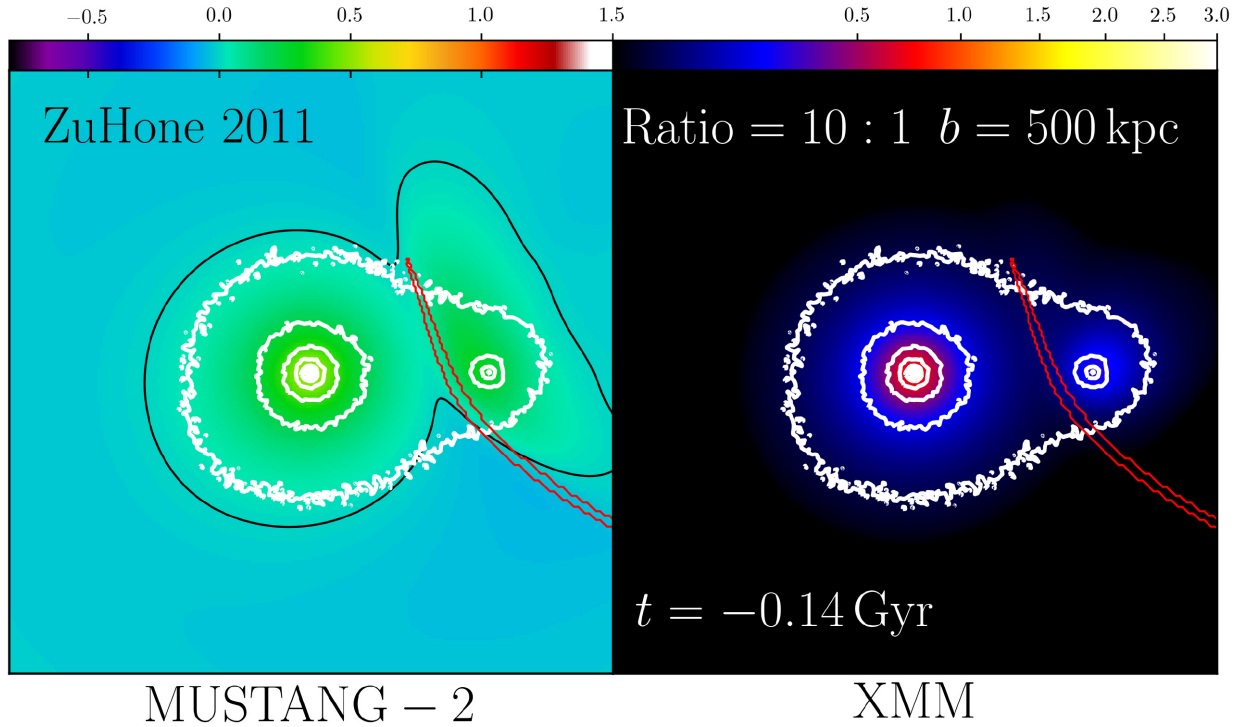
Figure 17. Simulated MUSTANG-2 (left) and *XMM-Newton* (right) images (4 arcmin × 4 arcmin) using numerical simulations of ZuHone (2011) publicly available through ZuHone et al. (2018), taking into account the PSFs and the transfer function. The panels are the edge-on view of the merger with 1: 10 mass ratio and $b = 500$ kpc at 0.14 Gyr before first core-passage, which is a similar case to the minor merger, HSC J021056-061154. Contours are the same as those in Fig. 11.

Sloshing features are found in many clusters through X-ray observations (e.g. Laganá, Andrade-Santos & Lima Neto 2010). Atacama Large Millimetre/submillimetre Array (ALMA) observation with 5 arcsec resolution found in RX J1347.5-1145 that y and S_X maps have a single peak, but there is a significant offset between the two peaks (Kitayama et al. 2016). The MUSTANG observation (Mason et al. 2010; Korngut et al. 2011) shows a reduced y parameter around the X-ray peak due to strong contamination from the central, radio-loud AGN. A significant residual y is found in RX J1347.5-1145 when fitting and subtracting a profile with the SZ centroid fixed to be the same position as the X-ray centroid (Plagge et al. 2013; Ueda et al. 2018; Di Mascolo, Churazov & Mroczkowski 2019a). However, Di Mascolo et al. (2019a) found no significant residuals, on scales from 5 arcsec to 10 arcmin, when jointly fitting an ellipsoidal pressure profile model with a floating centroid fit to the ALMA, ACA, Bolocam, and *Planck* data.

Kitayama et al. (2004) have measured the temperature of a subcluster in a merging cluster, RX J1347.5-1145 combining the SZE data from Submillimetre Common User Bolometer Array (SCUBA) and Nobeyama Bolometer Array (NOBA) and *Chandra* X-ray data and found a hot component with ∼20 keV, for the first time. Their finding of the hot temperature in the merging cluster is similar to those in HSC J023336-053022.

The *Chandra* Observation of the Bullet cluster (Markevitch et al. 2002) shows a bow-shock ahead of a stripping cool core and X-ray emission from a main cluster of which the core is elongated along the direction perpendicular to the merger axis. Halverson et al. (2009) detected a SZE signal associated with the main cluster using APEX-SZ with 1 arcmin resolution. Di Mascolo et al. (2019b) estimate a Mach number $\mathcal{M} = 2.08 \pm 0.12$ of the bow-shock with ALMA and Atacama Compact (Morita) Array (ACA) assuming an instantaneous equilibration of the electron and ion temperatures. However, no

high-resolution SZE observation covers the entire shock region to date.

The Arcminute Microkelvin Imager (AMI; Rumsey et al. 2017) discovered in CIZA J2242.8+5301 an equatorial-shock-heated gas with elongation is perpendicular to both its merger axis and the major axis of the cool core. The relationship of the morphology of y and S_X maps is the same as found in the pre-minor merger, HSC J021056-061154.

Menanteau et al. (2012) found that X-ray and y distribution in the El Gordo cluster is offset similar to the case of RX J1347.5-1145. An ALMA observation relying on X-ray data for priors (Basu et al. 2016) constrained the Mach number $\mathcal{M} = 2.4^{+1.3}_{-0.6}$ at the edge of X-ray surface brightness associated with radio relic (Botteon et al. 2016).

Both stacked *Planck* SZE and *RASS* X-ray maps for low-redshift and massive merging clusters (Okabe et al. 2019) found that the y and S_X distributions at cluster outskirts are elongated along the direction perpendicular to the merger axis, though the X-ray main core is elongated along the merger axis.

An offset between X-ray and Compton y parameter distributions seems common in merging clusters including literature and our sample. A perpendicular orientation angle between the major axes of high y and X-ray core distributions is also found in some clusters. However, the double-peaked y distribution has not yet been reported by observational studies.

4.5 Temperature Comparison

We compare the temperatures derived from the joint SZE and X-ray analyses with X-ray temperatures from spectroscopic measurements (Giles et al. 2016; Lieu et al. 2016; Adami et al. 2018). The XXL survey measured the X-ray temperature within $300h_{70}^{-1}$ kpc from their
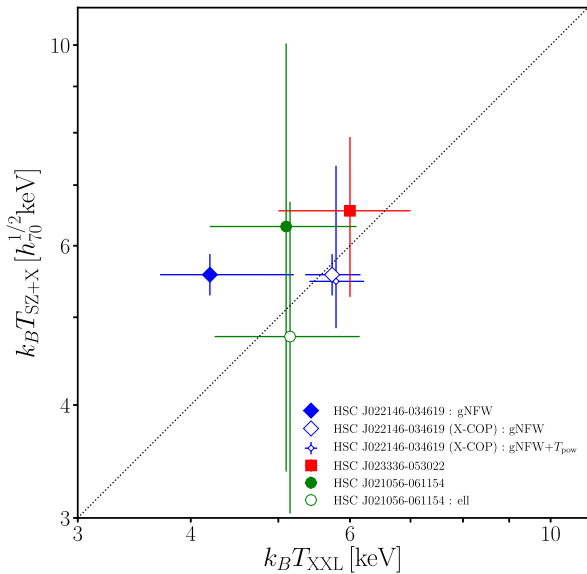
Figure 18. Comparison of X-ray and SZE temperatures. Blue diamond, red square, and green circle are HSC J022146-034619, HSC J023336-053022 and HSC J021056-061154, respectively. The open blue diamonds for HSC J022146-034619 denote the X-COP temperature measurement using deep on-source data. The small open diamond is the SZE temperature based on the gNFW+T_{pow} model. The X-ray temperatures of the elliptical model for HSC J021056-061154 (open green circle) and the gNFW+T_{pow} model for HSC J022146-034619 (small open diamond) are shifted by 1.01 for display purposes.

X-ray centres. We also use X-ray temperature derived from the deep on-target observation for HSC J022146-034619 from the X-COP measurement (Section 4.1).

We compute the cylindrical emission-weighted temperatures from our best fits within $300h_{70}^{-1}$ kpc from the XXL centres. Since HSC J023336-053022 and HSC J021056-061154 have complicated *y* distributions, we use the results of 2D analyses. Fig. 18 shows a temperature comparison between the joint SZE and X-ray analysis, $k_B T_{SZ+X}$, and the X-ray spectroscopic measurement, $k_B T_{XXL}$. We find in HSC J022146-034619 that the temperature using the XXL survey data and that from X-COP using the deep pointing observation differ by ∼2 keV, which is a 2.3σ difference; our result agrees with the latter one. The temperature of the gNFW+T_{pow} model for HSC J022146-034619 does not significantly change from that of the gNFW model. For the three clusters, the central projected temperatures derived the joint SZE and X-ray analyses agree well with the X-ray temperatures.

Mroczkowski et al. (2009) have found using Sunyaev-Zel'dovich Array (SZA) data that 1D, radial temperature profiles determined from joint SZE and X-ray analysis are in reasonably good agreement with those obtained from an independent X-ray spectroscopic analysis. Romero et al. (2017) have compared SZE temperatures with X-ray temperatures for 14 clusters and found a good agreement $\langle T_{SZ+X}/T_X \rangle = 1.06 \pm 0.23$ in gas mass-weighted temperatures. Although the previous studies did not carry out a multiple component analysis as demonstrated in this paper, our results agree with their results.

4.6 Deviations from scaling relations

In this section we study whether the dynamical states of the three clusters affect their positions relative to the scaling relations between total mass and temperature ($k_B T_{SZ+X}$), between total mass and the
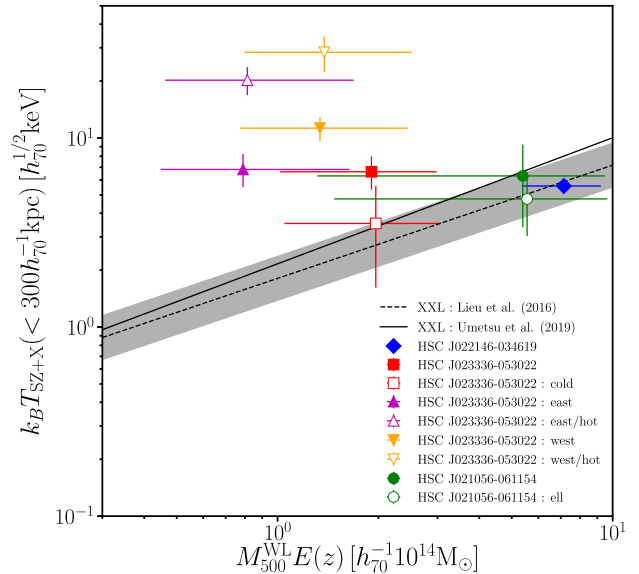

Figure 19. Mass–temperature scaling relation at $\Delta = 500$. The emission-weighted temperatures are computed within $300h_{70}^{-1}$ kpc from cluster centres. The solid and dashed lines denote the best-fitting scaling relations for the XXL clusters of Umetsu et al. (2020) and Lieu et al. (2016), respectively. The grey region is a combination of the 1σ uncertainty of the normalization and intrinsic scatter. Blue diamond, red square, magenta up-triangle, orange down-triangle, and green circle are HSC J022146-034619, the total, eastern and western component for HSC J023336-053022 and HSC J021056-061154, respectively. The open symbols denote the hot and cold components for the major merger or the elliptical model for the minor merger, respectively. The masses of open symbols are shifted by a factor of 1.03 for display purposes. The temperatures of the major merger, HSC J023336-053022, are much higher than those of the scaling relation.

integrated Compton parameter (Y_{cyl}) and between the total and gas mass (M_{gas}). We compute gas quantities from the best-fitting temperature and density profiles to avoid the PSF smearing effect and the radio transfer function. We use the results of multi-component analyses for HSC J023336-053022 and HSC J021056-061154.

4.6.1 M−T relation

We first compute emission-weighted temperature, $k_B T_{SZ+X}$, within projected radius $R = 300h_{70}^{-1}$ kpc from cluster centres following the XXL papers (Lieu et al. 2016). The emission-weighted temperature is computed by the best-fitting parameters of the joint SZE and X-ray analysis; the X-ray emission weight and the uncertainty are calculated from the error covariance matrix. The dashed line in Fig. 19 represents the mass–temperature scaling relations compiled from the XXL (Pierre et al. 2016), COSMOS (Kettula et al. 2013) and CCCP (Hoekstra et al. 2015) surveys. Umetsu et al. (2020) have carried out a weak-lensing analysis of XXL clusters using the HSC-SSP 16A shape catalogue and found a slightly lower mass scale than that of Lieu et al. (2016) (the solid line), though they are consistent within ∼1σ errors. The temperature of the single-peaked cluster, HSC J022146-034619, agrees with Lieu et al. (2016). We cannot find significant deviations for the minor merger, HSC J021056-061154, from the best-fitting scaling relations, regardless of the models. The temperature for the major merger, HSC J023336-053022, is two or three times higher than implied by the two scaling relations. The significance level of the deviation compared to scatter, $[k_B T - f_T(M)]/\sigma_T$, is $4.7^{+5.8}_{-3.0}$, where $f_T(M)$ is the best-fitting scaling relation

(Lieu et al. 2016) with $M = M_{500}^{WL} E(z)$ and σ_T is a combination of the normalization uncertainty and intrinsic scatter of the scaling relation. We consider both the WL mass and temperature uncertainties in the error calculation. The temperature of the central cool component still follows the scaling relations. The temperatures of the eastern and western hot components are at $37.5^{+25.9}_{-18.8}$ and $38.5^{+28.5}_{-18.8}\sigma-$levels higher than those expected based on their WL masses, respectively. The main source of the errors is the uncertainties of weak lensing masses. Although the intrinsic scatter extracted from the large sample (Lieu et al. 2016) would statistically include minor and major merger effects, the instant major merger boosts the temperatures from the baseline. In previous studies (e.g. Ricker & Sarazin 2001; Poole et al. 2007), numerical simulations for major mergers with a mass ratio of 1: 3 have shown that the temperature increases by a factor of two just after first pericentre passage. Our result is in good agreement with numerical simulations (see Section 4.6.4).

4.6.2 M−Y_{cyl} relation

We compute the cylindrical Compton parameter, Y_{cyl} (in units of Mpc²), as follows:

$$Y_{cyl} = 2\pi D_A^2 \int_0^{\theta_{500}} y(\theta')\theta' d\theta', \qquad (21)$$

where D_A is the angular-diameter distance from the observer to the cluster in Mpc, and the enclosed radius, $R_{500} = \theta_{500} D_A$, is determined in the WL analysis.[2] We also propagate errors of the WL-determined r_{500} into the integrated Y parameters. The radii, r_{500}, for the western and eastern components in HSC J023336-053022 are computed from the M_{500} derived from the 2D multicomponent WL analysis (Section 4.2). The projected distance between the two peaks in the $\tilde{y}_d$ map is lower than r_{500} (Section 4.2.2). Gupta et al. (2017) found that a conversion factor from a spherical integrated Y parameter to a cylindrical Y parameter is 1.151. We convert from a spherical Y parameter using a numerical simulation (Yu, Nelson & Nagai 2015) to the cylindrical Y parameter that is shown by the solid line in Fig. 20. The normalizations of two numerical simulations (Yu et al. 2015; Gupta et al. 2017) agree well with each other. The Y parameter of the single-peaked cluster, HSC J022146-034619, is half the expected value given its mass. This is caused by the normalization of the electron pressure profile being lower than expected from the *Planck* SZE pressure profile (Planck Collaboration V 2013). The minor merger scenario we proposed agrees with the numerical simulations. Since the model pressure outside the core of the minor merger is higher than those of the other clusters, the integrated Y of this cluster is comparable though its peak signal-to-noise ratio is lower. However, the Y parameters of the major merger are $7.7^{+8.3}_{-2.6}$ times higher than the scaling relation suggests, where we do not use the intrinsic scatter from the numerical simulation (Gupta et al. 2017). Poole et al. (2007) have investigated using numerical simulations the time evolution of the cylindrical Compton Y parameter within R_{2500} and found that it increases by about a factor of 4 just after first pericentre of major merger with a 1:3 mass ratio. Wik et al. (2008) have shown that the simulated spherical Compton Y parameter over the entire region of clusters increases by about 50 per cent times in major mergers with a 1:3 mass ratio.

Figure 20. Scaling relation of the WL mass and cylindrical Y parameter at $\Delta = 500$. The solid and dashed lines denote the best-fitting scaling relations from the numerical simulations of Yu et al. (2015) and Gupta et al. (2017), respectively. Colour symbols and grey region are the same as Fig. 19. The Y parameters of the major merger significantly depart from the scaling relation.

Although the measurement methods are different, the increase in the Y parameter provides similar trends to our results. However, Yu et al. (2015) have shown in cosmological hydrodynamic simulations that the spherical Y parameter of the thermal component has no significant merger boost at 0.15 Gyr after core passage and that the scatter of the Y parameter in the scaling relation is at most about 12 per cent. This is not supported by our data. They also found that the normalization of the Y parameter for the thermal component is $\sim$ 20–30 per cent lower than that obtained when non-thermal pressure is included. Similarly, Krause et al. (2012) have studied merger-induced scatter and bias in the $M-Y$ scaling relation using cosmological hydrodynamic simulations. They found that the Y parameter of major mergers within a Gyr after core-passage is below the baseline of the scaling relation and the Y parameter increases more slowly during mergers than expected from the overall scaling relation. This is not supported by our data, either.

There seems to be a discrepancy in results between cosmological and non-cosmological simulations. The discrepancy would depend on how much the thermal energy or the non-thermal pressure is increased by cluster mergers. In cosmological simulations (Krause et al. 2012; Yu et al. 2015), the level of non-thermal pressure support such as the bulk motion and turbulence is more dominant. Non-cosmological simulations (e.g. Ricker & Sarazin 2001; Poole et al. 2007; Wik et al. 2008) studied gas heating induced by supersonic motions in the major merger regime. The temperature and density enhancements are correlated in the shock region and thereby the Y parameter increases. From optical cluster samples, we in principle can find major mergers in various stages, thanks to the long lifetime of galaxy subhaloes (see details in the introduction of Okabe et al. 2019). A combination of optical surveys and follow-up observations is therefore a powerful approach to understand gas physics in clusters that are outliers in cosmological simulations.

---

[2]We note that arcmin² and steradians are other common units for Y used in the literature, in which case the D_A^2 factor should be omitted from equation (21) and corresponding units of angles or solid angles should be used in the integral.
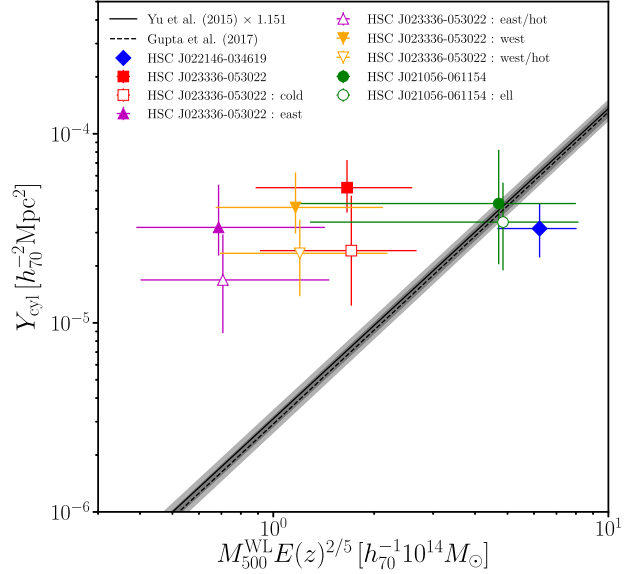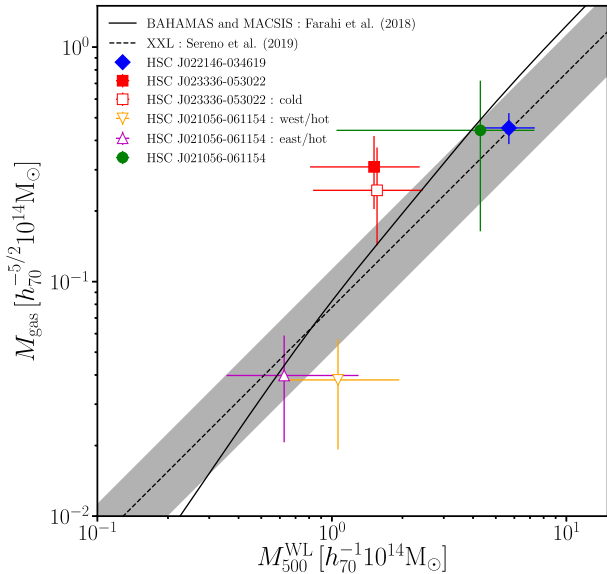
Figure 21. Relation between the WL mass and gas mass within spherical radius, r_{500}. The solid and dashed lines denote the best-fitting scaling relations from numerical simulations (Farahi et al. 2018) and the XXL clusters (Sereno et al. 2020), respectively. Colour symbols and grey region are the same as Fig. 19.

4.6.3 M−M$_{gas}$ relation

We also investigate the relation between total mass, inferred from WL analysis, and gas mass within each cluster's spherical radius r_{500}, as shown in Fig. 21. The cases of the major and minor mergers use the results of the multicomponent analyses. In 3D dimensions, we calculate the off-centring effect of each component, as follows:

$$\rho^{\text{off}}(r) = \frac{1}{2\pi^2} \int_0^\pi d\theta \int_0^{2\pi} d\phi$$

$$\rho\left(\sqrt{d_{\text{off}}^2 + r^2 - 2rd_{\text{off}}\cos\theta\sin\phi}\right), \qquad (22)$$

where ρ is the mass density, d_{off} is the off-centring radius, and r is the distance from the centre in the 3D space. We ignore the separation between components along the line of sight. Since the central component dominates for the gas mass, this assumption does not significantly change the result. We propagate errors of the WL-determined r_{500} into gas mass estimates. We also plot a theoretical scaling relation from cosmological hydrodynamical simulations (Farahi et al. 2018) and the scaling relation (Sereno et al. 2020) derived for the XXL sample (assuming $M_{\text{gas}} \propto M$ and no evolution) based on the HSC-WL (Umetsu et al. 2020) and XXL survey data. We find that the total gas mass within the major merger (red square) and the gas mass for the western hot component of the major merger (orange downward-triangle) are slightly higher and lower than the baseline scaling relations, respectively. If the gas mass follows the scaling relations before the merger, the feature suggests a possibility that a small fraction of the gas mass of the main cluster is moved to the region of the subcluster. Indeed, the X-ray core is composed of the two components (Section 4.1). The surface-brightness weighted centre close to the secondary X-ray peak is at the intermediate position of the two y peaks and the main X-ray peak is close to the eastern component. Some fraction of the X-ray core could be the remnant of the main cluster. A difference between collisional gas and collisionless dark matter distributions is
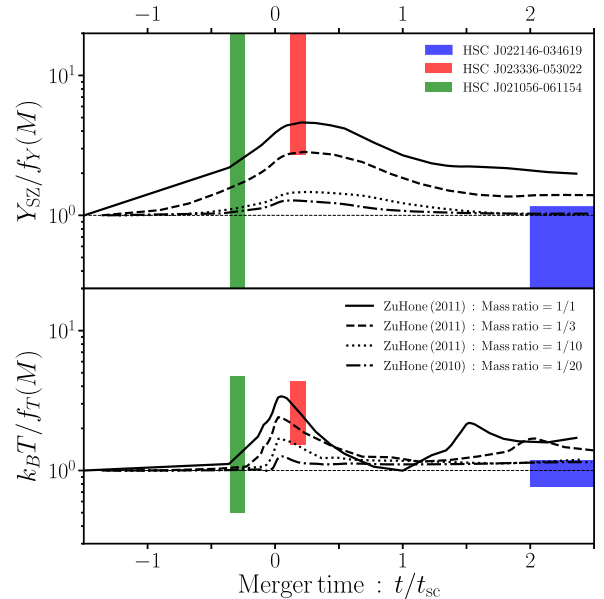

Figure 22. Time evolution of the merger boost. The *x*-axis is the time in units of the sound-crossing time. The function, *f*(*M*), is the temperature or the integrated Compton *y* parameter expected from the WL masses on the basis of the scaling relations (Lieu et al. 2016; Gupta et al. 2017). From left to right, rectangles mark HSC J021056-061154, HSC J023336-053022, and HSC J022146-034619, respectively. The errors in *y*-axes take into account the 1σ uncertainties of both gas measurements and WL masses. The solid, dashed, and dotted lines are results of numerical simulations (ZuHone 2011) of mass ratio 1:1, 1:3, and 1:10, respectively, assuming head-on mergers. The dash–dotted line shows the result of numerical simulations (ZuHone et al. 2010) of mass ratio 1:20 with an impact parameter of 200 kpc.

reported by previous studies. For instance, Okabe & Umetsu (2008) found that the gas distribution for on-going mergers is completely different from the dark matter distribution, while the two distributions before mergers are similar. The deviation of the total gas mass from the baseline is $3.6^{+1.4}_{-0.8}\sigma$, where we consider the error correlation through WL-determined radius. The deviation may be affected by cluster mergers, though we cannot rule out the possibility that the total gas mass before the merger is intrinsically higher than the baseline.

4.6.4 Time evolution

We finally investigate how much the temperature and the integrated Compton *y* parameter change with dynamical time during cluster mergers, as discussed above. Assuming that the gas properties before cluster mergers follow the scaling relations (Lieu et al. 2016; Gupta et al. 2017), we compute the ratio between the observable and the expectation of WL masses via the scaling relations, *f*(*M*). The range of plausible dynamical times is estimated by spatial separations between WL-determined centres (Section 4.2) or galaxy clumps (Sections 4.1 and 4.3) and inferred velocity. The dynamical time is normalized by the sound-crossing time to allow comparisons from different mass systems. We ignore the distance along the line of sight. We assume that the dynamical time ranges are 0.1 Gyr for the pre- and post-mergers and 1 Gyr for the sloshing phase as uncertainties. The result is shown in Fig. 22. The errors in the scaled Y_{SZ} and $k_B T$ values for each cluster take into account the 1σ uncertainties of both spherically symmetric gas models and WL masses. We also plot results of *N*-body and hydrodynamic numerical simulations of

binary mergers (ZuHone 2011) and sloshing (ZuHone et al. 2010) that are computed from the publicly-available catalogue (ZuHone et al. 2018). The solid, dashed, and dotted lines are the time evolution for head-on mergers of mass ratios 1:1, 1:3, and 1:10 from ZuHone (2011), respectively. The dash–dotted line is for mass ratio of 1:20 with impact parameter of 200 kpc, retrieved from ZuHone et al. (2010). The first two and last one are our references for the major and minor mergers, respectively. We normalize the simulated gas properties by the initial states. The temperature and the integrated Compton y parameter of ZuHone (2011) are shown as would be observed for a merger in the plane of the sky, and calculated within 300 kpc for the temperature and r_{500} for the integrated Compton y parameter from the X-ray surface brightness peaks. The off-axis merger of the sloshing simulation (ZuHone et al. 2010) are calculated for the same direction as Fig. 8. The overall trend of the time evolution from numerical simulations do not conflict with our results. Although the current sample of clusters is only three, future follow-up studies will significantly increase the number of clusters. Both the k_BT and Y parameters for the major merger are boosted from the baseline, which suggests that the scatter in the temperature and Y parameter, that is, the temperature and gas density, is correlated. Numerical simulations have shown negative (Kravtsov, Vikhlinin & Nagai 2006) and positive (Stanek et al. 2010) correlations between temperature and gas mass scatter. Gaspari et al. (2014) have discussed the origin of this pressure fluctuations. The subsonic motions mainly drive isobaric turbulence and entropy index perturbations, while high velocity motions with $\mathcal{M} > 0.5$ trigger compressive pressure fluctuations. Super-sonic motion in the major merger regime supports the latter case. Previous observational studies (Okabe et al. 2014b; Ghirardini et al. 2019) found that intrinsic scatter of entropy profiles is lower than that of pressure profiles in several local cluster samples. It indicates that the intrinsic scatter of the electron number density is correlated with that of the temperature (see also; Okabe et al. 2010). When temperature and density fluctuations are correlated, the Y parameter is affected and major mergers can give a systematic bias cluster cosmology. Although significant merger boosts were found in previous studies using non-cosmological simulations (e.g. Ricker & Sarazin 2001; Poole et al. 2007; Wik et al. 2008) and this paper, the merger boost in the Y parameter is not significant in some cosmological simulations (e.g. Krause et al. 2012; Yu et al. 2015). This discrepancy is an open question theoretically. Based on the observational approach, follow-up multiwavelength observations for a large sample of clusters are essential to answer this question and understand the thermodynamics of the gas. As pointed out by Okabe et al. (2019), the galaxy distribution contains unique and ideal information to construct a homogeneous sample of cluster mergers, in particular because of long lifetime of galaxy subhalos, a similarity between galaxy and dark matter distributions, and insensitivity to the ICM merger boosts. Although the sample can cover from pre- to post-mergers, it is difficult to distinguish between pre- and post-mergers, and thus, follow-up observations are important to measure the gas properties and characterize the impact of merging phenomena on the cluster evolution. We do not use any X-ray information for the follow-up sample definition in this paper; nevertheless, we found evidence for a merger boost, which is promising for future follow-up observations. Furthermore, a large sample of merging clusters will fill the parameter space of the dynamical time and the mass ratio, and statistically overcome uncertainties in the values of the impact parameter of cluster mergers, inclination angle of cluster mergers relative to the plane of sky, and intrinsic scatter of initial states.

4.7 Central entropy index profiles and centroid offsets

The distribution of galaxies provides a strong indication of whether a cluster is undergoing a major merger, and the phase of that interaction, but cannot inform us about the status of the cluster atmospheres. Further, optical searches are not good at identifying low-mass subhaloes and mergers where the halo barycentres are closely spaced. Since gas properties are more or less changed by both major and minor mergers, and the duration of the change continues over several sound-crossing times (e.g. Ricker & Sarazin 2001; Poole et al. 2007; Wik et al. 2008; ZuHone 2011), and repeated interactions with small subhaloes can sustain X-ray perturbation (Ascasibar & Markevitch 2006; ZuHone et al. 2010), the gas properties provides us with the essential information of the activity of gas, which is complementary to the optical galaxy distributions.

Pratt et al. (2010) have investigated cluster dynamical properties using X-ray-based entropy index profiles in the inner regions of 31 nearby clusters ($z \lesssim 0.15$) from the representative *XMM–Newton* cluster structure survey (REXCESS). They assumed a spherically symmetric model and found that the central entropy for morphologically disturbed clusters is higher than the baseline expected from cosmological simulations (Voit, Kay & Bryan 2005), but that for cool core clusters follows the baseline. That feature would be explained by the scenario that merging subhaloes penetrate into central regions of the main clusters, and then heat and disturb the central gas. We therefore investigate central entropy profiles. Following Pratt et al. (2010), we first assume a spherically symmetric model from 1D analysis. We normalized the radius by the WL-determined r_{500} and the entropy by the characteristic entropy computed by WL masses. The characteristic entropy is specified by equation 3 of Pratt et al. (2010). We here ignore WL measurement errors for simplicity. The resulting profiles of electron entropy index are higher than the baseline from numerical simulations (Voit et al. 2005), as shown in the left-hand panel of Fig. 23. The electron entropy index at $r \sim 0.01r_{500}$ is $\sim 0.1K_{500}$, which is similar to the case of the morphologically disturbed clusters of Pratt et al. (2010). Indeed, the y and S_X maps for the three clusters are complexly distributed. Since we have carried out multicomponent analyses, we computed the corresponding profiles for the main cluster component of the gNFW model. The right-hand panel of Fig. 23 shows that the entropy for the main cluster component follows the baseline. That suggests that, when we interpret the entropy profile in the three dimensional space from the projected information, the geometrical assumption and the number of components are both important. If the hot component is spatially offset from the cluster centre, the entropy index close to the centre for the spherical model would be overestimated due to the low density in this region.

We next compare centroids determined by the 2D analyses (Table 5) with the BCG positions. The left-hand and right-hand panels in Fig. 24 show gas centre and mass centre offsets. The gas centres are obtained by a forward modelling method, and thus differ from the peak positions of the SZE and/or X-ray distributions. The mass centre for the pre-minor merger, HSC J021056-061154, cannot be estimated since there is no shape catalogue in the central region (Section 3.4). The gas offsets for the sloshing cluster, HSC J022146-034619 and the pre-minor merger are smaller than those of the major-merger, HSC J023336-053022. We adopted the single gNFW model for HSC J022146-034619. The WL-determined centroids for the major merger agree with the BCGs (Section 4.2.2), while that for the sloshing cluster is slightly offset (Section 4.1.2). Offset features in gas and mass distributions show different trends and have no correlation with central entropy profiles. Therefore, the offset
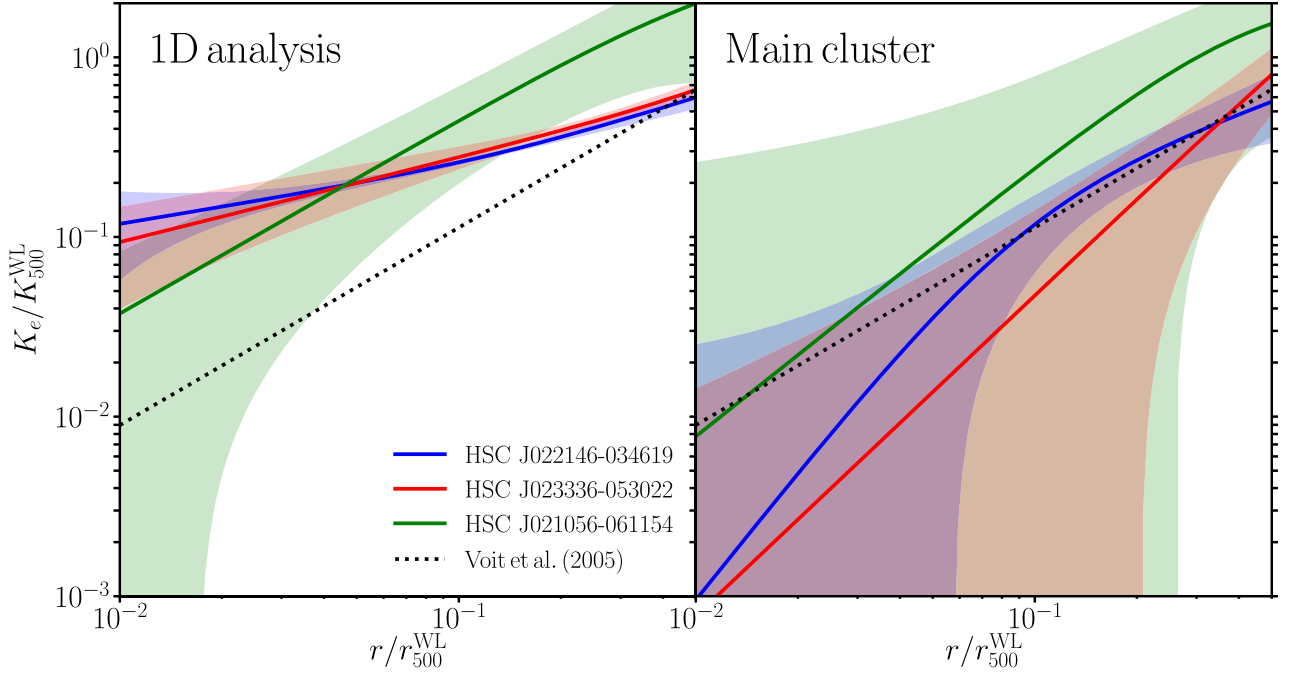
Figure 23. Central entropy index profiles normalized by weak-lensing radii and masses. *Left:* results from 1D analysis. *Right*: results for the main cluster components (gNFW model) derived from the multicomponent analysis. Blue, red, and green solid lines are HSC J022146-034619, HSC J023336-053022, and HSC J021056-061154, respectively. The colour-shaded regions represent the 1σ uncertainty bounds. The black dotted line is $K/K_{500} = 1.41(r/r_{500})^{1.1}$ of Voit et al. (2005). $K_{500} = 375 \,\mathrm{keV\,cm^2}(M_{500}^{\mathrm{WL}}/10^{14}h_{70}^{-1}\mathrm{M_\odot}E(z))^{2/3}(f_b/0.15)^{-2/3}$ from equation 3 of Pratt et al. (2010), where f_b is the baryon fraction.
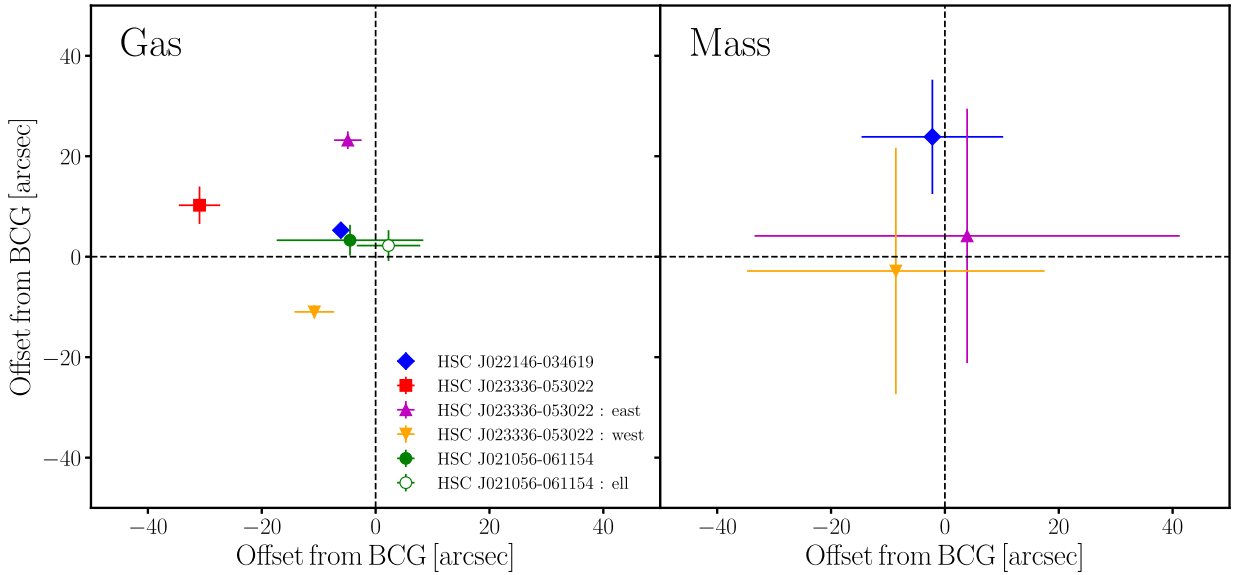
Figure 24. *Left*: offsets between gas centres obtained by the 2D joint SZE and X-ray analysis and the BCGs. *Right* offsets between mass centres determined by the 2D analysis and the BCGs. Colour symbols are the same as Fig. 19.

distances, especially gas centres, will give complementary indicators about the dynamical state.

4.8 Mass comparison

We next compare hydrostatic equilibrium (HE) masses with WL masses as a function of radius. The HE masses are evaluated through

the HE equation

$$M_{\mathrm{HE}}(<r) = -\frac{r^2}{G\mu m_p n_e}\frac{\mathrm{d}P_e}{\mathrm{d}r}, \tag{23}$$

where $\mu = 0.62$ is the mean molecular weight. For the multicomponent gas analysis, we take account of the off-centring effect (equation 22) for the electron number density and pressure profiles but ignore the offsets along the line of sight. Similarly, the two
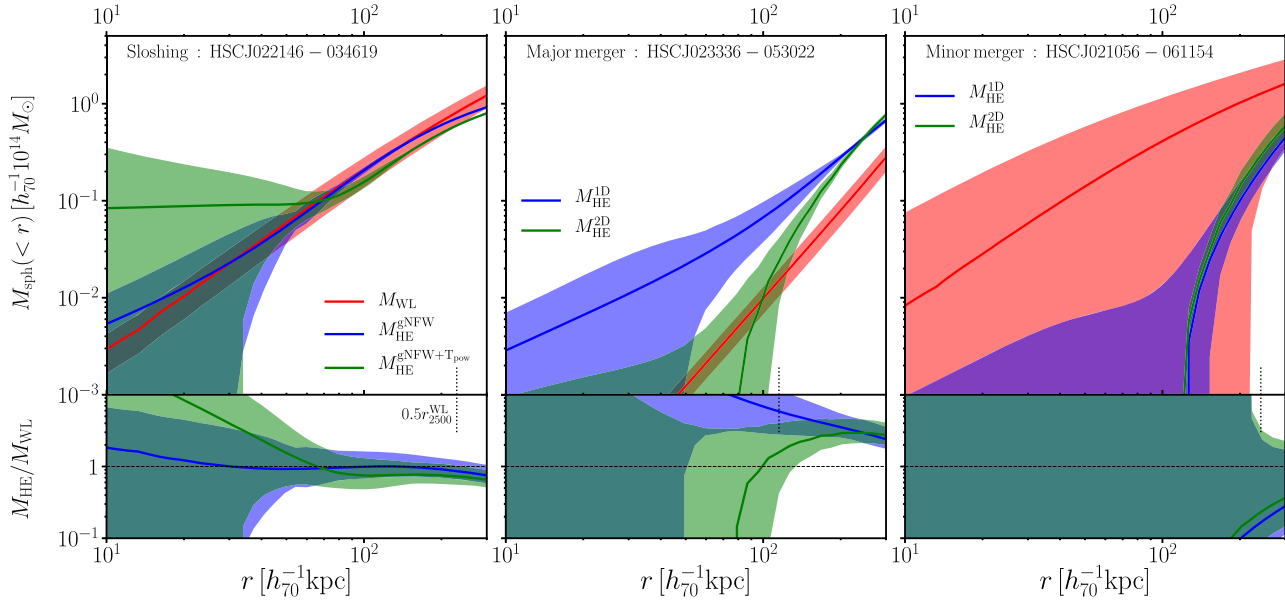
Figure 25. *Top*: HE and WL enclosed masses as a function of 3D radius (from left to right; HSC J022146-034619, HSC J023336-053022, and HSC J021056-061154). The red and blue lines denote the WL and HE mass profiles, respectively. The green lines are the HE mass profile derived from gNFW+T_{pow} model in the left-hand panel and 2D analysis in the middle and right-hand panels. The colour transparent regions denote the 1σ uncertainty. *Bottom*: HE to WL total mass ratios as a function of radius. The vertical dotted lines denote $0.5r_{2500}^{WL}$.

WL mass estimates by the 2D analysis are converted into 1D radial profiles through the off-centring effect in the mass density. Fig. 25 shows the spherical mass profiles derived by the joint SZE and X-ray analysis and by WL analysis. The figure also shows the mass ratio M_{HE}/M_{WL} out to 300 h_{70}^{-1}kpc which is comparable to the maximum radii (∼1 arcmin) of our positive y measurements. Since we cannot use the shape catalogue in the central region, the WL measurement errors for HSC J021056-061154 are large and the mass ratio cannot be constrained well. We find for the single-peaked cluster, HSC J022146-034619, that the HE mass is consistent with the WL one, while for the merging cluster, HSC J023336-053022, that the HE mass exceeds the WL one because of the merger-boost.

Although it is difficult to make a fair comparison with the literature because of the small set of clusters and differences in the radial range ($r \lesssim r_{2500}$; Fig. 25), we first compare results from a large compilation of clusters with masses measured at $\Delta = 2500-500$, because the mass bias at central regions is not yet well studied. Agreement of the HE and WL mass estimations of are reported by Local Cluster Substructure Survey (LoCuSS; Smith et al. 2016) and the XXL Survey (Sereno et al. 2020) at $\Delta = 500$, and weighing the Giants (wtG; Applegate et al. 2016) at $\Delta = 2500$. Their differences are at most of the order of $\lesssim$ 10 per cent. The LoCuSS (Smith et al. 2016) uses *Chandra* and *XMM–Newton* data with X-ray temperature measurements from the two satellites (Martino et al. 2014) and Subaru/Suprime-Cam WL analysis (Okabe & Smith 2016). The XXL Survey (Sereno et al. 2020) uses *XMM–Newton* X-ray measurements and assumed the universal pressure profile and Subaru/HSC-SSP WL data (Umetsu et al. 2020). The wtG (Applegate et al. 2016) uses *Chandra* X-ray measurements and Subaru/Suprime-Cam WL analysis (Applegate et al. 2016) for 12 relaxed clusters. All the X-ray and WL mass measurement techniques are different (see also Pratt et al. 2019), nevertheless the comparisons only found a discrepancy ∼ 30 per cent. However, the Canadian Cluster Comparison Project (CCCP; Mahdavi et al. 2013) with their new WL mass measurement (Hoekstra et al. 2015) have shown that the HE mass is on average

∼ 25 per cent lower than the WL mass (see also Smith et al. 2016). Pratt et al. (2019) have summarized that the CCCP WL masses are similar to those of LoCuSS and Cluster Lensing And Supernova survey with Hubble (CLASH; Umetsu et al. 2016) and thus, the discrepancy would be caused by a difference between X-ray analyses. Siegel et al. (2018) have carried out a joint analysis of *Chandra* X-ray observations, Bolocam thermal SZ observations, *HST* strong-lensing data, and Subaru/Suprime-Cam weak-lensing data for 6 regular CLASH clusters, and constrained that the non-thermal pressure fraction at $r_{2500} - r_{500}$ is < 10 per cent. Thus, state-of-art analyses using good resolution data resolving the internal structure suggest only a minor contribution of non-thermal pressure. However, interestingly, the *Planck* masses are ∼ 30–40 per cent lower than the WL masses, even when we use the same WL masses from Penna-Lima et al. (CLASH; 2017) and von der Linden et al. (wtG; 2014). It indicates that an observational discrepancy between WL and HE masses highly depends on how the HE masses are estimated.

A numerical simulation (Nelson et al. 2014) has found that the non-thermal pressure has a strong dependence of cluster-centric radius and a weak dependence of the mass accretion rate. The non-thermal pressure changes from ∼ 10 per cent, ∼ 15 per cent, to ∼ 40 per cent as the radius increases from $0.2r_{200m} \sim r_{2500}$, $0.4r_{200m} \sim r_{500}$, to r_{200m}. Biffi et al. (2016) also found a similar radial dependence. The average HE mass biases for cool-core and non-cool-core clusters are $\lesssim$ 5 per cent and ∼ 10 per cent at r_{2500}, and ∼ 10 per cent for the both at r_{500}, respectively. Therefore, the simulated HE mass bias at cluster cores is likely to be small, which agrees with our results. Similar results in central regions are reported by Okabe et al. (2016) and Hitomi Collaboration (2016). Okabe et al. (2016) have found that the central mass profile (r < 300 kpc) determined from the joint stellar kinematics and WL analysis is in excellent agreement with those from independent measurements, including dynamical masses estimated from the cold gas disc component, the HE mass profile, and the BCG stellar mass. The quiescent gas motion around the BCG in the Perseus cluster

is directly observed by the *Hitomi* satellite (Hitomi Collaboration et al. 2016). Since the amplitude of non-thermal pressure varies from cluster-to-cluster, it is important to increase the number of clusters for further assessments.

The differences between the HE and WL masses in previous numerical simulations and observations are small ($\lesssim$ 5–10 per cent) at small radii. We found a similar result in the single-peaked cluster, but for the merging clusters the HE mass is higher than the WL one.

5 CONCLUSIONS

We performed GBT/MUSTANG-2 observations for three HSC-SSP CAMIRA clusters (Oguri et al. 2018) with different galaxy distributions: one single-peaked cluster; one double-peaked cluster; and one belonging to a supercluster.

We carried out the following analyses for each cluster. We compared the *y* maps with X-ray images taken from the XXL survey and HSC-SSP optical galaxy distributions. The gas distributions observed by the SZE and X-ray method provide different information. We performed Bayesian forward modelling via simultaneous fits to MUSTANG-2 *y* and XXL X-ray data and measured gas properties. We measured WL masses using the HSC-SSP shape catalogue. We have looked through the library of simulations presented by ZuHone et al. (2018) and identified systems with similar X-ray and *y* properties for each of the three clusters. We summarize the main results for each cluster.

The results of the single-peaked cluster, HSC J022146-034619, are as follows:

(i) We found that the SZE and X-ray distributions have regular morphology, but the galaxy distribution is elongated.

(ii) The temperature profile measured by the joint analysis agrees with the temperature profile based on the X-COP method (Eckert et al. 2017).

(iii) The excess *y* distribution from the best-fitting gNFW profile is found at 3σ level at $\lesssim$ 4 arcsec from the BCG.

(iv) The residual *y* and S_X patterns from the model-independent, azimuthally averaged profiles are coherent, indicating that the cluster is likely to be in a sloshing phase.

(v) Two subhalo candidates that plausibly drive the sloshing mode are found. The first candidate is the second brightest galaxy and the second one is at 1.3 Mpc south of the BCG.

(vi) The coherent residual patterns is found in simulated *y* and S_X distributions (ZuHone et al. 2010).

The results of the double-peaked cluster, HSC J023336-053022, are as follows:

(i) A double-peaked *y* morphology with each peak associated with a separate galaxy concentration and a single X-ray core between the two *y* peaks are found.

(ii) Such a double-peaked *y* feature is not yet reported in previous studies.

(iii) The multicomponent analysis indicates two hot components with temperatures $28.4^{+5.9}_{-6.0}$ keV (west) and $20.2^{+3.5}_{-3.4}$ keV (east), where the temperatures are the X-ray-like emission-weighted temperatures measured within 300 kpc from the best-fitting centres.

(iv) The 2D WL analysis indicates that the western component is the main cluster. The mass ratio is $0.54^{+0.93}_{-0.28}$.

(v) The density and temperature distributions and the mass and galaxy distributions indicate that the cluster is likely to be a major merger after core crossing.

(vi) Some numerical simulations of merging systems (ZuHone 2011) show a double-peaked *y* distribution and single S_X distribution.

(vii) We do not find significant levels of diffuse radio emission in the FIRST, GMRT, and TGSS data with high angular resolutions. The absence of diffuse radio emission implies an efficiency of less than 1 per cent for conversion of kinetic energy into relativistic electrons, assuming a magnetic field strength $B > 1\,\mu$G.

The results for the supercluster member, HSC J021056-061154, are as follows:

(i) An elongated *y* distribution is offset from the X-ray main peak, which is around the BCG position.

(ii) The multicomponent analysis indicates a hot component elongated perpendicular to the major-axis of the X-ray core.

(iii) The anisotropic *y* and temperature distributions indicates that the cluster is likely to be in a pre-merger phase.

(iv) From stellar mass estimates of member galaxies, we suggest that the cluster is a minor merger with a total mass ratio of ∼1:10.

(v) Distributions in *y* and S_X like the observed ones are also found in numerical simulations (ZuHone 2011).

We then studied cluster properties and their relationship with their dynamical dependence. One of the striking results is that the distributions of the gas properties (temperature, density, and pressure) are more or less disturbed regardless of the global red galaxy distributions. The projected temperatures derived from the joint SZE and X-ray analysis are in a good agreement with those of X-ray measurements. We computed deviations from the mass scaling relations of the temperature, the integrated Y_{cyl} parameter, and the gas mass and the relationships with their dynamical dependence. We find a merger-driven boost in the $M-T$ (Lieu et al. 2016) and $M-Y_{cyl}$ (Gupta et al. 2017) relations, which is in good agreement with numerical simulations (ZuHone 2011). Although the *y* and S_X distributions of all the three clusters are disturbed and the central entropy index profiles are higher than the baseline from numerical simulations (Voit et al. 2005), the global k_BT and Y_{cyl} are changed only for the major merger just after core-passage. The WL mass profiles for the sloshing and minor merger agree with the HE mass profiles at $r \lesssim 300$ kpc, while the HE mass for the major merger is higher than the WL one.

The joint analysis of the high-angular resolution SZE and X-ray data enables us to simultaneously determine the 3D profiles of the temperature and the density and their centres. It can spatially resolve hot components at temperatures of tens of keV, which are not well measured by existing X-ray satellites. The spatial resolution of the projected temperature distribution is ∼ 0.05 arcmin^2 and higher than those of X-ray spectroscopic measurement (the order of the arcmin^2). Therefore, such analyses can overcome the problems of poor angular resolution of X-ray temperature measurements and provide a tool for studying the hottest components of clusters and cluster mergers. In the future, systematic follow-up observations for optical clusters in various dynamical stages will play an important role in cluster physics.

DATA AVAILABILITY

GBT data was taken under the project ID AGBT17B_101.

The Hyper Suprime-Cam (HSC) collaboration includes the astronomical communities of Japan and Taiwan and Princeton University. The HSC instrumentation and software were developed by the National Astronomical Observatory of Japan (NAOJ), the Kavli Institute for the Physics and Mathematics of the Universe (Kavli IPMU), the University of Tokyo, the High Energy Accelerator Research Organization (KEK), the Academia Sinica Institute for Astronomy and Astrophysics in Taiwan (ASIAA), and Princeton University. Funding was contributed by the FIRST programme from Japanese Cabinet Office, the Ministry of Education, Culture, Sports, Science and Technology (MEXT), the Japan Society for the Promotion of Science (JSPS), Japan Science and Technology Agency (JST), the Toray Science Foundation, NAOJ, Kavli IPMU, KEK, ASIAA, and Princeton University.

This paper makes use of software developed for the Vera C. Rubin Observatory (VRO). We thank the VRL Project for making their code available as free software at https://www.lsst.org/about/dm.

The Pan-STARRS1 Surveys (PS1) have been made possible through contributions of the Institute for Astronomy, the University of Hawaii, the Pan-STARRS Project Office, the Max-Planck Society and its participating institutes, the Max Planck Institute for Astronomy, Heidelberg and the Max Planck Institute for Extraterrestrial Physics, Garching, The Johns Hopkins University, Durham University, the University of Edinburgh, Queen's University Belfast, the Harvard-Smithsonian Center for Astrophysics, the Las Cumbres Observatory Global Telescope Network Incorporated, the National Central University of Taiwan, the Space Telescope Science Institute, the National Aeronautics and Space Administration under grant no. NNX08AR22G issued through the Planetary Science Division of the NASA Science Mission Directorate, the National Science Foundation under grant no. AST-1238877, the University of Maryland, and Eotvos Lorand University (ELTE) and the Los Alamos National Laboratory.

Based on data collected at the Subaru Telescope and retrieved from the HSC data archive system, which is operated by Subaru Telescope and Astronomy Data Center at National Astronomical Observatory of Japan.

XXL is an international project based around an XMM Very Large Programme surveying two 25 deg^2 extragalactic fields at a depth of $\sim 6 \times 10^{-15}$ erg cm^{-2} s^{-1} in the [0.5–2] keV band for point-like sources. The XXL website is http://irfu.cea.fr/xxl. Multiband information and spectroscopic follow-up of the X-ray sources are obtained through a number of survey programmes, summarized at http://xxlmultiwave.pbworks.com/.

REFERENCES

Adami C. et al., 2018, A&A, 620, A5
Aihara H. et al., 2018a, PASJ, 70, S4
Aihara H. et al., 2018b, PASJ, 70, S8
Aihara H. et al., 2019, PASJ, 71, 114
Applegate D. E. et al., 2016, MNRAS, 457, 1522
Arnaud M., Pratt G. W., Piffaretti R., Böhringer H., Croston J. H., Pointe-couteau E., 2010, A&A, 517, A92
Ascasibar Y., Markevitch M., 2006, ApJ, 650, 102
Basu K., Sommer M., Erler J., Eckert D., Vazza F., Magnelli B., Bertoldi F., Tozzi P., 2016, ApJ, 829, L23
Biffi V. et al., 2016, ApJ, 827, 112
Birkinshaw M., 1999, Phys. Rep., 310, 97
Bleem L. E. et al., 2015, ApJS, 216, 27
Böhringer H. et al., 2004, A&A, 425, 367
Bosch J. et al., 2018, PASJ, 70, S5
Botteon A., Gastaldello F., Brunetti G., Kale R., 2016, MNRAS, 463, 1534
Botteon A., Brunetti G., Ryu D., Roh S., 2020, A&A, 634, A64
Bouillot V. R., Alimi J.-M., Corasaniti P.-S., Rasera Y., 2015, MNRAS, 450, 145
Bradač M. et al., 2006, ApJ, 652, 937
Carrasco Kind M., Brunner R. J., 2014, MNRAS, 438, 3409
Cassano R. et al., 2013, ApJ, 777, 141
Cavaliere A., Fusco-Femiano R., 1976, A&A, 500, 95
Chen K.-F., Oguri M., Lin Y.-T., Miyazaki S., 2020, ApJ, 891, 139
Condon J. J., Cotton W. D., Greisen E. W., Yin Q. F., Perley R. A., Taylor G. B., Broderick J. J., 1998, AJ, 115, 1693
Coupon J., Czakon N., Bosch J., Komiyama Y., Medezinski E., Miyazaki S., Oguri M., 2018, PASJ, 70, S7
Di Mascolo L., Churazov E., Mroczkowski T., 2019a, MNRAS, 487, 4037
Di Mascolo L. et al., 2019b, A&A, 628, A100
Dicker S. R. et al., 2014, J. Low Temp. Phys., 176, 808
Diemer B., Kravtsov A. V., 2015, ApJ, 799, 108
Drury L. O., 1983, Rep. Progr. Phys., 46, 973
Eckert D., Molendi S., Paltani S., 2011, A&A, 526, A79
Eckert D., Ettori S., Pointecouteau E., Molendi S., Paltani S., Tchernin C., 2017, Astron. Nachr., 338, 293
Eckert D. et al., 2019, A&A, 621, A40
Ettori S., Donnarumma A., Pointecouteau E., Reiprich T. H., Giodini S., Lovisari L., Schmidt R. W., 2013, Space Sci. Rev., 177, 119
Ettori S. et al., 2019, A&A, 621, A39
Farahi A., Evrard A. E., McCarthy I., Barnes D. J., Kay S. T., 2018, MNRAS, 478, 2618
Furusawa H. et al., 2018, PASJ, 70, S3
Gaspari M., Churazov E., Nagai D., Lau E. T., Zhuravleva I., 2014, A&A, 569, A67
Ghirardini V., Ettori S., Eckert D., Molendi S., Gastaldello F., Pointecouteau E., Hurier G., Bourdin H., 2018, A&A, 614, A7
Ghirardini V. et al., 2019, A&A, 621, A41
Giles P. A. et al., 2016, A&A, 592, A3
Gralla M. B. et al., 2014, MNRAS, 445, 460
Guglielmo V. et al., 2018, A&A, 620, A7
Gupta N., Saro A., Mohr J. J., Dolag K., Liu J., 2017, MNRAS, 469, 3069
Ha J.-H., Ryu D., Kang H., 2018, ApJ, 857, 26
Halverson N. W. et al., 2009, ApJ, 701, 42
Helfand D. J., White R. L., Becker R. H., 2015, ApJ, 801, 26
Hirata C., Seljak U., 2003, MNRAS, 343, 459

Hitomi Collaboration, 2016, Nature, 535, 117

Hlavacek-Larrondo J. et al., 2018, MNRAS, 475, 2743

Hoekstra H., Herbonnet R., Muzzin A., Babul A., Mahdavi A., Viola M., Cacciato M., 2015, MNRAS, 449, 685

Huang S. et al., 2018, PASJ, 70, S6

Hughes J. P., Birkinshaw M., 1998, ApJ, 501, 1

Ichikawa K. et al., 2013, ApJ, 766, 90

Intema H. T., Jagannathan P., Mooley K. P., Frail D. A., 2017, A&A, 598, A78

Kang H., Ryu D., 2013, ApJ, 764, 95

Kawanomoto S. et al., 2018, PASJ, 70, 66

Kettula K. et al., 2013, ApJ, 778, 74

King L. J. et al., 2016, MNRAS, 459, 517

Kitayama T., Komatsu E., Ota N., Kuwabara T., Suto Y., Yoshikawa K., Hattori M., Matsuo H., 2004, PASJ, 56, 17

Kitayama T. et al., 2016, Publ. Astron. Soc. Japan, 68, 88

Komiyama Y. et al., 2018, ApJ, 853, 29

Korngut P. M. et al., 2011, ApJ, 734, 10

Krause E., Pierpaoli E., Dolag K., Borgani S., 2012, MNRAS, 419, 1766

Kravtsov A. V., Vikhlinin A., Nagai D., 2006, ApJ, 650, 128

Laganá T. F., Andrade-Santos F., Lima Neto G. B., 2010, A&A, 511, A15

Lieu M. et al., 2016, A&A, 592, A4

Lin Y.-T., Partridge B., Pober J. C., Bouchefry K. E., Burke S., Klein J. N., Coish J. W., Huffenberger K. M., 2009, ApJ, 694, 992

Mahdavi A., Hoekstra H., Babul A., Bildfell C., Jeltema T., Henry J. P., 2013, ApJ, 767, 116

Mandelbaum R. et al., 2018a, PASJ, 70, S25

Mandelbaum R. et al., 2018b, MNRAS, 481, 3170

Markevitch M., Gonzalez A. H., David L., Vikhlinin A., Murray S., Forman W., Jones C., Tucker W., 2002, ApJ, 567, L27

Martino R., Mazzotta P., Bourdin H., Smith G. P., Bartalucci I., Marrone D. P., Finoguenov A., Okabe N., 2014, MNRAS, 443, 2342

Mason B. S. et al., 2010, ApJ, 716, 739

Medezinski E., Umetsu K., Okabe N., Nonino M., Molnar S., Massey R., Dupke R., Merten J., 2016, ApJ, 817, 24

Medezinski E. et al., 2018a, PASJ, 70, 30

Medezinski E. et al., 2018b, PASJ, 70, S28

Menanteau F. et al., 2012, ApJ, 748, 7

Miniati F., Jones T. W., Kang H., Ryu D., 2001, ApJ, 562, 233

Miyaoka K. et al., 2018, PASJ, 70, S22

Miyatake H. et al., 2019, ApJ, 875, 63

Miyazaki S., Hamana T., Ellis R. S., Kashikawa N., Massey R. J., Taylor J., Refregier A., 2007, ApJ, 669, 714

Miyazaki S. et al., 2018a, PASJ, 70, S1

Miyazaki S. et al., 2018b, PASJ, 70, S27

Mroczkowski T. et al., 2009, ApJ, 694, 1034

Mroczkowski T. et al., 2019, Space Sci. Rev., 215, 17

Murata R. et al., 2019, PASJ, 71, 107

Nagai D., Vikhlinin A., Kravtsov A. V., 2007a, ApJ, 655, 98

Nagai D., Kravtsov A. V., Vikhlinin A., 2007b, ApJ, 668, 1

Nakazawa K. et al., 2009, PASJ, 61, 339

Navarro J. F., Frenk C. S., White S. D. M., 1996, ApJ, 462, 563

Navarro J. F., Frenk C. S., White S. D. M., 1997, ApJ, 490, 493

Nelson K., Lau E. T., Nagai D., Rudd D. H., Yu L., 2014, ApJ, 782, 107

Oguri M., 2014, MNRAS, 444, 147

Oguri M., Takada M., Okabe N., Smith G. P., 2010, MNRAS, 405, 2215

Oguri M. et al., 2018, PASJ, 70, S20

Okabe N., Smith G. P., 2016, MNRAS, 461, 3794

Okabe N., Umetsu K., 2008, PASJ, 60, 345

Okabe N., Zhang Y.-Y., Finoguenov A., Takada M., Smith G. P., Umetsu K., Futamase T., 2010, ApJ, 721, 875

Okabe N., Bourdin H., Mazzotta P., Maurogordato S., 2011, ApJ, 741, 116

Okabe N., Smith G. P., Umetsu K., Takada M., Futamase T., 2013, ApJ, 769, L35

Okabe N. et al., 2014a, PASJ, 66, 99

Okabe N., Futamase T., Kajisawa M., Kuroshima R., 2014b, ApJ, 784, 90

Okabe N., Akamatsu H., Kakuwa J., Fujita Y., Zhang Y., Tanaka M., Umetsu K., 2015, PASJ, 67, 114

Okabe N. et al., 2016, MNRAS, 456, 4475

Okabe N. et al., 2019, PASJ, 71, 79

Pacaud F. et al., 2016, A&A, 592, A2

Penna-Lima M., Bartlett J. G., Rozo E., Melin J. B., Merten J., Evrard A. E., Postman M., Rykoff E., 2017, A&A, 604, A89

Pierre M. et al., 2016, A&A, 592, A1

Piffaretti R., Arnaud M., Pratt G. W., Pointecouteau E., Melin J.-B., 2011, A&A, 534, A109

Plagge T. J. et al., 2013, ApJ, 770, 112

Planck Collaboration XII, 2011, A&A, 536, A12

Planck Collaboration V, 2013, A&A, 550, A131

Planck Collaboration XXIX, 2014, A&A, 571, A29

Planck Collaboration VI, 2020, A&A, 641, A6

Pompei E. et al., 2016, A&A, 592, A6

Poole G. B., Babul A., McCarthy I. G., Fardal M. A., Bildfell C. J., Quinn T., Mahdavi A., 2007, MNRAS, 380, 437

Pratt G. W. et al., 2010, A&A, 511, A85

Pratt G. W., Arnaud M., Biviano A., Eckert D., Ettori S., Nagai D., Okabe N., Reiprich T. H., 2019, Space Sci. Rev., 215, 25

Ricker P. M., Sarazin C. L., 2001, ApJ, 561, 621

Romero C. E. et al., 2015, ApJ, 807, 121

Romero C. E. et al., 2017, ApJ, 838, 86

Romero C. E. et al., 2020, ApJ, 891, 90

Rossetti M., Gastaldello F., Eckert D., Della Torre M., Pantiri G., Cazzoletti P., Molendi S., 2017, MNRAS, 468, 1917

Rozo E. et al., 2016, MNRAS, 461, 1431

Rumsey C., Perrott Y. C., Olamaie M., Saunders R. D. E., Hobson M. P., Stroe A., Schammel M. P., Grainge K. J. B., 2017, MNRAS, 470, 4638

Ruppin F. et al., 2020, ApJ, 893, 74

Rykoff E. S. et al., 2014, ApJ, 785, 104

Rykoff E. S. et al., 2016, ApJS, 224, 1

Sarazin C. L., 1999, ApJ, 520, 529

Schneider P., van Waerbeke L., Jain B., Kruse G., 1998, MNRAS, 296, 873

Sereno M. et al., 2020, MNRAS, 492, 4528

Siegel S. R. et al., 2018, ApJ, 861, 71

Sifón C. et al., 2016, MNRAS, 461, 248

Smith G. P. et al., 2016, MNRAS, 456, L74

Smolčić V. et al., 2018, A&A, 620, A14

Soker N., 2016, New A Rev., 75, 1

Stanek R., Rasia E., Evrard A. E., Pearce F., Gazzola L., 2010, ApJ, 715, 1508

Tanaka M. et al., 2018, PASJ, 70, S9

Tinker J., Kravtsov A. V., Klypin A., Abazajian K., Warren M., Yepes G., Gottlöber S., Holz D. E., 2008, ApJ, 688, 709

Ueda S. et al., 2018, ApJ, 866, 48

Umetsu K., Zitrin A., Gruen D., Merten J., Donahue M., Postman M., 2016, ApJ, 821, 116

Umetsu K. et al., 2020, ApJ, 890, 148

Vazza F., Roediger E., Brüggen M., 2012, A&A, 544, A103

Vazza F., Brüggen M., Wittor D., Gheller C., Eckert D., Stubbe M., 2016, MNRAS, 459, 70

Vogt C., Enßlin T. A., 2003, A&A, 412, 373

Voit G. M., Kay S. T., Bryan G. L., 2005, MNRAS, 364, 909

Wik D. R., Sarazin C. L., Ricker P. M., Rand all S. W., 2008, ApJ, 680, 17

Yu L., Nelson K., Nagai D., 2015, ApJ, 807, 12

ZuHone J. A., 2011, ApJ, 728, 54

ZuHone J. A., Markevitch M., Johnson R. E., 2010, ApJ, 717, 908

ZuHone J. A., Kowalik K., Öhman E., Lau E., Nagai D., 2018, ApJS, 234, 4

van Weeren R. J., Röttgering H. J. A., Brüggen M., Hoeft M., 2010, Science, 330, 347

van Weeren R. J., Brüggen M., Röttgering H. J. A., Hoeft M., Nuza S. E., Intema H. T., 2011, A&A, 533, A35

von der Linden A. et al., 2014, MNRAS, 443, 1973

[1] *Department of Physics, Hiroshima University, 1-3-1 Kagamiyama, Higashi-Hiroshima, Hiroshima 739-8526, Japan*

[2] *Hiroshima Astrophysical Science Center, Hiroshima University, 1-3-1 Kagamiyama, Higashi-Hiroshima, Hiroshima 739-8526, Japan*

[3]*Core Research for Energetic Universe, Hiroshima University, 1-3-1, Kagamiyama, Higashi-Hiroshima, Hiroshima 739-8526, Japan*

[4]*Physics Program, Graduate School of Advanced Science and Engineering, Hiroshima University, 1-3-1 Kagamiyama, Higashi-Hiroshima, Hiroshima 739-8526, Japan*

[5]*Department of Physics and Astronomy, University of Pennsylvania, 209 South 33rd Street, Philadelphia, PA 19104, USA*

[6]*Department of Astronomy, University of Geneva, ch. d'Ecogia 16, CH-1290 Versoix, Switzerland*

[7]*ESO - European Southern Observatory, Karl-Schwarzschild-Str 2, D-85748 Garching b. München, Germany*

[8]*INAF – IASF Milano, via Bassini 15, I-20133 Milano, Italy*

[9]*Academia Sinica Institute of Astronomy and Astrophysics (ASIAA), No. 1, Section 4, Roosevelt Road, Taipei 10617, Taiwan*

[10]*H.H. Wills Physics Laboratory, University of Bristol, Tyndall Avenue, Bristol BS8 1TL, UK*

[11]*Department of Astronomy, University of Virginia, 530 McCormick Road, Charlottesville, VA 22904-4325, USA*

[12]*Chalmers University of Technology, Department of Space, Earth and Environment, Onsala Space Observatory, SE-439 92 Onsala, Sweden*

[13]*Department of Physics, Toho University, 2-2-1 Miyama, Funabashi, Chiba 274-8510, Japan*

[14]*INAF – Osservatorio di Astrofisica e Scienza dello Spazio di Bologna, via Piero Gobetti 93/3, I-40129 Bologna, Italy*

[15]*INFN, Sezione di Bologna, viale Berti Pichat 6/2, I-40127 Bologna, Italy*

[16]*National Radio Astronomy Observatory, 520 Edgemont Rd., Charlottesville, VA 22903, USA*

[17]*Harvard-Smithsonian Center for Astrophysics, 60 Garden Str, Cambridge, MA 02138, USA*

[18]*SRON Netherlands Institute for Space Research, Sorbonnelaan 2, NL-3584 CA Utrecht, the Netherlands*

[19]*Institute of Astronomy, The University of Tokyo, 2-21-1 Osawa, Mitaka, Tokyo 181-0015, Japan*

[20]*Research Center for the Early Universe, School of Science, The University of Tokyo, 7-3-1 Hongo, Bunkyo, Tokyo 113-0033, Japan*

[21]*Department of Astrophysical Sciences, Princeton University, Princeton, NJ 08544, USA*

[22]*National Astronomical Observatory of Japan, Osawa 2-21-1, Mitaka, Tokyo 181-8588, Japan*

[23]*Department of Physics, Nagoya University, Aichi 464-8602, Japan*

[24]*Institute for Advanced Research, Nagoya University Furocho, Chikusa-ku, Nagoya, 464-8602 Japan*

[25]*Department of Physics, University of Tokyo, Tokyo 113-0033, Japan*

[26]*Kavli Institute for the Physics and Mathematics of the Universe (Kavli IPMU, WPI), University of Tokyo, Chiba 277-8582, Japan*

[27]*Department of Physics, Nara Women's University, Kitauoyanishi-machi, Nara, Nara 630-8506, Japan*

[28]*Argelander-Institut für Astronomie, University of Bonn, Auf dem Hügel 71, D-53121 Bonn, Germany*

[29]*AIM, CEA, CNRS, Université Paris-Saclay, Université Paris Diderot, Sorbonne Paris Cité, F-91191 Gif-sur-Yvette, France*

[30]*Department of Physics, McGill University, 3600 University Street Montreal, QC H3A 2T8, Canada*

[31]*Department of Physics, Faculty of Science, University of Zagreb, Bijenicka cesta 32, 10002 Zagreb, Croatia*

[32]*Graduate School of Natural Science & Technology, Kanazawa University, Kakuma-machi, Kanazawa, Ishikawa 920-1192, Japan*

This paper has been typeset from a TEX/LATEX file prepared by the author.